INFLUENCE OF INTEGRAL BRIDGE ABUTMENT STIFFNESS ON BACKFILL PRESSURE BUILD-UP CAUSED BY SEASONAL TEMPERATURE CHANGES

G.G. Havemann

Influence of integral bridge abutment stiffness on backfill pressure build-up caused by seasonal temperature changes

by

Garfield George Havemann

A dissertation submitted in fulfilment of the requirements for the degree of

Master of Engineering (Structural Engineering)

in the

Faculty of Engineering, Built-Environment and Information Technology

Department of Civil Engineering

University of Pretoria

Lynnwood Rd, Hatfield, Pretoria, 0002

February 2023

Abstract

Supervisor: Prof. E.P. Kearsley

Co-supervisor: Dr. S. Skorpen

Department: Civil Engineering

University: University of Pretoria

Degree: Master of Engineering (Structural Engineering)

Although the construction of integral abutment bridges (IAB) is simplified as the members are all cast monolithically with each other, the soil-structure interaction between the abutments and the retained soil significantly complicates their design. More complex thermal movement must be taken into account as opposed to the simplified methods recommended by existing design codes for jointed structures. The thermal expansion and contraction of the integral bridge's deck forces the abutment into and away from the retained soil which causes changes to the earth pressure distribution along the height of the abutment over time. For longer integral bridges, these changes are more pronounced and have greater influence on the design of the bridge.

The density of the sand increases with time due to the cyclic loading caused by the thermal action of the IAB and therefore results in a stiffer backfill against the abutments. The earth pressure build-up will occur for each thermal cycle and is highly dependent on the nature and properties of the soil and the structural stiffness of the deck and abutments of the integral bridge. This development in earth pressure over time due to cyclic loading is known as the strain hardening/soil ratcheting effect of soils and is more severe for longer bridges and for greater numbers of applied thermal cycles. Based on current literature, it is postulated that the retained soils can reach Rankine passive pressures during the bridge's design life. Large settlements can also be expected at the face of the abutments due to the corresponding volume reduction caused by the beforementioned densification of the sand that is continuously taking place.

It has been identified that sands generate the greatest rate of earth pressure development for the same amount of applied thermal cycles compared to finer soils such as silts and clays which have significantly more resilient behaviour and displayed significantly less increases in pressure over time. There is considerable uncertainty regarding the behaviour of the abutments of integral bridges due to cyclic temperature changes as the entire system (i.e., the bridge structure and retained soil) is highly dependent and influenced by each other. International design codes recommend length restrictions for the different types of integral bridges and are heavily governed by the amount of settlement at the abutment faces.

The main objective of the study was to identify the effects of integral bridge abutment stiffness during soil ratcheting caused by temperature change. More specifically, seasonal temperature

changes were investigated as the bridge deck is expected to expand the most during these cycles compared to daily cycles. The earth pressure evolution of a coarse silica sand, mechanical behaviour of the sand particles (displacements and particle flow), resiliency of the retained fill, and the overall structural behaviour (deflection, curvature, and bending moments) were evaluated experimentally by varying the stiffness of the substructure of several model integral abutment specimens that were constructed from reinforced concrete. Current literature has only investigated the soil-structure interaction of scaled abutments in the geotechnical centrifuge that were made from steel or aluminium. It should be noted that there does exist few studies that have incorporated larger scale models, and as such this study aimed to demonstrate more realistic IAB behaviour based on the constructed concrete specimens.

After testing of multiple specimens (each having different relative stiffness to the bridge deck) it was found that the degree of restraint exerted by the retained sand after 120 seasonal cycles (recommended design life of integral bridges by the British Standards) increased for greater abutment stiffnesses. It was found that the shape and magnitude of the pressure distributions as well as the structural behaviour demonstrated significant dependence on the stiffnesses of the abutment and retained sand. Based on the experimental data, the optimum choice of stiffness for the abutment specimens was evaluated.

Declaration

I, the undersigned hereby declare that:

- I understand what plagiarism is and I am aware of the University of Pretoria's policy in this regard;
- The work contained in this dissertation is my own original work;
- I did not refer to work of current or previous students, lecture notes, handbooks, or any other study material without proper referencing;
- Where other people's work has been used this has been properly acknowledged and referenced;
- I have not allowed anyone to copy any part of my dissertation;
- I have not previously in its entirety or in part submitted this dissertation at any university for a degree.

Name: Mr. Garfield George Havemann

Student number: 16006209

Date: February 2023

Acknowledgements

I wish to express my appreciation to the following organisations and persons who made this dissertation possible:

- My supervisor Professor E.P. Kearsley, for her guidance, assistance, and patience throughout the duration of my studies.
- My co-supervisor Professor S.A. Skorpen, for her highly valued advice and expertise in structural behaviour and design.
- The personnel of the University of Pretoria's Engineering 4.0 concrete laboratory for their practical experience, advice, and assistance in the construction of the experimental setup.
- The South African National Roads Agency (SANRAL), for their financial support which allowed for the construction of the experimental setup.
- My father, Mr. Leon Garfield Havemann, for his technical and mechanical expertise in the conceptual design of the steel strong box.
- My family and friends, for their enduring support in everything I do.

Garfield G. Havemann

Contents

Page

List of Tables

Page

List of Figures

Page

List of symbols

Symbol:	Description:	Natural units:
α	Coefficient of thermal expansion for concrete	Θ^{-1}
Δ or d	Deck movement due to temperature change	L
ΔL	Change in bridge length due to thermal expansion/contraction	L
ΔT	Change in temperature (seasonal)	Θ
ϵ	Strain	
ζ	Normalised length of the deck	
η	Normalised depth of soil	
λ	Slenderness ratio	
ν	Poisson's ratio	
ρ	Rowe's flexibility number	$L \cdot M^{-1} \cdot T^{2}$
ρ^{*}	Dimensionless modified Rowe's flexibility number	
$\rho_{A,P\&D}$	Modified Rowe's flexibility number by Addenbrooke *et al.* (2000)	$\dot{L^{-2}} \cdot M \cdot T^{-2}$
ρ_{max}	Maximum dry density of soil	$L^{-3} \cdot M$
ρ_{min}	Minimum dry density of soil	$L^{-3} \cdot M$
$\rho_{pluviation}$	Density of sand after pluviation	$L^{-3} \cdot M$
$\rho_{S,N\&N}$	Modified Rowe's flexibility number defined by Springman *et al.* (1996)	
ρ_{water}	Density of water	$L^{-3} \cdot M$
σ'_{h}	Horizontal effective stress in sand	$L^{-1} \cdot M \cdot T^{-2}$
σ'_{v0}	Initial vertical effective stress in sand (no settlement)	$L^{-1} \cdot M \cdot T^{-2}$
ϕ'	Internal angle of friction for soil	$^{\circ}$
A	Cross-sectional area of concrete deck/abutment	L^{2}
c'	Cohesion of drained sand	$L^{-1} \cdot M \cdot T^{-2}$
C_U	Coefficient of uniformity	
D_r	Relative density of soil	
D_{10}	Particle size of 10% passing sand	L
D_{50}	Average particle size	L
D_{60}	Particle size of 60% passing sand	L
e	Void ratio of soil	
e_{max}	Maximum void ratio of soil	
e_{min}	Minimum void ratio of soil	
E_0	Constraint modulus of elasticity of soil	$L^{-1} \cdot M \cdot T^{-2}$
$E_{concrete}$	Young's modulus of concrete	$L^{-1} \cdot M \cdot T^{-2}$
E_s	Young's modulus of soil	$L^{-1} \cdot M \cdot T^{-2}$
g	Earth's gravitational acceleration	$L \cdot T^{-2}$
G_s	Specific gravity	
H or h	Abutment height	L
I	Second moment of area	L^{4}
I_c	Second moment of area of substructure	L^{4}
I_s	Second moment of area of superstructure	L^{4}
K	Dimensionless system stiffness coefficient	
K	Effective length factor for buckling	
K	Coefficient of earth pressure (ratio of horizontal to vertical total stress in sand)	

K_0	Jaky's at-rest earth pressure coefficient	
K_a	Rankine's active earth pressure coefficient	
K_{max}	Maximum coefficient of earth pressure	
K_p	Rankine's passive earth pressure coefficient	
K_s	Shape factor	$L^{-5} \cdot M \cdot T^{-2}$
L	Total integral bridge length	L
M	Bending moment	$L^2 \cdot M \cdot T^{-2}$
N	Number of seasonal cycles applied to integral bridge	
q	Displacement flexibility number	$L^{-3} \cdot M \cdot T^{-2}$
r	Radius of gyration	L

1 Introduction to dissertation

1.1 Background

Integral Abutment Bridges (IABs) are bridges that have been constructed with the absence of any expansion joints and bearings as opposed to traditional bridges. These joints are installed for the purpose of accommodating the temperature-induced expansion and contraction of the bridge deck, eliminating any additional axial stresses that could develop between the superstructure and abutments due to temperature fluctuations.

Expansion joints and bearings are however susceptible to corrosion and immobilization which have been identified as the most serious source of damage in traditional bridges, and account for most of the maintenance and repair costs for these bridges. IABs therefore eliminate the possibility of any leakage of chemicals (e.g., de-icing salts) or water ingress into the deck expansion joints and bridge bearings and are in general more aesthetically pleasing due to the continuous superstructure of the bridge. Lower noise levels are also the result of vehicle traffic no longer crossing over the expansion joints in the bridge. IABs have been proven to be more economic due to their decreased maintenance costs and faster construction due to the superstructure being cast monolithically with the piers and abutments (Bloodworth *et al*., 2012; Dicleli & Albhaisi, 2004; Khodair & Hassitotis, 2013; Xu *et al.*, 2007a; Peric *et al.*, 2016; Rhodes and Moses, 2016).

Although the construction process is simplified, the soil-structure interaction between the bridge abutment and the retained adjacent soil greatly complicates the design of IABs (Ng *et al.*, 1998a). The temperature effects are often simplified for jointed structures in contrast to IABs where the thermal movement must be taken into account. Thermal expansion and contraction of the deck causes the abutment structure to move towards and away from the backfill respectively, causing changes to the earth pressure distribution of the soil against the abutment wall. As the length if the deck is increased, the thermally induced displacements and forces in the bridge members can also increase. The density of the soil increases with time due to the cyclic loading caused by thermal action and causes the backfill to become stiffer (Bloodworth *et al.*, 2012; Cossgrove & Lehane, 2003).

Earth pressure build-up will occur with each cycle and depends on the nature of the soil and the type of abutment used in the bridge. This earth pressure development caused by cyclic thermal expansion and contraction (seasonal and daily temperature variations) is known as the soil ratcheting effect. With greater displacement between the abutment and soil, more particle movement can occur and more strain and increased rapid stress escalation is caused during the expansion phase of the movement cycles resulting in the higher wall reactions. Settlement is common at the surface of the soil adjacent to the abutment wall which accounts for the change in volume due to the densification of the backfill material, which can cause cracking of wingwalls and opening of joints between the approach slab and joints (Naji *et al.*, 2020; Ng *et al.*, 1998; Peric *et al.*, 2016).

Sands have been shown to exhibit the greatest rate of earth pressure development over time compared to finer grained soils such as clays (Bloodworth *et al.*, 2012; Xu *et al.*, 2007b). Also,

sands with a larger internal angle of friction have been proven to cause greater earth pressures. There are still considerable uncertainties regarding the ultimate magnitudes and distributions of these pressures and the resulting ground movements that occur behind the abutments (Bloodworth *et al.*, 2012; Ng *et al.*, 1998b).

Current research on integral bridge abutment soil-structure interaction has not realistically addressed the effects of varying stiffness on the earth pressure build-up due to cyclic temperature changes (Stroyer, 1935; Rowe, 1952; Potts and Fourie, 1985; Thippeswamy *et al.*, 1994; Pappin *et al.*, 1986; Vaziri, 1996; Dicleli, 2000; Robberts, 2003; Abdel-Fattah *et al.*, 2018; Banks and Bloodworth, 2018). Only steel/aluminium materials used for the abutment have been investigated either in small-scale experimental/centrifuge testing with more focus being placed on numerical/analytical studies to investigate the behaviour between abutment stiffness and the retained fill. The general agreement between the literature is that for increasing stiffness, greater bending moments can be expected, however the influence of varying abutment thickness on the backfill soil (both in terms of the pressure distribution and the magnitudes that can be reached) after a number of expansion and contraction cycles, has not been fully defined in current available literature.

1.2 Objectives

The focus of the study was to investigate the effects of integral bridge abutment stiffness on strain hardening/soil ratcheting of a silica sand that was subject to movement caused by seasonal temperature changes.

The main objectives of the study comprised of the following:

1. Comparing the earth pressure build-up in the retained silica sand and identifying whether resilient behaviour of the silica sand could be reached within the applied number of seasonal cycles for different integral bridge abutment stiffnesses.
2. Comparing the settlements, displacements, and measured particle flow behaviour for different integral bridge abutment stiffnesses.
3. Comparing the structural behaviour which included measured deflections and strains of the specimens for different integral bridge abutment stiffnesses.

1.3 Scope of study

The study was restricted in terms of scope as follows:

- The project consists of physical testing of scaled integral abutment specimens to determine the effect of relative slenderness between the bridge deck and abutment on the stress development behind the abutment wall. Numerical modelling of the specimens was considered beyond the scope of the study.
- Reinforced concrete was used as the main material for the integral abutment bridge models.
- The soil tested during the experimental procedure is limited to only one type of coarse silica sand. Existing literature has shown that finer materials such as clays are far more resilient to the effects of ratcheting.
- The effects of surcharge pressures due to the presence of vehicle loading was excluded from the study.
- Bridge skew was neglected to eliminate any secondary effects (e.g., uplift).
- The effects of concrete shrinkage and creep were neglected. The difficulty in quantifying the shrinkage of integral abutment bridges falls outside the scope of this study.
- Only rotational movement of the abutment of integral bridges was considered.
- The effects of abutment stiffness on the ratcheting behaviour of dry silica sand were investigated. The presence of any water was thus neglected for the scope of the study.

1.4 Methodology

Scaled reinforced concrete integral bridge abutment specimens with varying abutment thicknesses were constructed to represent varying stiffnesses and were displaced against and away from a retained fill of silica sand at a constant displacement amplitude per cycle to simulate thermal expansion and contraction respectively. The specimens were subjected to an applied number of seasonal temperature cycles that represented the design life for a real integral bridge.

The methodology followed to achieve the research outcomes of the dissertation is summarised as follows:

- A study was conducted on the existing literature which focussed on overall integral bridge behaviour, the substructure response of the abutments, effects of stiffness of the abutments, the strain hardening/soil ratcheting effect, effects of temperature variation on bridges (daily and seasonal), soil type and particle effects, as well as the influence of backfill density.
- Scaled integral abutment specimens of different abutment thicknesses (representing different stiffnesses/flexibilities) were constructed from reinforced concrete and were subjected to cyclic loading. This was achieved by designing and building a steel frame box which housed the abutment-deck specimens and consisted of a laminated glass panel side door. The steel box was accompanied by a rigid frame onto which a linear actuator was installed. This allowed for displacement controlled cyclic loading by moving the

deck part of the specimens towards and away from the retained silica sand to represent seasonal temperature changes.

- A separate frame was constructed that allowed the connection of Linear Variable Differential Transformers (LVDTs) along the height of the abutment wall as well as along the length of the bridge deck that captured the deflected shapes of each specimen during testing.
- Laboratory testing was conducted (according to SANS and ASTM standard testing methods) to determine the material properties of the concrete and silica sand used.
- All specimens were instrumented with strain gauges on both faces along the height of the abutments and also along the length of the deck parts that captured the strains and corresponding bending moments.
- The glass panel door allowed for particle image velocimetry to be performed on each specimen and as such a camera setup was utilised to capture images during testing to study the flow and displacements of the sand particles.
- All tests were conducted at 1g in the University of Pretoria's concrete laboratory.
- The data captured during experimental testing was analysed and used to evaluate the effects of abutment stiffness as specified in the objectives of this dissertation (Section 1.2).

1.5 Organisation of report

The dissertation comprises of the following chapters:

- Chapter 1: The introduction to the dissertation which serves to detail the hypothesis, objectives, and scope of the study conducted.
- Chapter 2: Literature review of current and historical work done for the topic under investigation. Information contained in this chapter is used to validate and verify the experimental findings and corresponding analyses of the acquired data.
- Chapter 3: The design and construction of the experimental setup. This chapter also details the instrumentation used to capture the experimental behaviour.
- Chapter 4: The analysis and discussion of the results from the preliminary test that was conducted.
- Chapter 5: The analysis and discussion of the experimental results.
- Chapter 6: Discussion and outcome of the research objectives based on the experimental findings and literature study. Recommendations relating to the experimental setup and for future research efforts are also detailed.
- Chapter 7: List of references used.
- Appendix A: The appendix of the dissertation.

2 Literature review

2.1 Introduction

The following chapter details the literature study conducted for the dissertation.

2.2 Integral bridge abutment movement

Up until the early 20th century, the use of traditional jointed bridges were more common and desirable compared to integral bridges due to the elimination of additional stresses that arise in the bridge super-, and substructures caused by thermal expansion and contraction. These bridges are however not without their limitations as field monitoring conducted over the years by researchers (Thippeswamy *et al.*, 1994; Wolde-Tinsae *et al.*, 1988) have reported on the overall unsatisfactory performance of jointed bridges. These faults resulted in regular and extensive maintenance requirements and rehabilitation efforts on jointed bridges. Integral bridges can be defined according to Hoppe and Gomez (1996) as bridges having a superstructure that is *rigidly connected* to the substructure (abutments) which can thus allow expansion and contraction against and away from the neighbouring backfill soil respectively.

In general, integral bridges have shown to perform satisfactory with the elimination of joints intended to compensate for thermal expansion and bridge abutment bearing. The most common issue with integral bridges occurs in the approach slab and backfill region where settlement caused by continuous expansion and contraction cycles (daily and seasonal) as well as traffic loading often lead to the formation of bumps and cracks forming at the abutment and embankment interface in the approach slabs. However, it is widely regarded to be significantly more cost effective in terms of maintenance to address these issues compared to the more extensive problems caused by joints (expansion and bearing) used in traditional jointed bridges. The use of integral bridges is reported to be the standard in the majority of states in the US (Hambly, 1997).

Kunin and Alampalli (2000) surveyed multiple transportation agencies across the United States and Canada to assess the performance and current design practices of integral bridges. In general, all agencies reported highly favourable performance where the only issues that would arise for these bridges would include minor cracking, poor drainage at the abutment-embankment interface and settlement of the approach slabs. Alaskan integral bridges were reportedly more susceptible to hairline cracking in the backwalls caused by the adhesion of frozen soil due to the cold climate. The agencies located in Colorado reported that most, if not all, movement occurred in the abutments of their bridges and that there was no apparent influence on this movement due to the difference in stiffness between the superstructure and abutment (Kunin and Alampalli, 2000). Regarding soil pressures, Rankine passive earth pressure is most commonly used in the design of integral bridges in the US and Canada (with the exception of very few not taking the effects of earth pressure into account at all). Granular backfill is the most common backfill used where some opted to employ geotextile-reinforcing to aid in settlement prevention.

The overall design of integral bridges is complicated by the *soil-structure interaction* caused by the thermal movement of the deck superstructure. Vaziri (1996) mentions that the mismatch between the partial factors used in Geotechnical and Structural design also causes further complications during the analysis and design phases of these structures. Classical methods of determining the earth pressures behind retaining walls and bridge abutments often yield overestimates of the true pressures that take place and as such, determining an optimised design is typically not realistic when only relying on these methods.

Integral bridge design requires the combined skills of structural, geotechnical, and highway engineering in order to account for the soil-structure and structure-pavement interactions effectively (Hambly, 1997). Hambly (1997) also reports that many current integral bridges are designed such that the stiffnesses and flexibilities are spread throughout the structure in order to avoid any potential concentrating effects due to thermal expansion and contraction (as well as braking loads from traffic).

The use of fully integral bridges started during the 1930s and were initially short bridges with maximum lengths of approximately 30 m. Any bridge design with length exceeding this magnitude was often based solely on observed bridge prototype performance at the time where most highway agencies across the world relied on their own length restrictions and requirements for design (Hoppe and Gomez, 1996; Wolde-Tinsae *et al.*,1988). Only during the early 1980s, the first official guides to limiting integral bridge length were devised which recommended maximum lengths of approximately 90 m, 150 m and 180 m for steel, cast-in-situ concrete and pre-stressed concrete integral bridges respectively. Most of the earliest guidelines at the time can be considered conservative by today's standards and since then many developments in terms of increasing the limiting integral bridge lengths have taken place over the past few decades. A maximum movement of up to 50 mm was acceptable for integral abutments according to Hambly (1997), regardless of approach slab deformation and cracking that could occur as a result of such high deformation. In terms of the ability of piles to accommodate the large stresses due to the longitudinal and lateral displacements caused by temperature change in integral bridges, Arsoy *et al.* (1999) found that this contributes significantly to the total length of the bridge deck and must therefore be designed accordingly for the desired length of the bridge.

The length restrictions of integral bridges (both steel and concrete) were further investigated by Dicleli and Albhaisi (2004) by evaluating the maximum length that can be achieved as a function of the capacity (local buckling stability) of steel piles supporting the abutments to resist the forces caused by temperature change specifically for embankment that consists of a clayey material where the abutment-pile connection was considered as *fixed*. Their work involved static pushover analyses for symmetrical bridges with no skew where the stiffness of the bridge (in terms of the deck and abutment sizes) was considered for 2 bridges, namely a *flexible bridge* (steel structure) and a *stiff bridge* (concrete structure). Their model only considered the passive movement (into the backfill soil direction). It was determined that a larger abutment height allows for more displacement capacity of the bridge when governed by pile fatigue performance. This however has a negative effect on the displacement capacity if the design is governed by the shear and flexural resistance of the abutment. For increasing

lengths of the bridge deck, the displacement capacity was jeopardised due to the larger rotations that occur at the pile-abutment connection causing larger bending moments.

Field observations conducted by Hoppe and Gomez (1996) revealed excessive approach settlement at the embankment and bridge deck interface (extending almost 10 m from the interface) for a 98 m long two-span composite steel girder integral bridge located in Virginia, USA. The bridge did not have any approach slabs and was constructed with a 5-degree skew. From the bridge's 2-year monitoring period of the soil pressure behind the abutment walls, the pressure was observed to fluctuate about the at-rest pressure $K_0$with little change in mean soil pressure. This could be as a result of the overall secondary shrinkage and creep effects causing the bridge to shorten over time, hence reducing the effect of the thermal expansion pressures. A maximum pressure of 175 kPa (almost full passive pressure) was recorded where it was found that pressures did in fact increase over the first year but slowly levelled off in the second year of operation. These results are also in agreement with Hirakawa *et al.* (2007)'s findings. It was also found that the stresses in the steel girders were determined to be significantly smaller than the maximum design stresses. Overall, the authors concluded that the bridge in question was performing satisfactory over the 2-year monitoring period.

Arsoy *et al.* (1999) reported on the performance and behaviour of various components of integral bridges based on field monitoring and corresponding finite element analyses (plain strain models neglecting the presence of soil ratcheting). The deck was modelled to be stiff (EI_{deck} = 0.68 × 10^6 kN·m^2 per meter) in order to provide rotational restraint to the abutments which were founded on piles (EI_{piles} = 4.1 × 10^3 kN·m^2 per meter). The bridges that were monitored in the field did not contain any approach slabs and performed well in general with the exception of minor erosion taking place at the abutment-backfill interface (as a result of poor surface water drainage). Other common problems encountered during the field monitoring include cracking due to secondary effects in the abutments, greater rotation due to temperature change for skewed bridges, settlement of the approach fill, and significant stresses in piles caused by cyclic temperature changes. Arsoy *et al.* (1999) also report in their work that the approach fill had no effect on the longitudinal displacement behaviour of the bridge deck (i.e., the deck expanded and contracted as if there was no fill present). With respect to the measured earth pressures, both active and passive earth pressures were recorded during the monitoring period. Both rotational and translational movement of the abutments took place. The authors listed an important concern that abutment pressures should be determined with the displacement of the wall taken into account, with such measures not being available at the time of writing their article.

With regard to the effects of shrinkage and creep, field observations done by Wolde-Tinsae *et al.* (1988) showed that shrinkage cracks in the superstructure (deck slab) and the negative moment regions (deck piers) were common for the integral bridges in service at the time. The main drawback of integral bridges was the overall lack of information regarding the effects to these secondary forces at the time (i.e., thermally induced forces, including shrinkage and creep effects). Although thermal expansion and contraction was among the main influencing design parameters for integral bridges, the time-dependent variables such as the shortening of the concrete due to the effects of shrinkage and creep are also important factors that must be considered in the design of these structures and also have considerable impact on bridge

performance. Kim and Laman (2010)'s parametric study of IAB response prediction models was based on calibrated 2D numerical modelling (non-linear) for the AASHTO 75-year design life. 243 cases were analysed in their work where the bridges were subjected to thermal loadings and backfill pressures and also incorporated creep and shrinkage effects. The effects of the thermal expansion coefficient of the concrete, the total bridge length, height of retained backfill and corresponding stiffness, and the founding pile stiffness were investigated. Soil-pile interaction was accomplished using the *p-y* (force-displacement) data from the American Petroleum Institute (API). Their data revealed that the backfill height and corresponding stiffness does not have a significant effect on the displacement of the abutment, nor the pressure exerted by the backfill (except for piles, where shorter abutments result in greater lateral forces exerted onto the piles). The thermal expansion coefficient had a significant effect on the pile lateral forces, moments and displacements as well as the girder's axial forces and moments.

Kim and Laman (2010a)'s work was further expanded by Kim and Laman (2010b) where numerical analyses were conducted and based on four IABs located in central Pennsylvania. Their work placed emphasis on the time-dependent response and soil-structure interaction of the abutments. It should be noted that instead of the API's *p-y* curves, a simplified triangular distribution was applied to the abutments. Based on a time-dependent analysis, their numerical model was found to agree relatively well with the field data measured for the four IABs. Time-dependent effects are regarded to have significant effect on long-term behaviour (in terms of the magnitude of the displacements of the abutments) and cannot be neglected in analysis of IABs. Their findings agree well with Pugasap *et al.* (2009) where it was also stated that the time-dependent effects due to shrinkage and creep were the governing contributing factor for the displacement accumulation for the abutments near the top. This is in agreement with the research conducted by Fennema *et al.* (2005) and the findings revealed by Arockiasamy and Sivakumar (2005) where the time-dependent deflections accounted for a 100% increase in the total deflection observed for abutments that were designed for either fixed or hinged supports.

2.2.1 Effects of temperature variation (daily & seasonal)

In general, bridges will encounter the greatest expansion and contraction during summer days and winter nights respectively, with each daily variation in temperature resulting in a single cycle of both expansion and contraction (day and night respectively). The extreme temperature changes (such as the period where summer shifts to winter and vice versa) will therefore govern/control the largest displacements of integral bridges. Logically, the maxima and minima of the ambient temperatures and displacements of the bridge will coincide with one another (i.e., they are closely linked).

Darley *et al.* (1998) studied the behaviour of an integral bridge abutment. The bridge was located in Glasgow and spanned over 60 m with shallow integral abutments. The bridge was reported to have displaced about 4 mm for a temperature change of $16^{\circ}C$. Their monitoring reported some sliding that occurred between the base of the abutment and the soil foundation. Densification of the retained soil was observed over the analysis period as the thermal cycles progressed (stresses during the 1997 period were slightly higher than the years before) and

that even the smallest changes in movement of the bridge deck length due to temperature (<1 mm) had significant impact on the lateral stress acting on the abutments. The temperatures that reached up to 23 degrees showed significant increases in the lateral stresses acting on the abutments ($K > 1$, reaching up to a value of almost 2). Their data indicated (similar to Ng *et al.* (1998a)'s findings) that a combination of tilting and translational movement (sliding and deformation action of the soil foundation) took place over the monitoring period.

Brena *et al.* (2007) analysed data measured for an integral bridge (with no skew) located in Massachusetts for a period of 3 years. Both seasonal and yearly performance of the bridge was considered where it was found that measured values for the displacements due to thermal contraction and expansion were less than design values used for the construction of the bridge (up to 60%). The base rotation was found to be significantly affected by the stiffness of the superstructure and the restraint of the piles to rotations in general. The restraint to longitudinal displacement of the bridge's superstructure was deemed negligible by the authors since the thermal behaviour of the whole bridge deck resembled that of an unrestrained bar (i.e., the deck superstructure displayed close agreement with $\Delta L = \alpha \cdot \Delta T \cdot L$ where α, ΔT, and L denote the coefficient of thermal expansion, the change in temperature, and the length respectively) and concluded that the current design approach for IABs is conservative. However, the 2 abutments did reveal different behaviour in comparison to each other where the northern abutment demonstrated lower lateral restraint compared to the southern abutment (Brena *et al.*, 2007).

Results from Darley *et al.* (1998)'s study showed that even daily temperature fluctuations related closely to the lateral stresses measured against the abutments. Small hysteresis effects of about 1 kPa were measured between the expansion and contraction perturbations of the bridge deck.

De Jong *et al.* (2004) identified 3 different types of backfill interaction types with associated abutment movement due to the highly non-linear soil behaviour at the soil-abutment interface. Steady increases in temperature resulting in slow movement of the abutment results in a constant/consistent earth pressure even if the magnitude of movement is significant. During slowly decreasing temperature periods, the contraction of the bridge results in almost negligible pressures acting on the wall (active earth pressure state is achieved). During quick changes in temperature (and movement as a result), the earth pressures are expected to change linearly (either positive or negative depending on increase or decrease of temperature respectively). De Jong *et al.* (2004)'s recorded data showed that the stiffness of the soil displayed an increase with depth and this was postulated to be as a result of confining stresses. The stiffnesses of the soil that were measured along the depth were an order of magnitude less than predicted with pressure meter tests (De Jong *et al.*, 2004).

Skorpen *et al.* (2018) analysed temperature, shrinkage, and earth pressure data captured on a 90 m long integral bridge. Recorded movements due to daily temperature change measured ±1 mm and a maximum of 4.5 mm inward movement was measured when the ambient temperature dropped (12-degree effective bridge temperature change). Regarding the earth pressures, at the time of writing the authors reported that the current measured stresses exceeded at-rest pressures.

Al-Qarawi *et al.* (2020) investigated the soil settlement and increase in lateral earth pressure of a dry coarse sand that was loaded cyclically for 30 cycles at ±2 mm displacements. The test setup consisted of a 700 x 300 x 250 mm container which housed a 13 mm thick steel plate representing the abutment wall. Testing also included the presence of EPS geofoam blocks which were arranged into 2 separate configurations. At cycle 30, the earth pressure at one third the height of the wall increased by 75%, where most of the increase occurred in the first 5 cycles (compared to only 32% with the inclusion of the EPS). The neutral position (at-rest) was reportedly at a plateau after only 10 cycles. A total of 75 mm settlement was recorded at the soil-wall interface after testing excluding EPS (compared to a settlement of 31 mm with the EPS situated behind the wall). The authors also conducted a corresponding numerical study based on the experimental findings using the Mohr-Coulomb elastoplastic material model included in Abaqus in a plane-strain formulation of the geometry. Their findings concluded that the worst settlement occurs in the first few cycles where the settlement and earth pressures tend to reach an asymptote at later cycles. The inclusion of EPS showed that earth pressures can be reduced significantly, and that compaction of the adjacent fill is not the solution to the settlement issue for IABs (Al-Qarawi *et al.*, 2020).

2.3 Effects of integral bridge abutment stiffness

Some of the earliest research that focused on the effects of flexibility/stiffness of retaining walls was done by Stroyer (1928; 1935) where the earth pressure distributions were investigated specifically for flexible (elastic) walls (Stroyer, 1928) and expanded upon in Stroyer (1935) which focussed on the effects of increasing stiffness. Stroyer (1928) identified that the observed earth pressure behind sheet walls did not reach the ultimate calculated values and in many cases, it was considerably less than expected. At the time, no case was reported where such sheet walls have failed due to bending/flexure. The research made the distinction between sheet walls that were solely fixed at their base/bottom and for sheet walls supported at both the top and bottom (which is comparable to an integral bridge abutment to an extent). A significant *arching action* of the structures was present for both cases and was identified as the main contributing factor to the reduction in observed earth pressures behind the walls. It was concluded that the reduced bending moments at mid-height were caused by the shift or redistribution of the total pressure where the sliding of the nearest particles against the wall's face (which would be less compact compared to the rest of the overall fill) would take place and gradually reduces on account of the overall elasticity of the fill and the degree of deflection of the wall taking place (which at mid-height is often the greatest for the case of the connections at both the top and bottom of the sheet wall).

Stroyer (1935) investigated the influence of varied thicknesses of a steel plate which was loaded in the passive pressure condition on different soils. The reduction of bending moment in the wall was found to be a function of the coefficient of active earth pressure K_a but independent of the magnitude of the deflection. Both during flexing of the wall and afterwards, the soil should be in a stressed state where the pressure is less but if the soil particles can flow or rather a state of *flux* can occur, then the pressure will normalise, and the wall's flexed position will stabilise. A *lag* state was recorded where the observed deflection of the wall

would always be less than the theoretically determined deflection which would always become parallel at some point and continue with such an offset for the remainder of the tests and therefore any further increase in deflection would yield no further change in earth pressure. This was suggested to be the result of looser particle packing of the soil grains where the earth pressure reduction was proportional to the recorded lag. The measured lag however decreases with increasing plate thickness/flexibility/stiffness or in other words, the *reduction in pressure* will decrease with increasing wall thickness. For the case of a thin wall or plate which would have more deflection, the moving volume of grains directly behind the wall is negligible compared the volume contained in the flexed state but in the case of small deflections there could be greater presence of *flux movements* or rather flow of soil. The work done by Rowe (1952) was also focussed on assessing the influence of flexibility on the bending moment that occurs specifically in the piles of sheet-pile walls where the fill contained a water table, which further expanded on the findings of Stroyer (1935). It was found that depending on the level of the water, a decrease or even an increase in bending moment could take place and must be evaluated per structure. For increasing stiffness of the piles/walls, the greater the bending moment was found to be.

Thippeswamy *et al.* (1994) performed a parametric study on the behaviour of single-span integral bridges where the effects of super- and substructure stiffness were varied as well as the temperature, height of the retained embankment, the soil properties, types of foundation used for the abutments, as well as the connections between the approach slab and the foundation to the abutments. They used a dimensionless system stiffness coefficient K which is expressed as the ratio of the superstructure stiffness to the substructure stiffness as follows:

$$K = \frac{H}{L} \cdot \frac{I_s}{I_c} \qquad \text{Equation 2-1}$$

Where H, L, $I_s$and I_c denote the height of the abutment, the length of the bridge, the moment of inertia of the superstructure and the moment of inertia of the substructure respectively. Close attention was paid to the type of connection used for the abutment to foundation and deck/approach slab connection (either fixed, hinged or partially fixed). The most critical connection was determined to be the *hinged-hinged connection* which displayed the greatest bending moment for any selected system stiffness coefficient K. Greater moments were reached for increasing K values (i.e., greater superstructure stiffness compared to the abutment's). The bending moments for a jointless (integral) bridge were found to be about 50% of a similar jointed (classical) bridge structure.

Thippeswamy *et al.* (2002) defined a spread footing as a stiff system for an integral bridge and using a pile type foundation is regarded as a more flexible support system. They described in their work that stiffer systems induced high tensile stresses which could lead to cracking of the deck at the joint of the integral bridge abutment and superstructure. When using a portal frame as the design basis in combination with pile foundations, the expected stresses in the portal frame caused by active and passive soil pressures are almost negligible. Some agencies however still require the presence of soil pressure to be taken into account for the design of the portal frame structure. For integral bridges where the abutment substructure is founded on a row of piles, the stiffness of the substructure is comparatively smaller than the superstructure. The authors declared that based on their results for the monitored bridge (McKinleyville

bridge), earth pressures are recommended to be neglected in the design and analysis of such integral bridges. The dominant source of total stresses in the portal frame structure was found to be caused by the temperature gradient in the bridge deck.

Much of the research effort currently devoted to the study of integral bridge behaviour is heavily dependent on analytical modelling of the soil-structure interaction between the adjacent retained fill and the bridge structure. Amongst the first attempts at numerical modelling of simple flexible retaining walls was done by researchers Potts and Fourie (1985) and Pappin *et al.* (1986). Pappin *et al.* (1986) developed a finite element model incorporating the soils stiffness and behaviour using a subgrade reaction model consisting of a system of linear elastic springs positioned along the height of the wall (referred to in literature as the *Winkler spring model*). The Winkler spring model is a popular method used for modelling the behaviour of soil-structure interaction and is still in active application at the time of writing. Day and Potts (1993) investigated the static case for a retaining wall at different excavation levels and assessed the effects of element choice on the overall behaviour of the walls. It was found that using 2D beam elements provides enough accuracy for modelling sheet pile walls, specifically thin or flexible walls, and plane strain 2D elements were determined more suitable for concrete retaining walls due to the shear stresses acting on the sides of the elements as well as the thickness was shown to have noticeable effects on both the stability and the bending moment distribution. Any water pressure that was present was found to reduce the effects of wall thickness.

A practical numerical model was developed by Vaziri (1996) for the analysis of flexible retaining walls where the stiffness was represented by a series of elastic beam elements (in combination with the soil and the prestressed struts used for the wall) which form part of the *overall stiffness matrix* of the model. The model relied on the use of springs to represent the struts as well as the soil stiffness. Emphasis was placed on the *soil arching effect* (defined as the transfer of pressure from yielding masses of a soil to its static surrounding soil skeleton) behind retaining walls. This arching effect is responsible for the reduction in earth pressure on a yielding (or rather flexible) part of the wall and causes the shift in pressure to the rest of the wall. The arching effect is aggravated by increasing wall deflection and greater soil stiffnesses. The movement of retaining walls are heavily dependent on the system stiffness and it was found that, for increasing wall stiffness, movement is expected to reduce and is recommended when the surrounding soil is a soft clay. Dicleli (2000)'s work focussed on developing a simplified numerical model to determine the stresses in integral bridge abutments and the superstructure under gravity loading. The soil-structure interaction was included by representing the coefficient of earth pressure as a function of the displacement/rotation of the abutment:

$$K = K_0 + \psi d \leq K_p \qquad \text{Equation 2-2}$$

Where d and ψ represent the displacement of the abutment at a point along the height of the wall and the slope of the earth pressure variation defined by the type of backfill used in the numerical model, respectively. Equation 2-2 is applied to a series of Winkler springs along the full height of the abutment and piles. The authors investigated the effect of the ratio of the deck bending stiffness to the equivalent abutment wall bending stiffness (R_s) and concluded

in their parametric study that integral bridges with larger R_s ratios behave similarly to simply supported bridges during vertical/gravitational loading conditions. By utilising full frame action during the analysis of integral bridges under the conditions defined in Dicleli (2000), it was found to provide the most economical deck design.

Robberts (2003) conducted detailed parametric analyses of prestressed and concrete integral bridges where the time-dependent behaviour was investigated. The stiffness of the bridge abutment was varied (0.1, 0.2, 1, and 10 times the reference stiffness of the abutment) by altering the thickness of the abutment accordingly where for a full-scale integral bridge it was found that for abutment heights up to 9 m in height, the base of the abutment foundation will tend to move into the retained fill for increasing stiffnesses. For heights greater than 9 m it was found that the base will move in the opposite direction for increasing stiffness. For greater stiffness (regardless of abutment wall height) less displacement at the position of the foot of the wall took place in the direction away from the retained soil.

Abdel-Fattah *et al.* (2018) developed a plane-strain 2D finite-element model to investigate the effects of seasonal temperature change on IABs. A multi-span, solid-slab bridge was modelled, and both the construction sequence and backfilling process were included in the analysis. Their model was able to evaluate the effects of abutment stiffness where 2 different values for abutment thickness were considered (1.5 m and 1.25 m). Their numerical results showed that the stiffer abutment generated greater pressures along the wall compared to the 1.25 m thick abutment (approximately 2 to 5% greater) and this increase is more evident for longer bridges. It was also concluded that for the upper part of the backfill (upper 75% of the wall) the increase in backfill stiffness generated larger stresses, but the opposite was true for the lower 25% of the wall. From the data acquired in the experimental work conducted by Bloodworth *et al.* (2012), a numerical model was developed and a series of tests for 4 different abutment stiffnesses were analysed (a stiff abutment, 1500 mm diameter pile, 1200 mm diameter pile, and 900 mm diameter pile). A maximum reduction of 10% between the stiffest and most flexible abutment was found as seen in Figure 2-1. The authors acknowledged that although a definite soil-structure interaction mechanism was clearly present, the benefit is however more related to economical savings and that the prevalent response of the abutment as a whole, regardless of stiffness, is rotational movement.

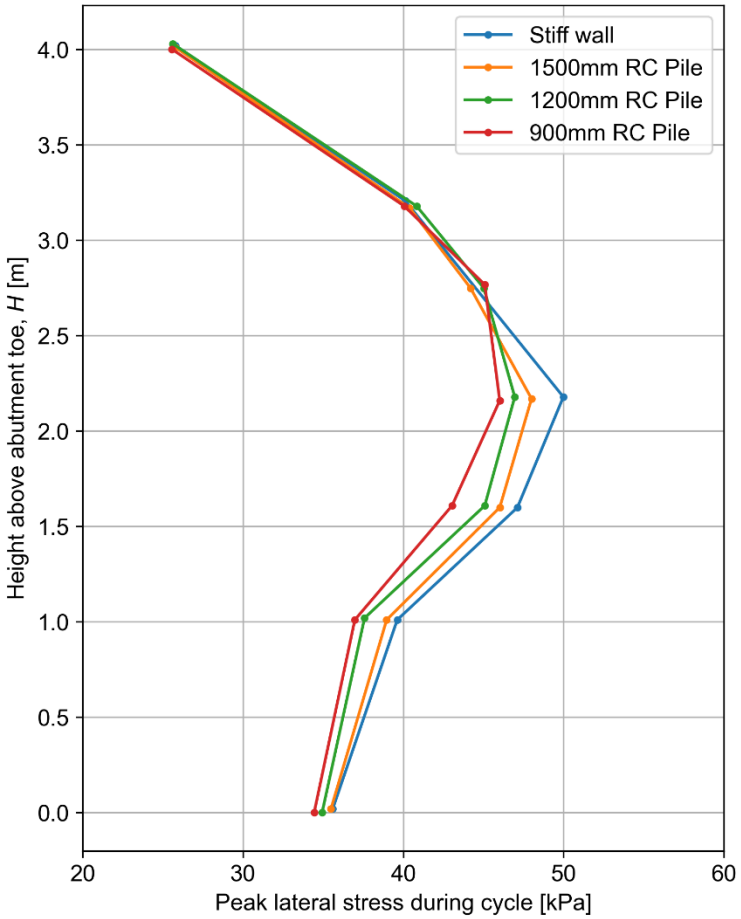

Figure 2-1: Sensitivity of peak lateral stresses to abutment stiffness (Bloodworth, Banks and Clayton, 2012).

Banks and Bloodworth (2018) also evaluated the effects of abutment stiffness and concluded that the effect of varying the stiffness was not considered to be important over the practical range of walls used in construction.

2.3.1 Integral bridge abutments compared to propped retaining walls

Considerable research effort has been devoted to the study of retaining walls and the interaction between the structural stiffness and the retained fill. The behaviour of an integral bridge abutment is comparable to the behaviour of a propped cantilever retaining wall and therefore could possibly provide better insight into the soil-structure interaction for the abutments of integral bridges. Powrie and Li (1991) utilised finite element modelling to investigate the behaviour of propped retaining walls (at formation level) supporting a 9 m high clay fill of high stiffness. The soil stiffness and pre-excavation earth pressure was found to have a significant effect on the wall's behaviour. Stiff retaining walls were the focus of the analyses, and it was found that the magnitude of both the soil and wall movements were mainly dependent on the stiffness of the soil. For lower values of soil stiffnesses, higher wall movements were present where the wall movements remained unaffected by a large change in wall stiffness of about 40%. For higher embedment ratios (length to thickness ratios), a reduction in the magnitude of wall movement was observed. The structural connection

between the retaining wall and the permanent prop slab simulated in the analyses had, to an extent, a lesser effect on the bending moment distribution compared to the pre-excavation earth pressure. This discovery could serve as evidence that it is feasible to consider that the behaviour of propped retaining walls is similar to that of the abutments of integral bridges.

The concept of a *flexibility number* for retaining walls was introduced by Rowe (1952) where the stiffness or rather flexibility of any given wall could be expressed numerically using the following relationship:

$$\rho = \frac{H^4}{EI} \qquad \text{Equation 2-3}$$

Where H denotes the height of the wall or pile and EI representing its bending stiffness. Equation 2-3 was derived to produce equal flexibility numbers for both the prototype and model representations of the structure. Results discussed in Rowe (1952) were often expressed in terms of the logarithm of this flexibility number.

The stiffness of the retaining walls was also investigated by Potts and Fourie (1985) where different at rest pressures (denoted by k in Figure 2-2) were also investigated for walls ranging from stiff to flexible as for sheet pile walls (having bending stiffnesses of 2.3×10^9 kN·m^2 and 2.3×10^4 kN·m^2 respectively). It was found that for the soft walls the movement was much greater at the mid height. This work was based on a numerical model and results were compared to the classic limit equilibrium model available at the time and found that the ratio of the bending moments determined via the numerical analysis (M_{FE}) to the limit equilibrium values (M_{LE}) decreased for an increase in the logarithm of Rowe (1952)'s flexibility number ρ (Figure 2-2).

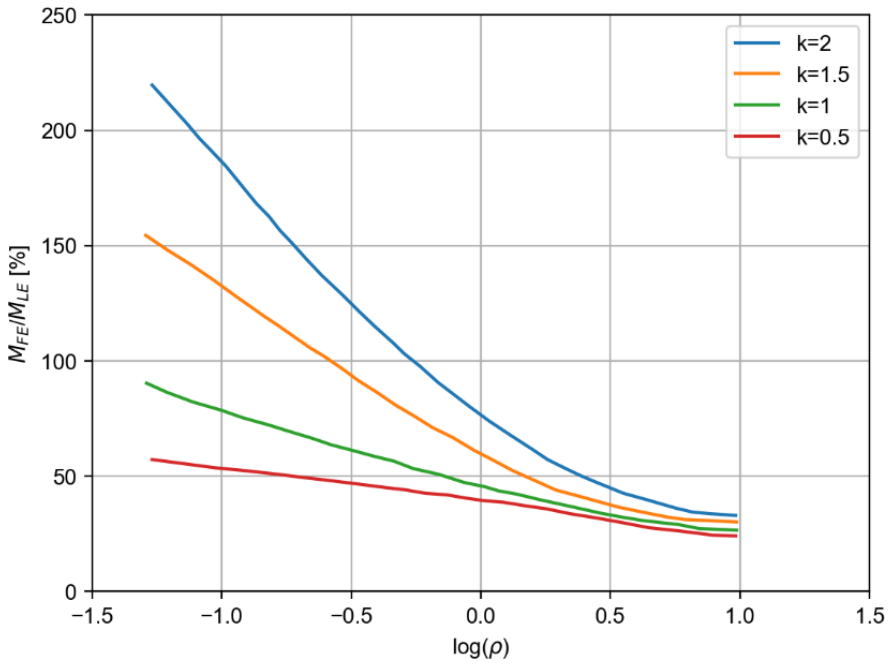

Figure 2-2:Variation in bending moment with wall stiffness (Fr=2) (Potts and Fourie, 1985).

Potts and Fourie (1985) were among the first researchers to adopt Rowe (1952)'s flexibility number in their work and suggested a normalised version of the relationship using the stiffness

of the retained soil to be used due to the fact that the stiffnesses of both the structure and the soil have an influence on the bending moments of the walls and corresponding prop forces. One of the earliest applications of the normalised flexibility number was used in the work conducted by Potts and Bond (1994) where a numerical study was conducted to determine the effects of wall stiffness (during static loading conditions where $K = K_0$) on the behaviour of propped retaining walls. It was shown that the normalised flexibility number using the soil's stiffness is a feasible parameter that can be used to assess the relationship of both wall and soil stiffness to various parameters such as deflection, bending moment and K_0. The dimensionless modified flexibility number is expressed as follows:

$$\rho^* = \frac{L^4 \cdot E_s^{avg}}{E_w \cdot I} = \rho \cdot E_s^{avg} \qquad \text{Equation 2-4}$$

Where L, E_s^{avg}, E_w and I represent the height of the wall, average soil modulus of elasticity, wall modulus of elasticity, and the second moment of area of the wall respectively. Figure 2-3 details the variation of the normalised maximum moment as the flexibility of the retaining wall is varied. Bending moment was affected to a lesser extent by the stiffness chosen for the soil during the numerical analysis procedure. Walls with greater stiffness showed moments that were four times larger compared to the most flexible walls.

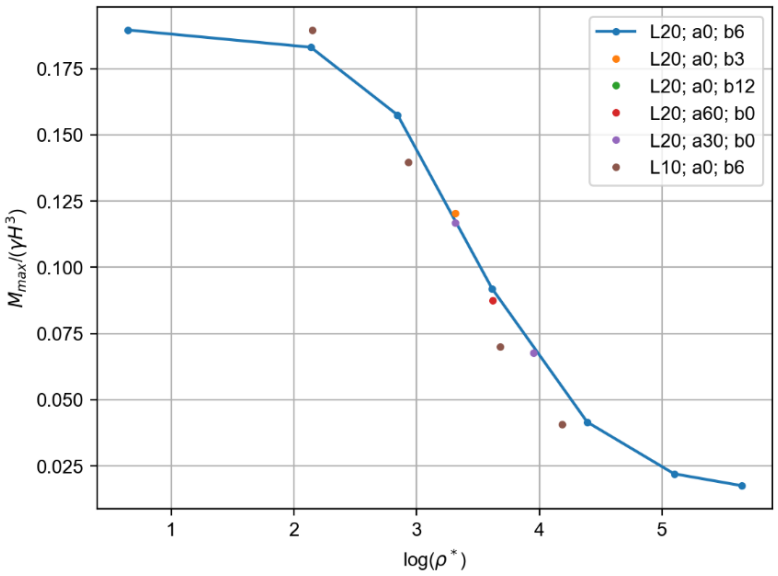

Figure 2-3: Maximum wall bending moment expressed as a function of the normalised flexibility number (Potts and Bond, 1994).

Potts and Bond (1994) found that the normalised flexibility number was better suited for stiff walls where Rowe's flexibility number is best used for more flexible walls with low stiffness values (Figure 2-3). Figure 2-4 is comparable to Figure 2-2 where it can be seen that Rowe's flexibility number is more sensitive and distinguishable for different values of K_0 for lower wall stiffnesses.

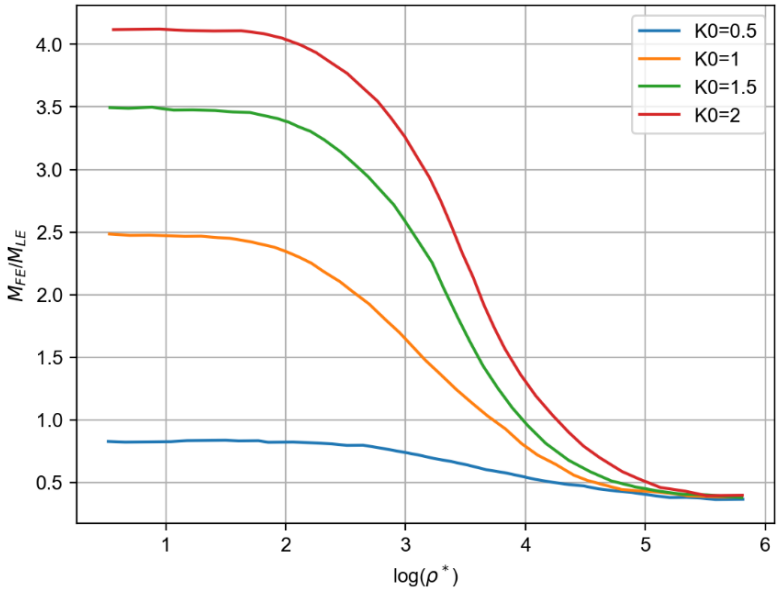

Figure 2-4: Ratio of FEM to Limit State maximum moment expressed as a function of the normalised flexibility number (Potts and Bond, 1994).

Springman *et al.* (1996) utilised another dimensionless normalised version of the Rowe (1952) flexibility number where the expression was multiplied by the gradient of the shear modulus of the soil (denoted as m by the authors) and is written as follows:

$$\rho_{S,N\&N} = \frac{mH^4}{EI} \qquad \text{Equation 2-5}$$

Springman *et al.* (1996) divided rigid and flexible walls in terms of a *dimensionless wall flexibility ratio*. Rigid or stiff walls were defined by a value of $\rho_{S,N\&N} < 200$ and is achieved for shorter diaphragm walls. In contrast, flexible walls are characterised by a value of $\rho_{S,N\&N} > 500$ which include long sheet pile walls as examples of flexible abutments that can reach values upwards of this magnitude.

Addenbrooke *et al.* (2000) conducted research on retaining walls using numerical modelling in order to establish and evaluate the use of a modified *displacement flexibility number* $\rho_{A,P\&D}$ which is based on the work conducted by Addenbrooke (1994 cited in Addenbrooke *et al.*, 2000) for multi-propped wall installed during excavation. From prior research conducted on the displacement dependency of soil-structure interaction, the use of previous flexibility numbers for retaining walls failed to provide a comprehensive context for retaining wall design in terms of the amount of deformation that a wall can achieve and the support conditions at the base and along the height of the wall. The displacement flexibility number derived by Addenbrooke *et al.* (2000) is expressed as follows:

$$\rho_{A,P\&D} = \frac{EI}{h^5} \qquad \text{Equation 2-6}$$

Where $\rho_{A,P\&D}$ has units of kN/m^4 and the variable h represents the spacing of the props in the multiprop configuration of the retaining wall. Thus, larger displacement flexibility numbers would represent stiff/rigid walls and lower numbers would imply flexible/soft walls. Addenbrooke *et al.* (2000) varied multiple aspects in the numerical models which included the

prop stiffnesses, at-rest pressure K_0, number of props used (i.e., the prop spacing h), modulus of elasticity and the Poisson's ratio of the walls. For a given stress regime provided by the stiff clay fill (after excavation) and a certain prop stiffness, the use of the displacement flexibility number defined in Addenbrooke *et al.* (2000) can be used to predict the same maximum lateral wall deflection and ground surface displacement for systems that have similar displacement flexibility numbers.

2.4 Soil ratcheting effect/Strain hardening of soils

The soil ratcheting effect (or also known as the strain hardening effect) can be defined traditionally (with reference to the behaviour of integral bridges) as the flow of soil particles behind an abutment wall where cyclic loading has been applied to the structure through daily and seasonal thermal cycles (causing contraction and expansion of the bridge deck leading to the displacement of the abutment wall away from and towards the backfill respectively). The flow of soil behind the wall will take place downwards along its face and within a portion of the soil mass in the shape of a triangular wedge (Springman *et al.* (1996); Ng *et al.*, 1998a) where a corresponding *densification of the wedge* will take place from particle-interlocking, causing increases in the lateral stresses behind the wall for successive expansions of the bridge deck (or rather passive state movements of the integral bridge abutment) (Springman *et al.*, 1996). Settlements behind the wall can be expected due to the corresponding volume change caused by the densification process and is a significant disadvantage of jointless structures. In other words, for each active perturbation, the soil particles behind the wall will fall into the gap created and will further prevent any additional movement caused by successive passive perturbations (Ng *et al.*, 1998b). An example of one of the earliest works in literature demonstrating the soil ratcheting effect were the experiments conducted by Skinner (1969) which showed that there is a noticeable sliding or rolling action that takes place between course soil particles when subjected to shearing and is accompanied by a corresponding volume change. If the soil mass was at a high density, dilation will be the main mechanism of soil movement.

2.5 Role of active and passive earth movement/pressure

In order for full active pressures to develop in soils, rotations about the bottom edge of a retaining wall of magnitudes 0.0005H and 0.002H are required for soils of high and low relative densities respectively (Clough and Duncan, 1991 cited in Barker *et al.*, 1991; Sowers and Sowers, 1961 cited in Broms and Ingelson, 1971). Clough and Duncan (1991, cited in Barker *et al.*, 1991) conducted a range of experimental and finite element testing on a range of different sand densities where it was found that the movement to reach the passive pressure state required a displacement of roughly 10 times greater than the movement required to reach the active pressure state for a wall height of H. Table 2-1 shows the ratio of wall movement to wall height required to reach both the active and passive pressure states for loose, medium dense and dense sands.

Table 2-1: Ratio of wall movement to wall height required to reach active and passive pressure states (Clough and Duncan, 1991 cited in Barker *et al.*, 1991).

	Values of Δ/H	
Type of backfill	**Active**	**Passive**
Dense sand	0.001	0.01
Medium dense sand	0.002	0.02
Loose sand	0.004	0.04

The earth pressure coefficient (both active and passive) would remain constant after the corresponding maximum wall displacement ratio to wall height was reached for a sand.

Zhang *et al.* (1998) focussed on expanding upon the Coloumb and Rankine methods utilising the strain increment ratio and the angle of internal friction of the soil. Their findings showed that the actual displacement characteristic behaviour of the retaining wall must be taken into account which determines the corresponding active and passive pressure distributions acting on the wall. Five possible displacement shapes were identified where each case would yield different active and passive pressure distributions based on the depth and top displacement of the wall (Figure 2-5). Earth pressure is highly sensitive to not only the properties of the soil but also the properties of the wall and the corresponding soil-structure interaction. Figure 2-6 details the earth pressure distributions for the case where only rotation of the base occurs.

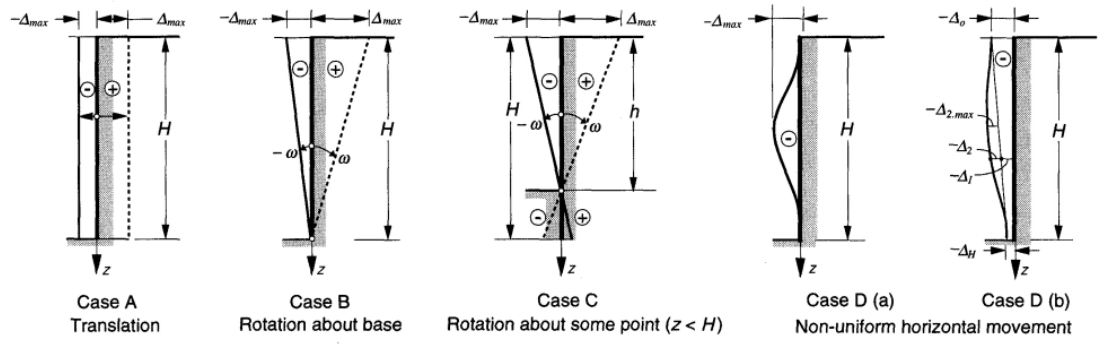

Figure 2-5: Typical models of lateral wall movement for common cases (Zhang *et al.*, 1998).

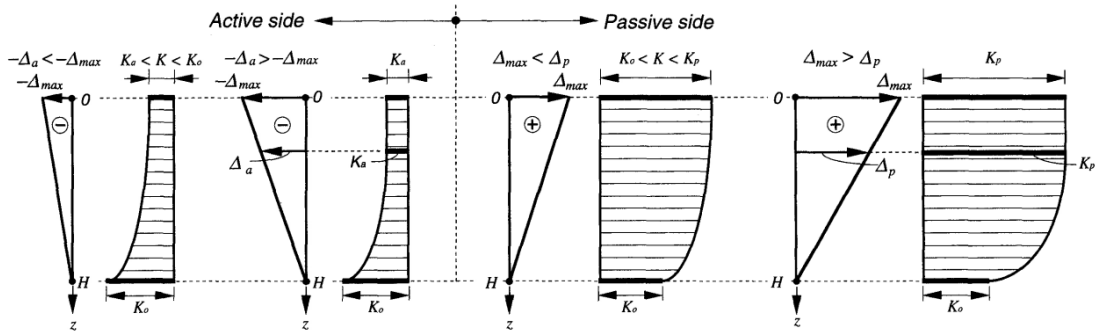

Figure 2-6: Distribution of active and passive earth pressure for the case where only rotation occurs about the wall base (Zhang *et al.*, 1998).

Dicleli (2005) showed that the intensity and shape of the backfill pressure acting on the abutment is a function of the abutment height as well as the stresses generated in the pile

foundations. From their parametric study, non-linear *static pushover* (i.e., thermal load is represented as a linear longitudinal loading) numerical analyses were performed which considered heights ranging from 2 m to 5 m and two different thicknesses to assess the stiffness effects of the abutment. Height of the abutment has a significant effect on the shape and intensity where longer abutments yielded backfill pressures up to 30% larger than the shorter abutments. For the longer abutment heights, the pressure distribution also strayed slightly from the classical triangular distribution assumed using Rankine or Coulomb theory at the base of the walls. Regarding the effects of abutments having either a thickness of 1 m or 1.5 m, negligible difference was found.

For a bridge in Massachusetts (supported by pile foundations), Civjan *et al.* (2004) evaluated earth pressure and temperature data for a 16-month period and reported that after 1 month from measuring the peak pressures, the earth pressures remained stable during the summer and fall months which was postulated to be as result of pressure dissipation in the soil mass from particle rearrangement. The data obtained by Civjan *et al.* (2004) showed that different abutments for the same bridge displayed different levels of earth pressure due to the bridge expanding more at one abutment than the other.

Nam and Park (2015)'s work focussed on a test integral bridge with stub abutments founded on pile foundations where data such as the earth pressure, temperature and bridge movements were monitored over a 3-year period. Earth pressures measured showed a clear trend where pressures measured in later years exceeded those from the year prior in the upper 2 meters (Figure 2-7). It was reported that for passive pressures to initiate, a magnitude of 1% of the total abutment wall height was required either in translational or rotational movement which is in agreement with the findings of Clough and Duncan (1991, cited in Barker *et al.*, 1991) for a dense sand as shown in Table 2-1.

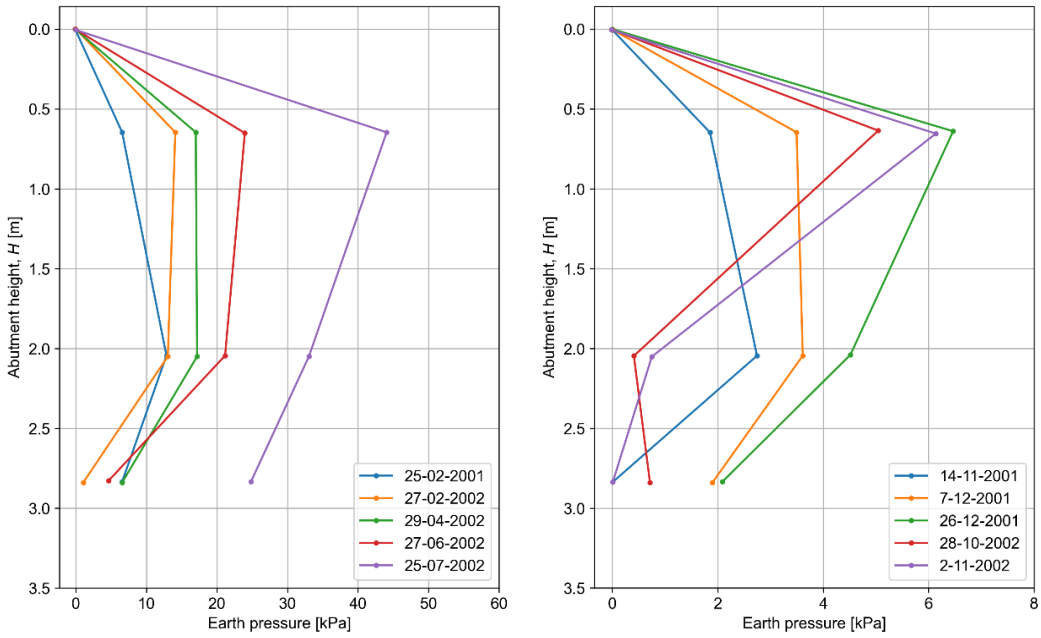

Figure 2-7: Earth pressures measured over 3-year period for (a) passive and (b) active cases (Nam and Park, 2015).

Salman and Issa (2021) performed a calibrated parametric study based on a real integral bridge based on a 7-year monitoring period dataset. The work involved investigating the effects of bridge length, type of soil used, and pile size and orientation. Non-linear soil springs were used to model the soil-pile and soil-abutment interface behaviours with the inclusion of several shrinkage models. Based on their results, it was found that passive movement resulted in less displacement compared to the active case regardless of bridge length where the bridge models displayed a net shortening along its length due to the soil restraining the bridge's expansion over time.

2.5.1 Soil type and particle shape effects

Material properties and behaviour of the soil have a significant influence on the soil-structure interaction that takes place between the integral bridge's abutments and the retained fill. The apparent Young's modulus and surface roughness parameters were found to have an effect on the frictional response of soils (Sandeep and Senetakis, 2018). They found that the inter-particle friction is reduced by increasing the product of the apparent Young's modulus and surface roughness in soils. The research efforts conducted by Clayton *et al.* (2006), Xu *et al.* (2007a) and Xu *et al.* (2007b) - which focussed on the earth pressures developed behind full height abutments of IABs by granular materials including clay - was expanded upon by Bloodworth, Banks and Clayton (2012) who developed a numerical model based on the prior triaxial testing of a stiff clay, sand, and *glass ballotini* for typical stress paths found behind integral abutments. Each material was subjected to lateral strains ranging from 0.05% to 0.2% and density effects were also taken into account by preparing the samples with varying densities for each material (relative densities D_r of 18%, 70%, and 92%). Repeatable behaviour is present for clays without much irreversible strain occurring during cyclic loading (i.e., *resilient behaviour* was present) whereas for the sand the final earth pressures reached magnitudes far higher than the at-rest pressures at the end of the 100-cycle test. Particles with high sphericity were represented by the glass ballotini and showed similar resilient behaviour compared to the clay specimens with no signs of lateral stress increase for increasing number of cycles (Figure 2-8).

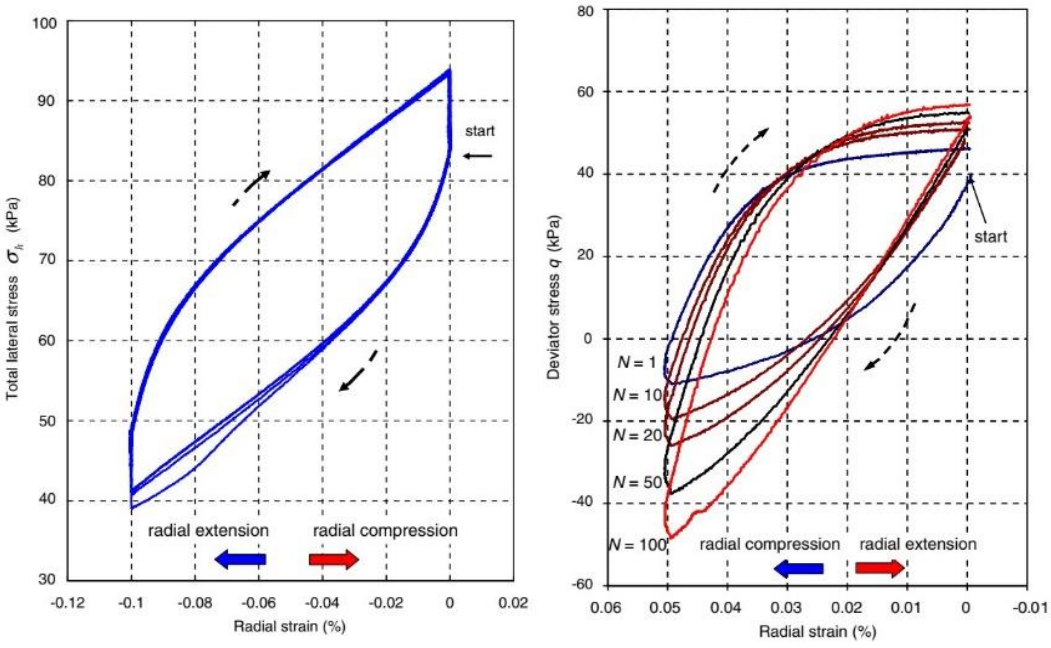

(a) (b)

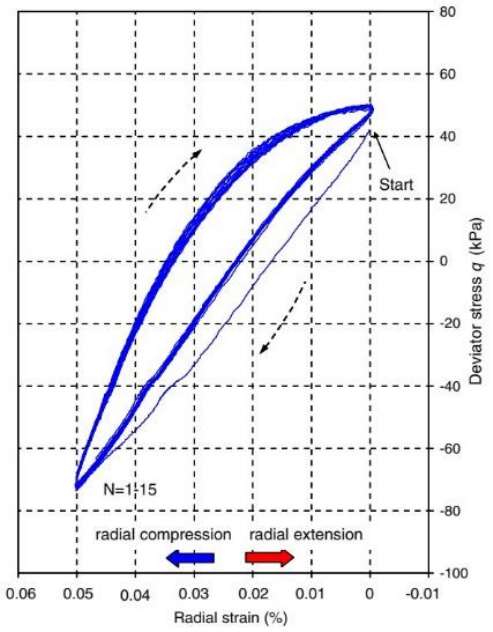

(c)

Figure 2-8: (a) Total horizontal stress for clay. (b) Deviator stresses for sand. (c) Deviator stresses for glass ballotini (Bloodworth *et al.*, 2012).

2.5.2 Soil/Backfill density and compaction effects

A rigid bridge was investigated by Broms and Ingelson (1971) where the abutment faces were instrumented to investigate the earth pressures after compaction of a uniform sand backfill and to identify the required movements to achieve full active and passive conditions. They demonstrated that the earth pressure distribution was highly sensitive in both distribution and magnitude to the *compaction effort* that was applied where the initial pressures were very high immediately after compaction. A rotation of 0.001H was shown to be sufficient to produce

active conditions in the compacted backfill compared to the value of 0.0005H determined by Sowers and Sowers in 1961 as cited in Broms and Ingelson (1971). Passive earth conditions were achieved with rotations equal to a minimum of roughly 0.0013H with maximum earth pressures occurring in the centre along the abutment's height. Clough and Duncan (1991, cited in Barker *et al.*, 1991) showed that for increasing density of the sand, an *increase* in maximum passive pressure coefficient K_p and a *decrease* in the maximum active pressure coefficient occurred. Regarding the effects of compaction, results found in Clough and Duncan (1991, cited in Barker *et al.*, 1991) showed that an increase in the compaction level of the backfill behind retaining walls yielded almost the exact same values for both maximum passive and active pressure coefficients. The at-rest earth pressure coefficient K_0 was shown to increase for increasing compaction level and both the maximum active and passive pressure states would be reached earlier with less required wall movements compared to uncompacted sand.

Clayton and Symons (1992) conducted research on the effects of compaction for clays behind retaining walls where the construction process was taken into account for walls with high resistance to lateral movement. It was determined that the effects of compaction must be taken into account, which is not possible with current classical means of determining the earth pressure against rigid and flexible walls. For clays, the compaction, relaxation and the pore-water pressure dissipation must be taken into account. For a specific clay detailed in Sowers *et al.* (1957, cited in Clayton and Symons, 1992), the lateral pressures (which reached magnitudes greater than the predicted passive pressures) reduced by as much as 30% during the first day of operation. This was the case when compacted to roughly 15% of the soil's plastic limit as a result of pore-pressure dissipation.

Regarding the effects of density on the strain hardening of the sand specimen, Figure 2-9 shows that both dense and loose sand particles are subject to rearrangement and corresponding interlocking of soil grains, leading to the increased earth pressures for the 100 cycles. No apparent plateau is evident based on the results for a strain range of 0.2% for either of the density levels tested (Bloodworth *et al.*, 2012).

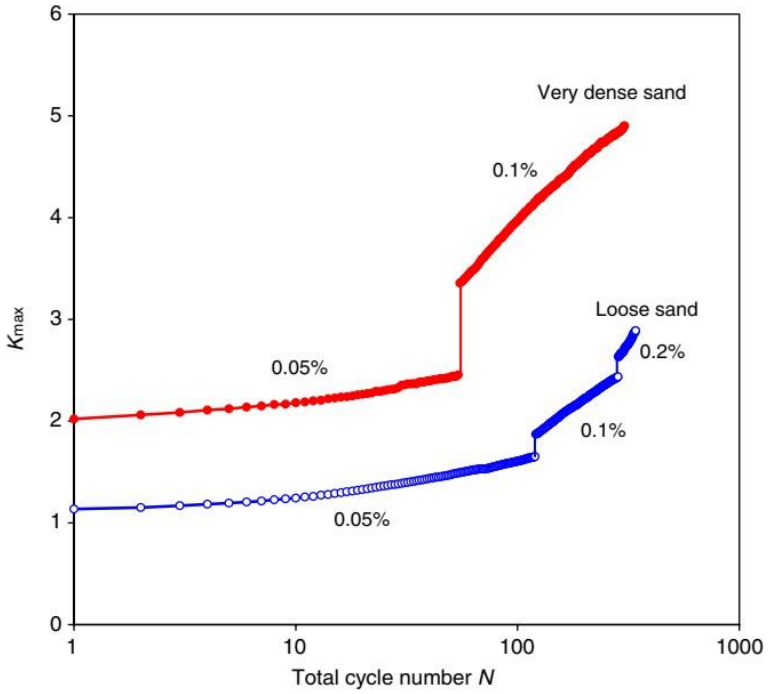

Figure 2-9: Maximum earth pressure coefficient for different densities of the sand specimen (Bloodworth *et al.*, 2012).

2.5.3 Findings from numerical analyses of soil ratcheting/strain hardening

Proper selection of the material model for soils is crucial for accurate numerical modelling of any soil structure interaction problem. The effects of the non-linearity of soils were investigated by Jardine *et al.* (1986) where they developed multiple numerical analyses for different SSI problems such as footings (foundations), piles (comparable to retaining walls), strutted excavation and cavity expansion utilising both linear elastic and non-linear soil properties. Their findings showed that specifically for footings, combining stresses from linear elastic theory and the measured non-linear stress-strain response show reasonable results (e.g., the centre line settlements). For the case of large piles and calculation of wall bending moments using only linear elastic theory is not acceptable to represent soil stiffness.

Faraji *et al.* (2001) formulated a full 3D finite-element model which also incorporated the full nonlinearity of the soil-structure interaction caused by the retained backfill. As the soil reaction against the abutments are interdependent on the magnitude and mode of deformation/deflection of the wall/abutment, nonlinear springs were utilised along the full height of the abutment wall and the piles. The force-deflection design curves detailed in the National Cooperative Highways Research Program (NCHRP, 1991 cited in Faraji *et al.*, 2001) design manual was used to define the spring constant coefficients for all the springs located along the abutment only. For the piles the nonlinear *p-y* curves documented in the American Petroleum Institute (API, 2003 cited in Faraji *et al.*, 2001) are used instead to better represent their soil-structure interaction. A more realistic distribution was obtained compared to the classical triangular distribution as it is expected that the nonlinear pressures will be greater closer to the ground surface and lower at the support or base of the abutment wall (lower soil

movement/deformation). The peak moments in the piles decreased by about twice the amount when compaction density was increased from a loose state to a denser state and the maximum moment was found to occur at the abutment-pile interface. The level of soil compaction was thus identified as a significant factor that must be taken into account which can affect the overall bridge's behaviour. Axial forces in the superstructure girders should not be neglected in the design as the magnitude of the axial forces vary greatly with compaction level of the backfill.

Banks and Bloodworth (2018) numerically modelled the behaviour of the soils behind integral bridges during seasonal and daily thermal changes based on the material model developed by Banks (2009) and Bloodworth *et al.* (2012) (which was based on a sample of Leighton Buzzard sand) and compared their findings to current design standards employed by both BA 42 and PD 6694-1. Their numerical model produced peak earth pressures up to 60% lower at mid-height compared to BA 42 and favoured PD 6694-1 more closely for bridges up to a total length of 60 m. The peak lateral stress eventually propagated downwards for increasing number of cycles and the stresses at the surface showed a stabilising trend. The inclusion of daily cycles in the analyses accounted for an increase in approximately 10% in the peak stresses developed in the soil.

Caristo *et al.* (2018) conducted numerical analyses using PLAXIS 2D and evaluated the effects of the initial movement direction (termed the *interaction mechanism* in their work) during cyclic loading of IABs due to temperature change as well as evaluating the feasibility of using recycled tyres for the purposes of a compressible inclusion material. It was found that during the first 15 cycles the pressure build up rate was faster for the contraction-expansion case but for increasing cycles up to 120 the two mechanisms showed virtually no difference for their recorded lateral stresses (Figure 2-10).

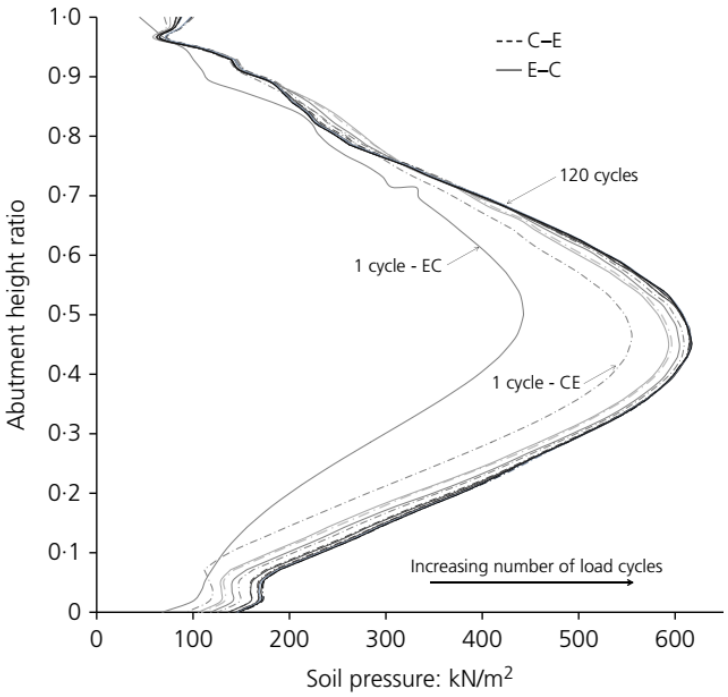

Figure 2-10: Pressure development on conventional abutment (Caristo *et al.*, 2018).

Walter *et al.* (2018) conducted large-scale experimental testing on river washed pea gravel placed in a 1524 x 1219 x 762 mm steel box which was loaded cyclically using a steel stiff wall connected to a hinge at the base for a total of 10 cycles at a displacement magnitude of 13 mm. A corresponding numerical study was calibrated using the experimental results in the PLAXIS software package using the hyperbolic soil hardening constitutive model. Care was taken to create the model as close to reality by including the effects of backfilling layers of 150 mm thick increments. The study placed focus on the lateral earth pressure behaviour during cyclic loading where the numerical results can be seen in Figure 2-11.

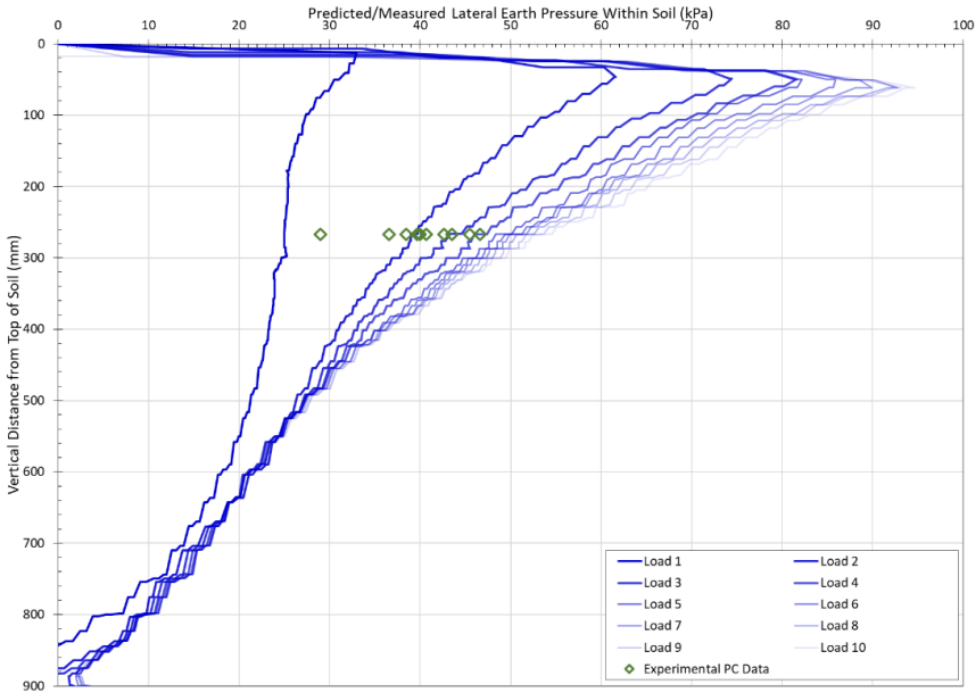

Figure 2-11: Lateral earth pressure within soil adjacent to moving wall for each inward cycle compared to experimental data (Walter *et al.*, 2018).

Walter *et al.* (2018) demonstrated that the greatest earth pressures occur in the upper portion of the wall (in contrast to the triangular distribution approximated using Rankine's earth pressure theory) and that the pressure increase reduced for increases in the number of cycles (numerical and experimental data were in good agreement).

Sandberg *et al.* (2020) conducted a calibration study for a numerical model developed using PLAXIS 2D (HS constitutive model for soil) for the Heathrow Expansion Project. The bridge in question measured at roughly 140 m long which is one of the longest integral bridges in current operation. A complete SSI analysis was performed and compared to the standard *limit equilibrium method* (LE) which is used in some design codes. Reference is also made to England *et al.* (2000)'s findings where their derivation for earth pressure along the depth of the wall is also compared to the findings of the numerical study. The authors varied the lengths of the abutment (ranging from 9 m to an exceptionally large value of 17 m – both having a wall thickness of 2 m) and allowed for a total of 120 years as the design life of the bridge. The earth pressure distributions from the study are shown in Figure 2-12.

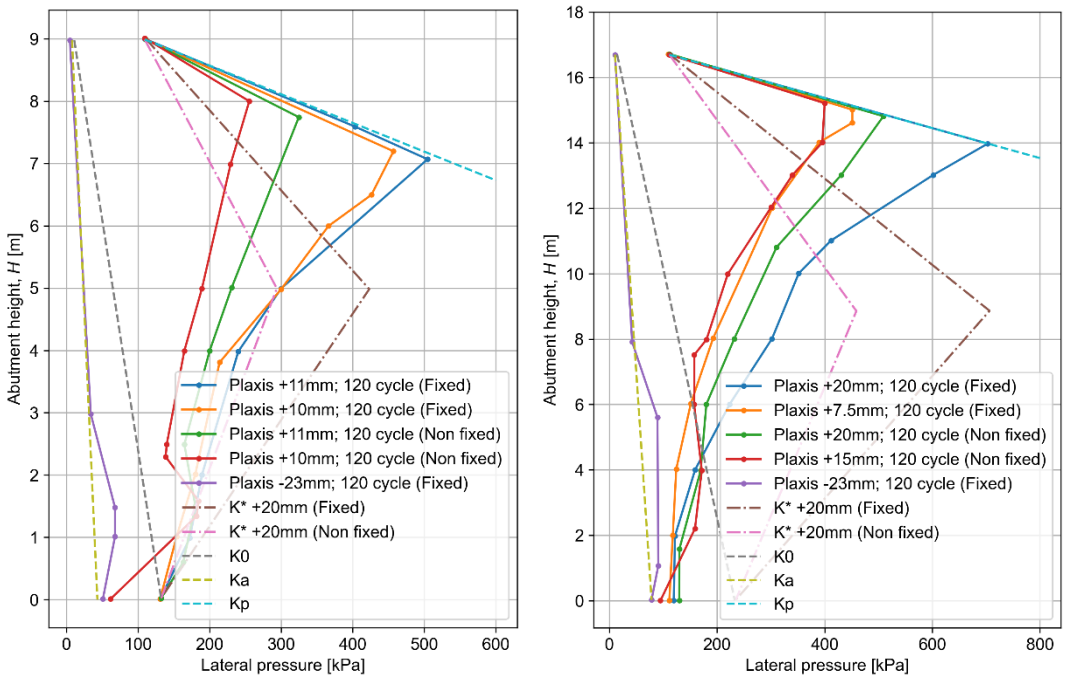

(a) (b)

Figure 2-12: Earth pressure distribution along depth for a) 9m and b) 17m high abutments (Sandberg *et al.*, 2020).

Most noticeable is the fact that there is clear distinction between the LE method and the numerical results where the computed distribution yielded its peak pressure much higher in the abutment stem rather than at the midpoint as predicted by England *et al.* (2000)'s empirical relationship. Sandberg *et al.* (2020) also suggested that the magnitude of thermal expansion is influenced (directly proportional) by the stiffness of the soil.

The use of discrete element modelling is a new technology that has been used to better represent the behaviour of particulates (especially soil grains) for numerical/analytical modelling compared to previous 2D and 3D representations of soil-structure interaction. A 2D discrete element study was conducted by Alonso-Marroquin and Herrmann (2004) where the response of cyclic loading of soils were investigated using convex polygons that were generated at random. From their analyses, it was evident that the evolution of the volume ratio was sensitive to the initial random structure of the generated polygons, which seems to suggest that the initial orientation of the soil grains plays a noteworthy role during the ratcheting process of soils. Xu and Guo (2021) conducted a discrete element study to investigate the effects of strain-controlled cyclic loading applied to granular materials on the earth pressures that are developed behind integral bridge abutments. Their models utilized clumped particles consisting of multiple spheres to simulate non-spherical grains of soil. Loose samples tend to have much greater degrees of volume reduction compared to dense samples where dense samples routinely display a greater tendency to dilate rather than reduce in volume. After a small number of cycles, the micro-structure of the grains can produce large lateral stresses due to the change in micro-structural arrangements of the particles. Xu and Guo (2021) showed that for a particle arrangement consisting of only perfectly spherical particles, no significant pressure increase due to cyclic loading was computed in their analysis. Hadda and Wan (2018)

conducted a 2D DEM study focussing primarily on the micro- and macroscopic behaviour of retained soil during monotonic and cyclic loadings. Through bisection of both Coloumb's and Roscoe's solutions angles (denoted as θ_C and θ_R respectively in Figure 2-13), a decent approximation for the angles of the sheared zone can be determined during active and passive failures for *monotonic* loading conditions (Figure 2-13). They also demonstrated with their numerical model that an asymptotic state is reached after a determined number of cycles (which in turn depends on the density, stress level and loading amplitude/magnitude).

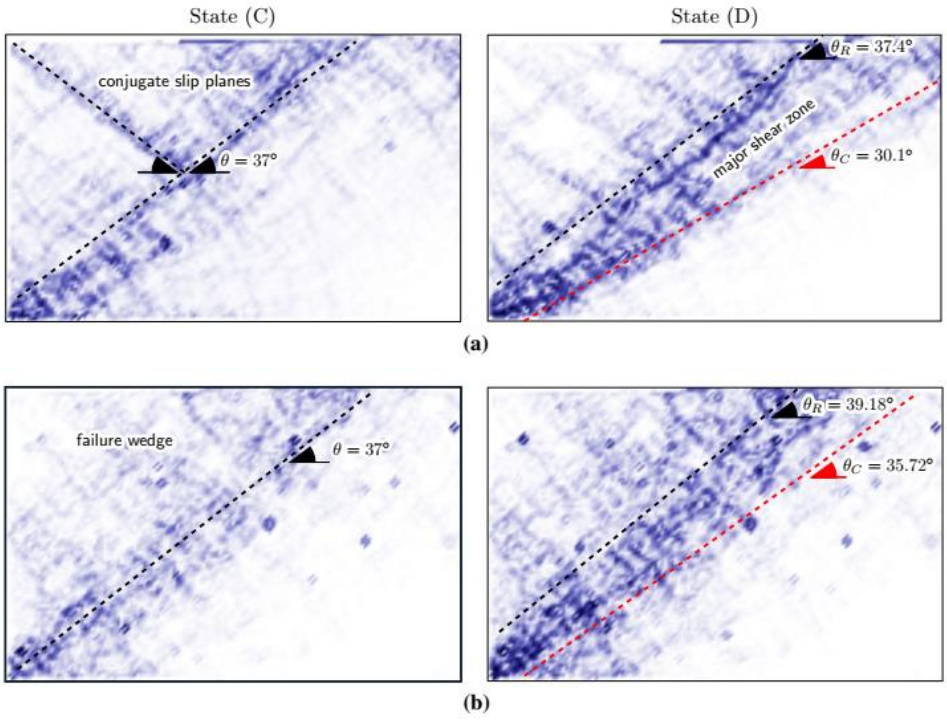

Figure 2-13: Deviatoric strain fields for C and D states during passive pressure for (a) dense soil and (b) medium dense soil (Hadda and Wan, 2018).

Hadda and Wan (2018) found that during cyclic loading of the soil, the dense soil revealed loosening in terms of the granular assembly in contrast to the medium dense soil that showed further densification of the assembly. The hysteresis loops demonstrated the stiffness evolution of the assembly as well as the progress of the asymptotic state. All loops were centred at the neutral position (x = 0) and at a mean force value (which in turn is also a characteristic of the asymptotic state). As can be seen in Figure 2-14, high velocity movement of particles are more commonly found directly behind the retaining wall and zones of high shearing are more commonly found at the bottom wedge of the confined area (termed the *dead zone* by the authors). This zone of mobilized soil is larger for the medium dense specimen and that the dead zone size decreases for increasing displacement magnitude.

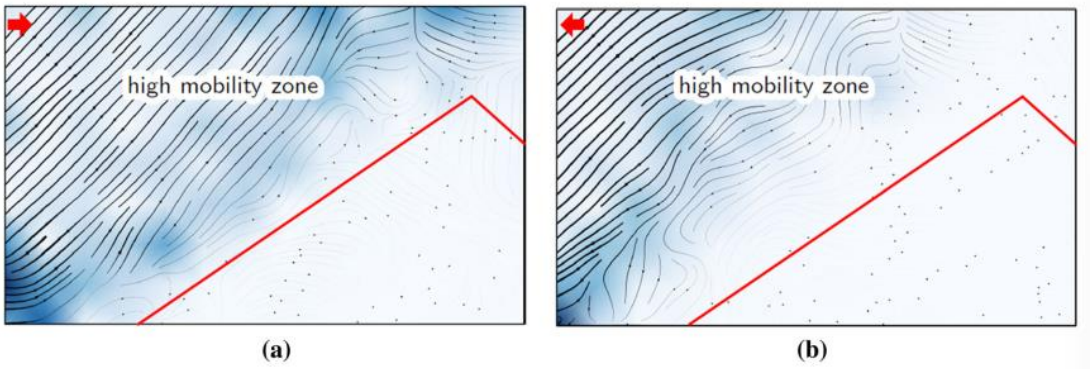

Figure 2-14: Streamlines indicating regions of high mobility as well as the dead zones during cyclic loading for (a) half-way pushing (x=0) and (b) half-way pulling (x=0) (Hadda and Wan, 2018).

Ravjee *et al.* (2018) conducted numerous numerical DEM (Discrete Element Method) tests which focussed on investigating the effects of particle sphericity (different polyhedral shapes) on the soil behaviour behind IABs during cyclic thermal change. High sphericity demonstrated gradual densification and increases in pressure and was present in the entire backfill region. For low sphericities, the pressure increases were found to be more rapid with localised densification occurring at the abutment-soil interface zone (due to particle interlocking effect). The results of the DEM study demonstrated that integral bridge construction is benefitted by soil of high sphericity.

2.6 Results from scale model testing

Springman *et al.* (1996) conducted a multitude of centrifuge testing on fine sub-angular silica sand (particle size range of about 90-150 μm) using prototype models made from DURAL (i.e., a high strength and low weight alloy consisting of an Aluminium, Copper and Magnesium composite) and were subjected to the effects of seasonal and daily temperature variations. Testing included an extreme cycle taking place once in the estimated 120-year design life of the bridge structure (a temperature change of roughly 46°C), daily cycles where temperatures are varied between day and night, and more significant cycles taking into account the seasonal variation of temperatures between summer and winter. Settlement occurred for all tests and the highest pressures were located at a distance of 1/3 H and were generally higher for the stiffer walls. The *wall roughness* was a critical parameter as greater values of roughness lead to an increase in the maximum achievable passive earth pressure K_p. Stiff walls were found to rotate rather than bend and were subject to greater moments and flexible walls deformed much more in terms of flexure. The overall bending moments were found to increase by as much as 30% for embedded walls for increasing number of cycles. Ng *et al.* (1998a) conducted further centrifuge experiments for spread-base integral abutments. Their testing incorporated the effects of Serviceability Limit State (SLS), Ultimate Limit State (ULS) and 1 in 120-year expansions of the bridge (summarised in Table 2-2).

Table 2-2: Controlled displacements used during centrifuge testing (Ng *et al.*, 1998a).

Event:	Nominal controlled displacement (prototype) [mm]	Nominal rotation at deck level [degrees]
Daily (SLS)	± 6	± 0.06
Daily (SLS)	± 12	± 0.12
Annual (ULS)	± 30	± 0.29
1 in 120-year cycles (extreme case)	± 60	± 0.58

In their work they found that sliding of the base (translational motion) was a concern for integral abutments and cannot be neglected in their design. At ULS conditions, the V-shaped failure wedge that forms (Figure 2-15) developed after a total of 100 cycles with the increase in pressure taking place being larger at the position of the deck compared to the rest of the height of the wall for both dense and loose sands.

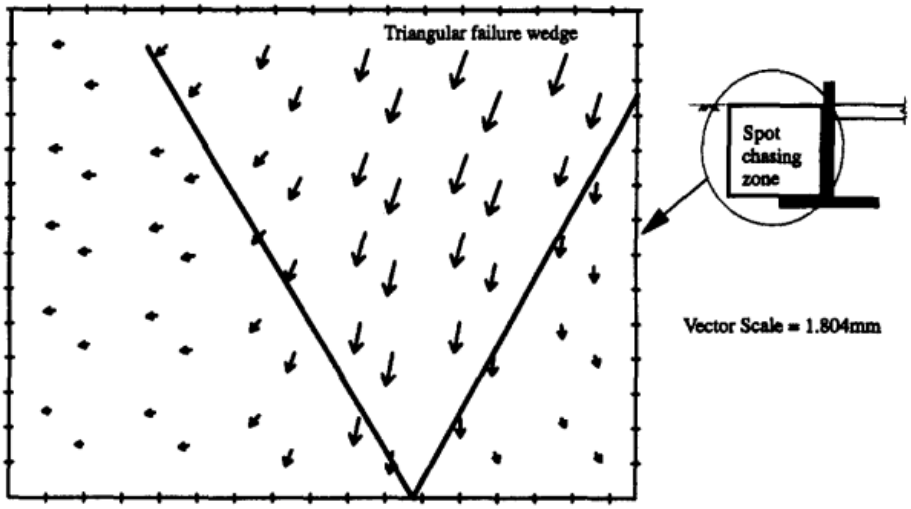

Figure 2-15: Displacement vectors and V-shaped failure wedge after 100 cycles (Ng *et al.*, 1998a).

They also found that the lateral earth pressure increased with the amplitude of the displacements for each passive movement, however at a decreasing rate with the presence of a plateau (upper limiting value) revealing itself after the 100 cycles mark. For both dense and loose retained sand, Ng *et al.* (1998a) found that the earth pressures resulting from ratcheting action was more than twice the at-rest pressures (K_0) where the loose sand specimen reached a higher earth pressure magnitude than the dense soil.

England and Tsang (2000; 2001), England *et al.* (1997), and England *et al.*, (2007) conducted important research on the design of integral bridges to resist lateral soil pressures that increase over time due to the strain hardening phenomenon. Similar centrifuge testing was done compared to Ng *et al.* (1998a; 1998b) where Leighton Buzzard sand was subjected to cyclic loading by rotation at the base of a stiff wall. Both daily and seasonal cycles were investigated where close attention was paid to the lateral stresses and their relationship to the top displacement to overall height ratio (d/H) as well as the deformation behaviour of the retained fill. England and Tsang (2000; 2001) and England *et al.* (2007) reported that a steady-state value (or rather plateau) can be achieved after approximately 100 to 200 seasonal cycles where

roughly 50% of this increase was already reached after only 20 cycles. This plateau of stress escalation is directly proportional to the magnitude of the applied displacement (d/H ratio) per cycle (Figure 2-16), but important to note that although dependent on the d/H ratio's magnitude, the stress is not dependent on the previous history of the stress and strain in the soil. The presence of daily cycles in combination with seasonal cycles did not produce significantly larger stresses after each cycle compared to only subjecting the wall to seasonal cycles but did increase the soil settlement and deformation at the wall interface (England and Tsang, 2001).

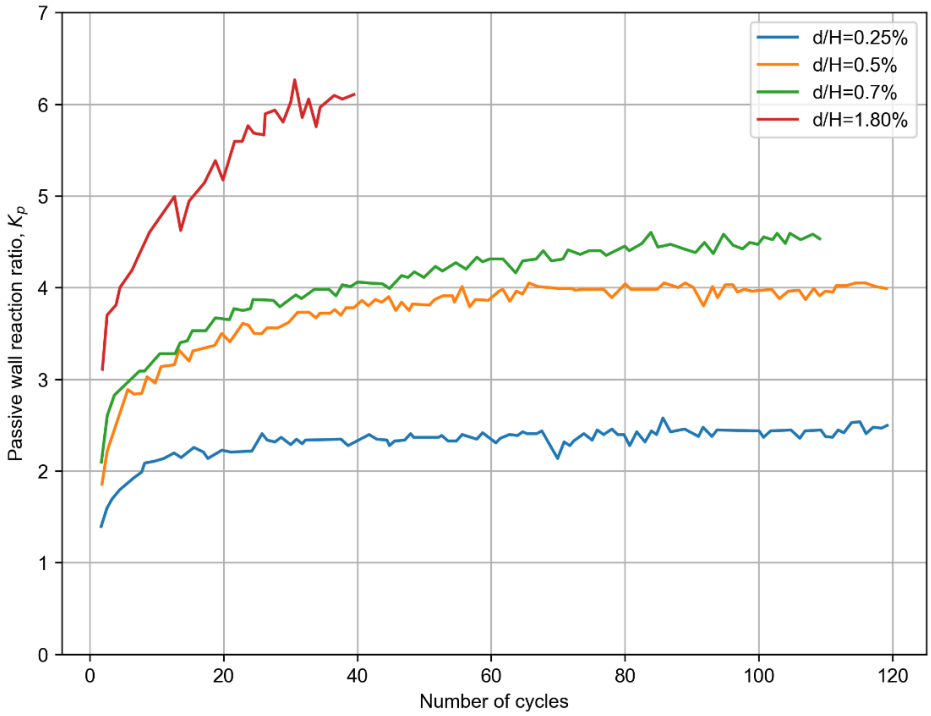

Figure 2-16: Variation of K with the number of cycles for varying d/H ratios (England and Tsang, 2000; 2001).

Each cycle results in the densification of the soil but will also cease at the plateau point where only settlement of the soil surface will persist due to the ratcheting action (i.e., only the flow of soil particles will continue). England and Tsang (2000; 2001) and England *et al.* (2007) concluded their work by providing an empirical relationship for predicting the passive earth pressure coefficient for the design of integral bridge abutments:

$$K^* = K_0 + \left(\frac{d}{0.03H}\right)^{0.6} K_p \qquad \text{Equation 2-7}$$

Lehane (2011) conducted 40g centrifuge testing to assess the effects of seasonal cyclic loading on the earth pressure stresses generated behind deep abutments (heights ranging from 4 m to 6.5 m for the prototype) of integral bridges. Rotations about the *hinged base* of the abutments were in the range of 0.05% to 0.6% for Δ/H. The models were constructed using a dry silica sand for all tests and were subjected to a total of 100 cycles. Based on the data shown in Figure 2-17, the authors noted that the stress profiles are not sensitive to different heights of the hinge above the rigid boundary and the same can be said for different abutment heights (taking into account the variability of the soil's relative density D_r).

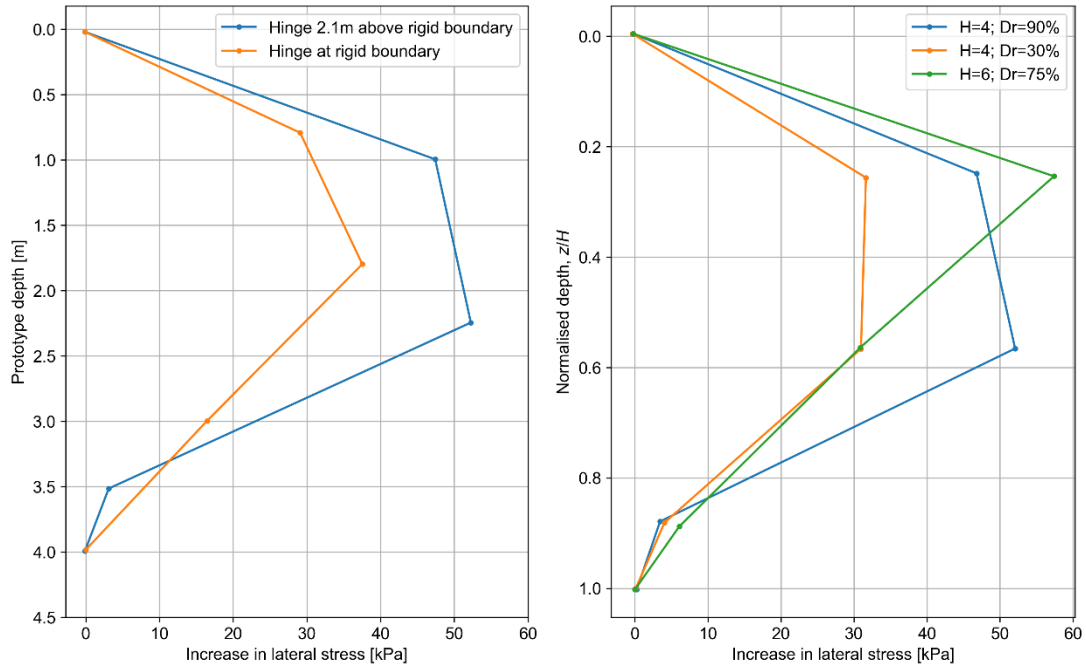

(a) (b)

Figure 2-17: Maximum increases in lateral stress for (a) different depths to rigid boundary and (b) different abutment heights (Lehane, 2011).

Lehane (2011) reported that a cyclic amplitude of less than 0.1% causes insignificant increases in the maximum potential stress initiated by an individual cycle. After 100 cycles, the authors concluded that the rate of stress increase is relatively small.

Cosgrove and Lehane (2003) assessed the behaviour of a laboratory scale model of a spread-base abutment of an integral bridge where loose backfill (dry siliceous sand) was loaded cyclically. A 25 mm thick mild steel plate (298 x 1100 mm) was chosen to represent the abutment and allowed to rotate about its base (hinge support) in a 2.61 (L) x 1.36 (H) x 0.3 (W) chamber made from steel with a laminated glass sheet for the front face of the box (Figure 2-18).

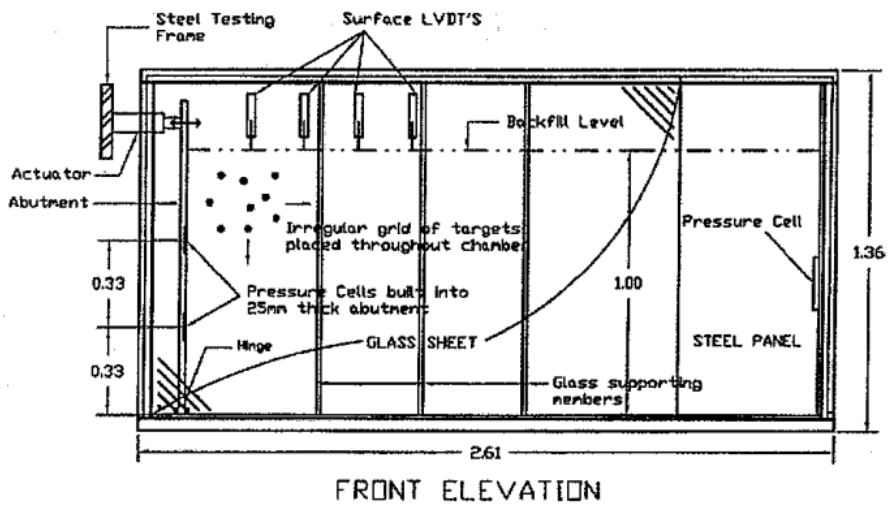

Figure 2-18: Chamber housing steel abutment for experimental setup (Cosgrove and Lehane, 2003).

The backfill was subjected to two tests where test 1 and test 2 were subjected to 120 and 500 active-passive cycles with a displacement amplitude of ±6 mm and ±2.3 mm respectively at 1 m above the base hinge position. Significant strains associated with strain ratcheting took place but did not show any tendency to approach a constant value for increasing number in cycles (Figure 2-19) as was the case in England *et al.* (2000). The maximum possible coefficient of lateral earth pressure was found to be significantly larger than the Rankine passive earth pressure coefficient for all tests.

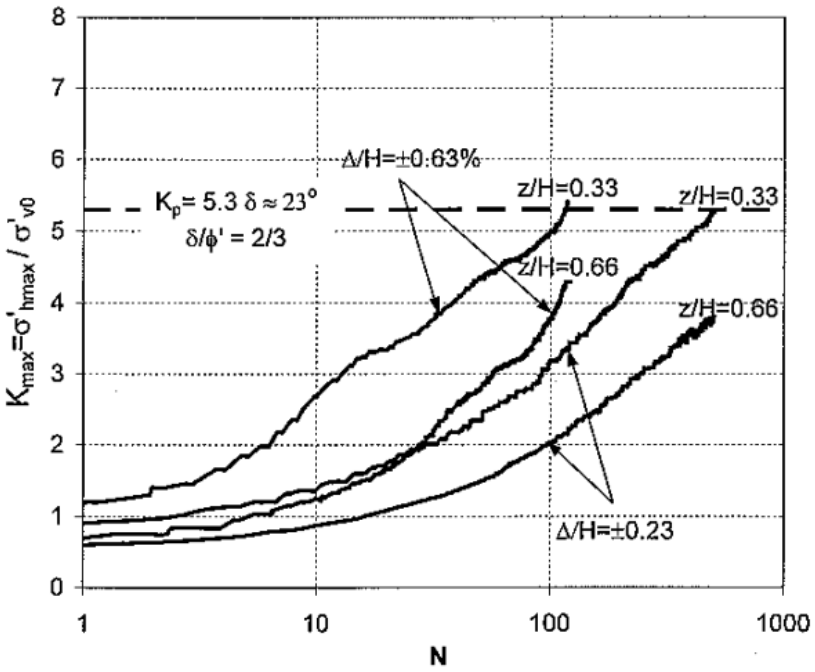

Figure 2-19: Maximum lateral earth coefficient variation with number of cycles (Cosgrove and Lehane, 2003).

Settlement at the interface between the abutment wall and the retained fill was found after testing and was proportional to the number of applied cycles. A triangular zone (or wedge) was formed at roughly a distance of H/3 from the interface whereafter little soil particle movement took place (Figure 2-20).

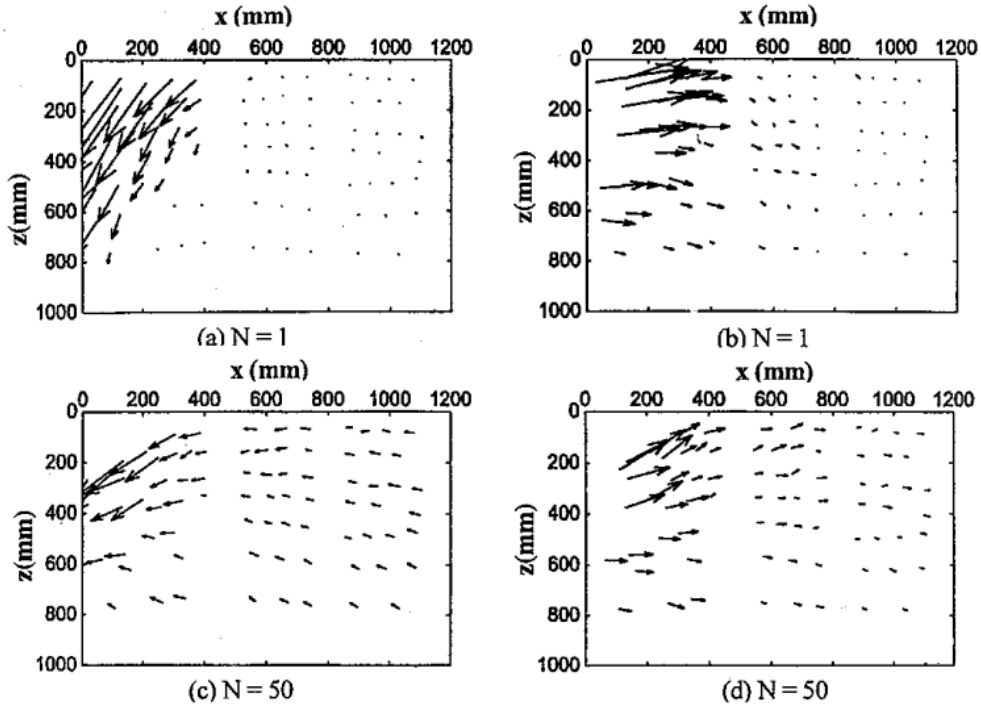

Figure 2-20: Active and passive vectors for cycles 1 and 50 during test 1 (Cosgrove and Lehane, 2003).

Luo *et al.* (2022) conducted a literature review and small-scale experiments that evaluated the effects of wall stiffness, loading rate, and the displacement history of the abutment of an integral bridge. A total of 3 small-scale tests were performed in a 1525 x 1050 x 1150 mm timber box with glass panels located on each face which allowed for PIV (Particle Image Velocimetry) analyses (Figure 2-21).

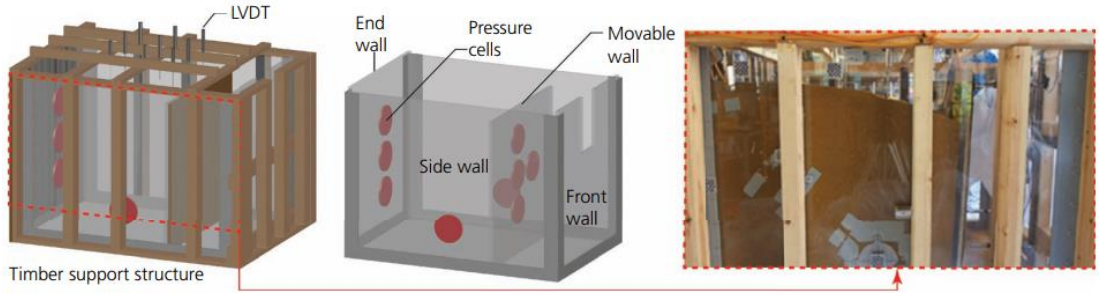

Figure 2-21: (a) 3D Diagram of test setup and (b) box filled with soil (Luo *et al.*, 2022).

The wall stiffness was evaluated by considering 2 types of walls with a length of 1000 mm: (1) a wall made from 25 mm PMMA (Plymethylmethacrylate) plates which sandwiched a 25 mm thick timber plate which represented a movable/flexible wall and (2) a wall made from a 25 mm PMMA and 50 mm aluminium plate combination with a 25 mm timber plate that represented a rigid wall. Amplitudes commenced at ±5 mm and were increased by 5 mm every second cycle until the final maximum amplitude of ±30 mm was reached. The loading rates of 0.5 mm/s and 1 mm/s were evaluated for each wall. From their experimental findings, the maximum recorded pressures at the end of testing were higher than predicted by Rankine and

PD 6694-1. After the 12th cycle, the pressures measured for the stiffer wall were higher compared to the flexible wall. The backfill surface settlements for the rigid abutment were slightly larger after 12 cycles, but this was most likely as a result of the larger loading amplitude. Settlements increase rapidly for increasing cycles regardless of wall thickness.

2.7 Conclusion

The current research efforts that have focussed on the effects of abutment stiffness on ratcheting of the embankment soil have mostly consisted of many numerical analyses of full-scale integral bridge abutments and analysis of experimental data obtained from centrifuge testing and small-scale abutments using materials that are not representative of the materials used in the construction of real in-service integral abutment bridges. In general, experimental testing of small-scale abutments are made from steel/aluminium materials/composites which are used to represent the abutment of an integral bridge which behaves fundamentally different compared to reinforced concrete and interacts differently with the adjacent soil (e.g., frictional forces along the interface between the abutment and embankment soil) and can crack if exposed to large enough forces. From the literature, it was evident that there does exist an influence due to the stiffness of the abutment walls as well as the type of soil used, but the effects are unknown for scale abutment testing using reinforced concrete.

It was thus decided to experimentally investigate the effect of abutment stiffness on the soil stresses that develop behind the abutment due to cyclic loads resulting from bridge deck expansion. This was achieved by constructing scale abutment-deck specimens made from reinforced concrete which retained a fine silica sand to represent the worst-case scenario for thermally induced ratcheting behind integral bridge abutments. Reinforced concrete was used to more accurately represent the soil-structure interaction problem for real integral abutment bridges.

3 Experimental setup

3.1 Introduction

The following chapter details the experimental setup and the measured material properties of the specimens.

A scaled experimental test was designed where abutment specimens made from reinforced concrete of varying thickness were tested in a steel strong box which provided complete confinement of the embankment sand. The abutments were cast monolithically with a portion of the deck in order to investigate the overall behaviour of the deck-abutment joint connection and its role in the ratcheting process.

The purpose of this chapter is to detail the experimental setup that was designed to house the concrete abutments and the sand as well as to present the material properties of the concrete and the sand used for the experiments. The chapter also aims to detail the setup process that was done for each test sample and abutment-deck specimen and explains the decisions made with respect to the cyclic loading process based on prior research conducted and the project's limitations.

Figure 3-1: Complete test setup for an abutment-deck specimen.

3.2 Concrete abutment walls

Based on the literature study conducted, a fundamental decision was made to select concrete as the material of choice for the abutment specimens as no other laboratory scale test has been conducted (including centrifuge testing) where actual reinforced concrete was used besides the general choice of aluminium or steel for the abutment structures.

Concrete is fundamentally a non-linear material as opposed to metal where the modulus of elasticity is much easier to quantify (in terms of its linearity). As such, the behaviour cannot be expected to be representative of a true structure such as prior models that were developed in the geotechnical centrifuge as seen in literature. In an effort to relate the true behaviour of the influence of abutment stiffness on the ratcheting phenomenon in real integral bridges, the abutment specimens were developed at roughly small scale and designed as reinforced concrete members.

Due to the fact that the sand was expected to exhibit the *flow behaviour* as referenced in the literature study, there would most likely also be an influence on the results simply due to the surface roughness of the concrete as opposed to using a metal such as aluminium or steel. Due to the presence of the deck member and joint at the top of the abutment specimens, possible cracking at the interfaces could occur which could allow moment redistribution in the structure, which is not possible for the current experiment if aluminium or steel was used.

It is acknowledged that aluminium and steel are appropriate for use in specific scenarios during geotechnical centrifuge testing. However, based on the current existing knowledge of the ratcheting effect and the influence of earth pressure escalation on the behaviour of integral bridges, the non-linear effects of concrete have proven to be absent in literature and too important to be excluded and simplified by using a linear elastic metal material for testing purposes.

In order to assess the effects of abutment stiffness on the ratcheting phenomenon, it was decided that a total of 5 specimens were to be cast, each having a different thickness abutment but the same deck dimensions. Abutment thicknesses varied with 25 mm increments starting at the most flexible abutment having a thickness of 50 mm and ending with the most rigid abutment having a thickness of 150 mm (i.e., the thicknesses considered for the experimental testing consisted of 50 mm, 75 mm, 100 mm, 125 mm, and 150 mm for the abutments). All abutment specimens were cast with a 50 mm thick reinforced concrete slab which represented the half portion of the deck of an integral abutment bridge. The reinforced concrete abutment-deck specimens can be seen in the photos in Figure 3-2.

The abutment specimens measured 300 mm across their width with the intention of producing plane strain conditions. It should be noted that the influence of the scaled deck and abutment width on the backfill behaviour was not assessed due to the plane strain assumption and deemed beyond the scope of the study.

(a)

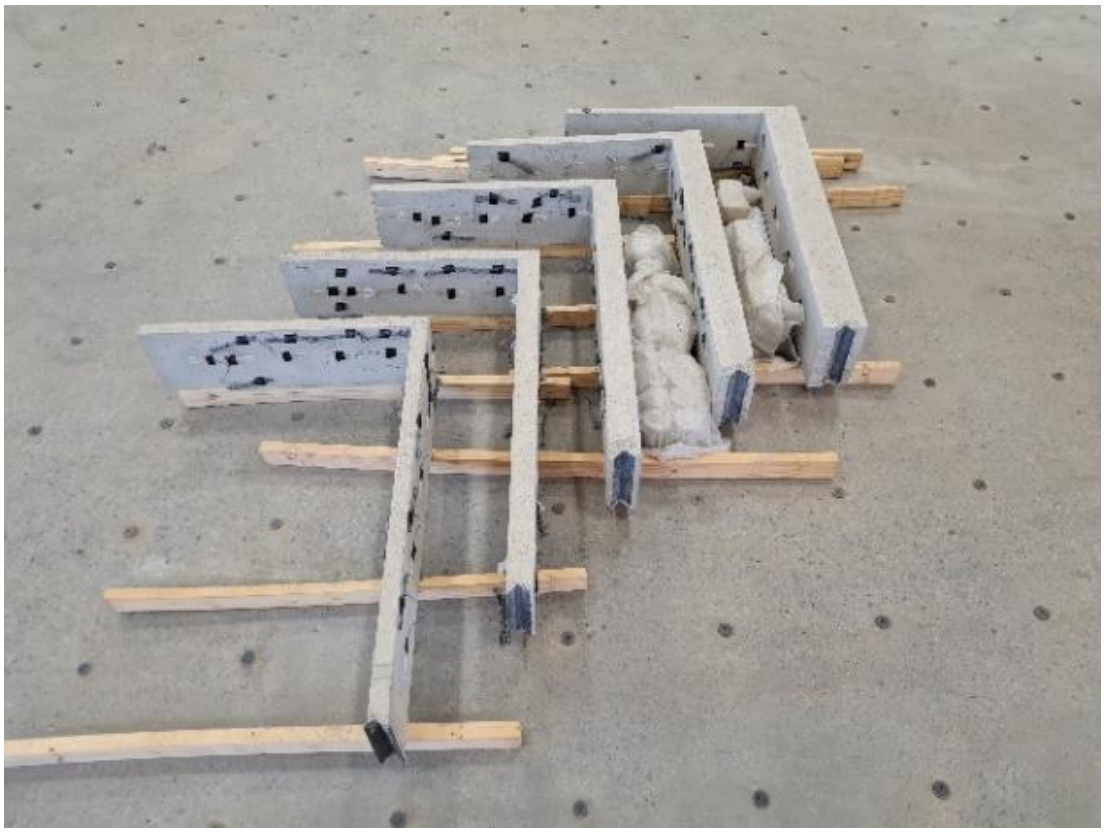

(b)

Figure 3-2: (a) Reinforcing details of (b) cast specimens.

3.2.1 Reinforcement layout and type of reinforcing used

The reinforcement used consisted of 5 mm steel mesh (true diameter of 4.7 mm) where the joints and ends of the abutment and deck were further reinforced using 6 mm rebar steel (true diameter of 5.75 mm). The reinforcement is shown in Figure 3-3.

Figure 3-3: Steel reinforcement layout for the abutment specimens.

The abutments were heavily reinforced (refer to Table 3-1) in order to reduce the possibility of cracking (although it is acknowledged that no amount of steel can prevent cracking and that post-cracking stiffness may be influenced during testing) and non-linear plastic behaviour occurring during testing and to also ensure that the deflection/bending/deformation characteristics of the walls and deck remain in the linear elastic zone, such that equilibrium and section properties were simplistic enough to determine with reasonable accuracy. It is acknowledged that the restriction of the strain range of the concrete specimens to the linear-elastic range is a significant limitation of the study and was mainly implemented for the purpose of reducing the study's scope.

The joint at the deck and abutment intersection was heavily reinforced with the 6 mm rebars to ensure that proper moment transfer can occur (Figure 3-4).

Figure 3-4: Joint reinforcing for proper moment transfer.

Each abutment specimen contained an identical amount of reinforcing and the quantities of steel used for the abutment specimens are shown in Table 3-1. It should be noted that the choice of equal steel reinforcement provided to all specimens was assumed to be adequate to reduce the possibility of cracks forming during any given experimental test provided that the strain ranges remained in the elastic strain range.

It is acknowledged that the complexity of mixed parameterisation of flexural stiffness (and likely also crack width and spacing) may influence experimental results without the ability to distinguish the cause thereof.

Table 3-1: Quantities of steel used for the abutment specimens.

Specimen (denoted by abutment thickness):	% steel reinforcing by volume:
50 mm	4.40
75 mm	3.38
100 mm	2.75
125 mm	2.31
150 mm	2.00

The bases of the abutments were all reinforced using 50 x 50 x 4 mm tapered angle welded to five 6 mm rebar bars that extended 300 mm into the concrete. The angle served as a *pin connection* at the base of the wall (Figure 3-5).

Figure 3-5: Angle connection at the bases of the abutment specimens.

The end connections for the deck portions of the abutment specimens were constructed in a similar fashion where the rebars were welded to a 4 mm flat bar (Figure 3-6). The purpose of the deck's end plate was to allow for a custom-made mounting bracket that could be fastened to the force transducer-actuator setup.

Figure 3-6: Deck end connection for the abutment specimens.

3.3 Test setup for the specimens

A custom-built steel box was designed and constructed for the experiments of all the scale abutments. This section details the steel box (the outer frame and the glass panel door), the instrumentation used during each experiment, the concrete abutments, and the loading setup (actuator).

3.3.1 Steel frame strong box frame

Based on Cosgrove and Lehane's (2003) findings, any movement of soil further than roughly 30% of the abutment wall's height from the face of the wall revealed negligible displacements. As such, these findings largely influenced the size of the steel frame strong box designed for the tests conducted in terms of boundary effects and economical constraints.

The frame mainly consisted of 75 x 75 x 4 mm square hollow steel sections which were welded together to ensure that the frame was as rigid as possible to minimise the deflection of the sides of the box and to ensure that the sand and concrete abutment specimens were *constrained* during testing. To combat sand spilling out of the steel frame, 5 mm thick steel sheeting was welded to the back, bottom, and one of the sides. Thus, the 2 remaining sides were blocked off by the concrete abutment specimen itself and a steel doorframe which housed a 1000 x 1600 mm laminated glass panel which had a thickness of 37.52 mm (a sufficiently strong panel was required to reduce the possibility of the glass panel failing due to the increase in pressure during cyclic loading). The frame's detailed dimensions are shown in Figure 3-7.

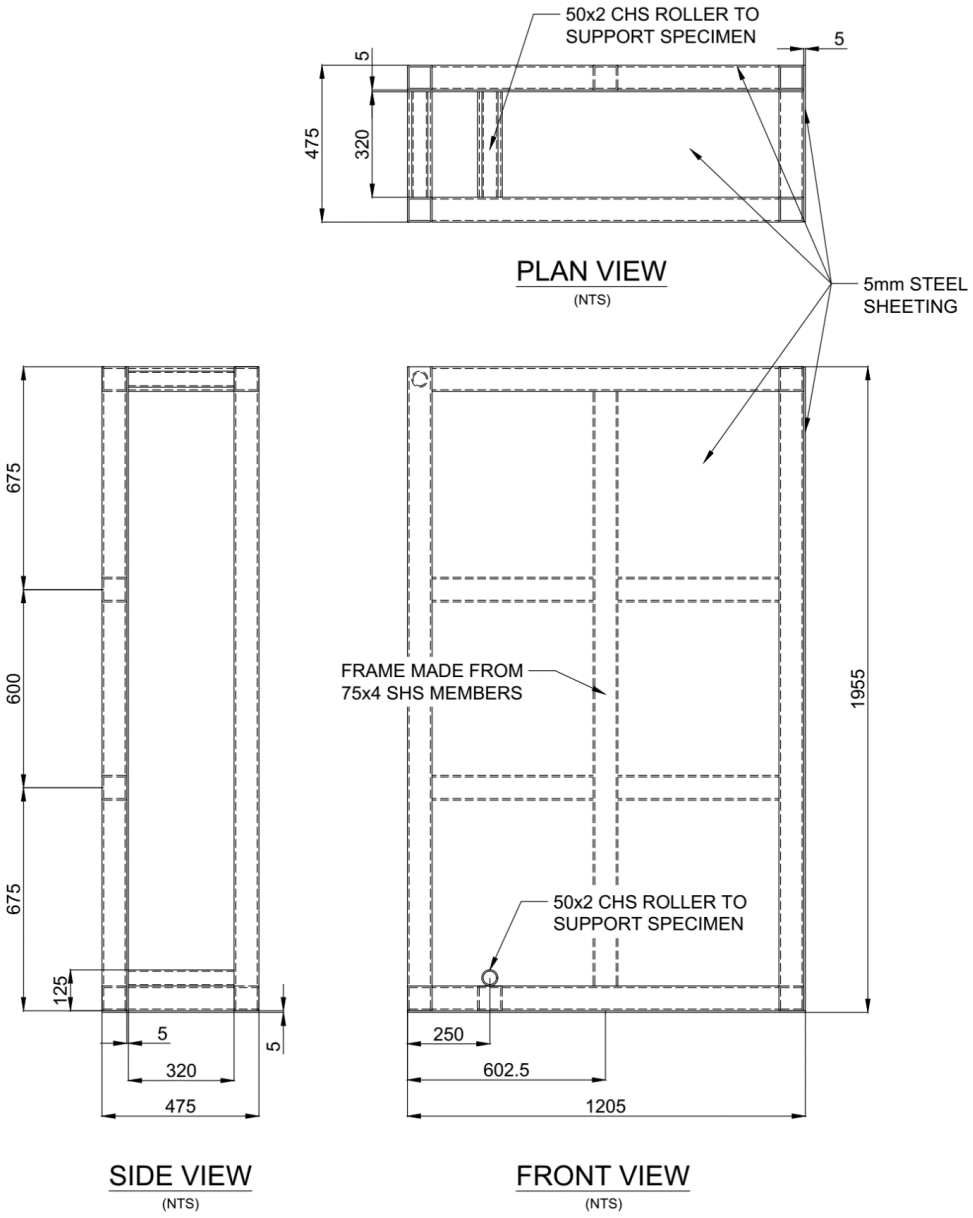

Figure 3-7: Steel box detail.

The completed steel box frame was designed to be bolted onto a concrete strong-wall and strong-floor (Figure 3-8). This allowed the box to stay stationary during testing and to further ensure that minimal deflection of the back steel sheet was taking place (which was the most critical surface since it was in the direction of the cyclic loading being applied to the concrete specimens and hence the sand in the steel frame box). The thickness of the strong-wall and strong-floor measures 500 mm and 1000 mm respectively.

It should be noted that it is not known whether the steel frame strong box experienced any inelastic strain or permanent deformation during testing of the specimens and was assumed to provide adequate rigid confinement. The effects of any potential inelastic strain or permanent deformation of the steel frame strong box were deemed beyond the scope of the study.

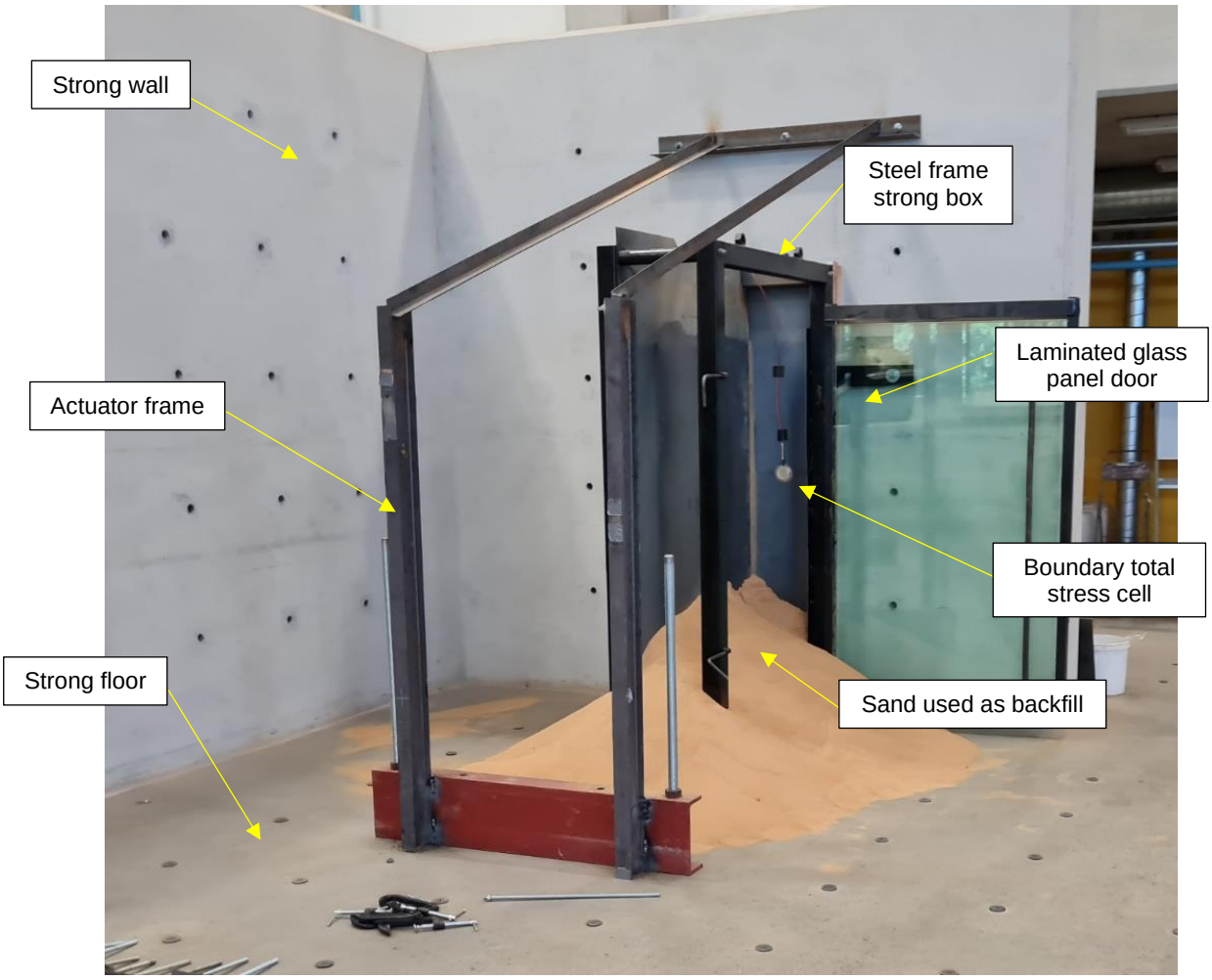

Figure 3-8: Concrete lab strong wall and strong floor.

3.3.2 Roller base for abutment specimens

A 50 x 2 mm circular hollow section was welded to a 75 x 75 x 4 mm square hollow section (also shown in Figure 3-7) at the bottom of the steel box frame situated 250 mm away from the front end of the box. This circular hollow section serves to provide minimal displacement of the abutment wall base in the horizontal and vertical directions whilst still allowing rotation of the base. Therefore, the connection is theoretically assumed to be a *hinged connection* for equilibrium calculation.

The vertical and horizontal displacements were restricted solely by the self-weight of the specimens that were simply lowered onto the circular hollow section by resting the angle that was welded to the reinforcing frame at the base of the specimens on the pipe positioned at the base of the steel frame strong box.

3.3.3 Steel doorframe and glass panel

The steel frame strong box was designed to allow the application of *particle image velocimetry* (PIV) analysis on the sand that was loaded cyclically in order to assess the

deformation/displacement magnitudes and deformation/displacement patterns of the sand retained behind the abutment specimens. Thus, a steel doorframe was designed to house the 1000 x 1600 mm laminated glass panel such that the sand displacement was visible and could be photographed during testing.

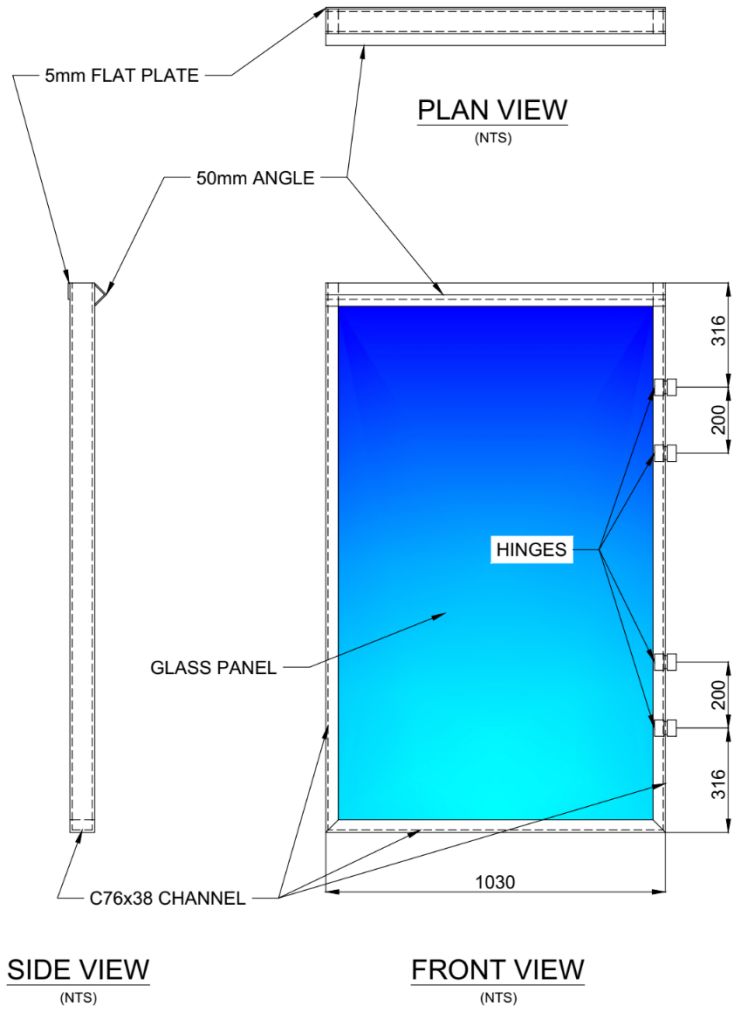

Figure 3-9: Steel doorframe detail.

The PIV setup (Figure 3-10) required the use of a stationary digital camera that was mounted onto a tripod and positioned roughly 2.75 m from the face of the glass panel. Multiple spotlights were positioned towards the glass panel and a large tarpaulin was hung behind the camera to reduce any glare and other reflected light to provide the best possible image quality for use during the PIV analyses. The image capture rate was set to a frequency of 0.1 Hz (1 image every 10 seconds).

GeoPIV-RG (Stanier *et al.*, 2015) was used to analyse the sets of images for each test with a selected patch size of 200 pixels spaced at 100-pixel intervals for all analyses that were

conducted in order to compensate for the relatively large distance from the glass panel whilst still providing meaningful detail in terms of calculated displacements of the sand particles.

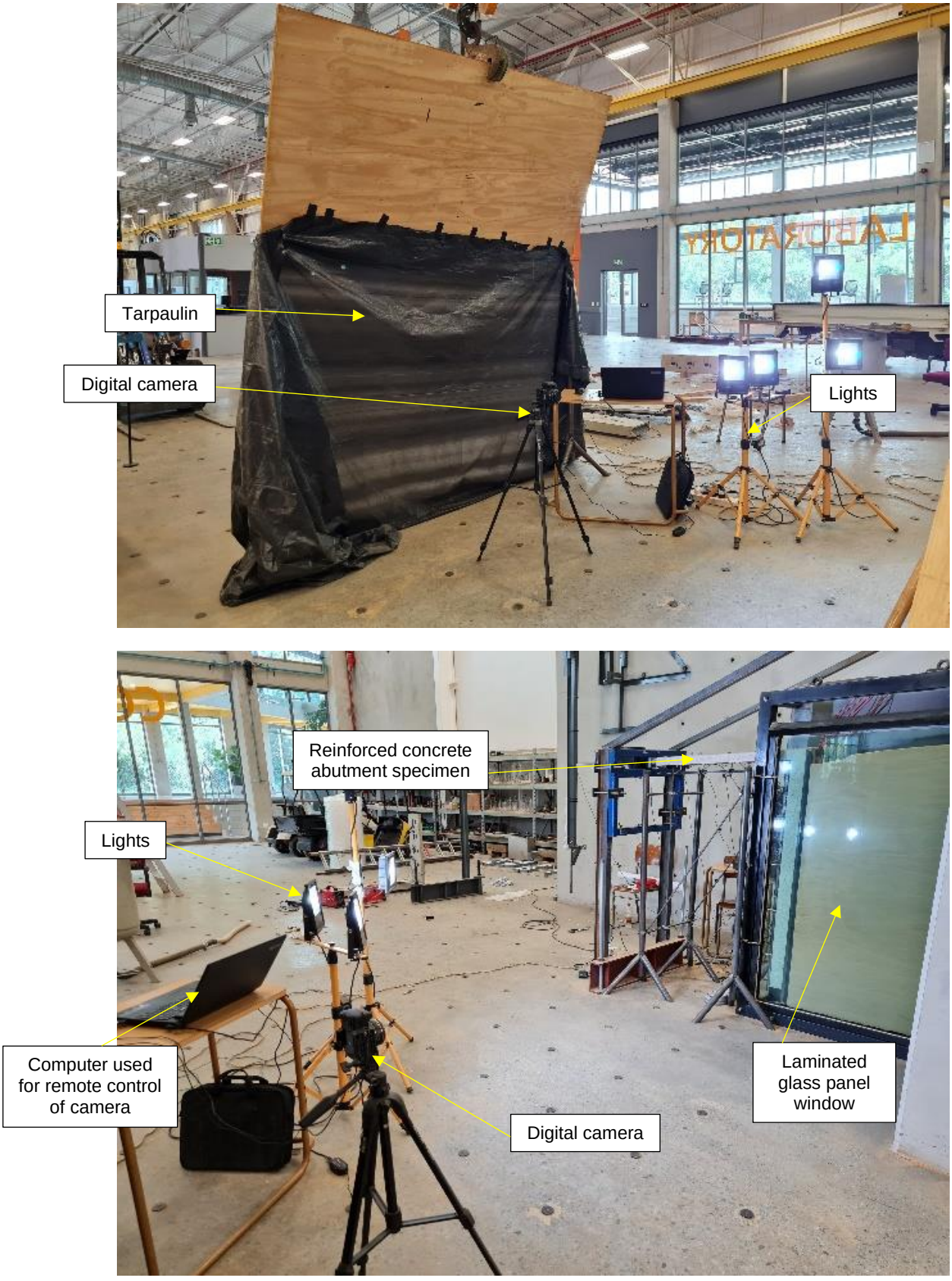

Figure 3-10: PIV setup.

The steel doorframe (Figure 3-9) consisted of 76 x 38 x 5 mm tapered channel sections for the sides and the bottom of the frame. The top of the doorframe was connected at the back and front edges with a 50 x 5 mm thick flat bar and 50 x 4 mm tapered angle respectively to allow for the glass panel to be lowered into the doorframe and at the same time to ensure the frame remains rigid enough during cyclic loading. The frame itself was lined with 5 mm thick rubber padding to protect the glass panel's edges from cracking during fitting into the frame and during testing. The panel was secured permanently into the frame using strong silicone adhesive along the front and back edges.

3.3.4 Basic setup procedure for any given abutment

The setup procedure for any given test was performed by first ensuring that the abutment wall was lowered correctly into place where the side of the abutment that was facing the steel panel side of the box was sealed using masking tape (Figure 3-13). The side facing the glass panel door frame was sealed using multiple layers of sealing strip which was stuck to both the abutment being tested as well as the glass panel to minimize the deterioration of the strips in order to ensure that the friction caused from displacing the abutment back and forth is kept as consistent as possible (Figure 3-13). The angle profile cast into the base of each abutment was placed onto the roller in the steel frame strong box.

In order to load the abutment walls cyclically using the actuator, a stiff frame was also constructed that would allow minimal displacement of the frame along the direction of the load being applied. The frame consisted of two vertically placed IPE100 I-beams that were mounted onto a horizontal PC 230 x 90 parallel flange channel section that was fixed to the floor using 50 mm diameter threaded rods. The actuator's frame was also secured to the strong wall which the steel box was placed against in order to further reduce any possible deflection due to the loading being applied. This connection was achieved by welding 50 mm angle profiles to the top of the two vertically placed I-beams spanning over the length of the steel box and again fastened using the 50 mm diameter rods to the strong concrete wall. The actuator itself was connected to its own frame that was fastened to the I-beam frame using flat bars that were bolted to each other. This design compensated for the variation in the dimensions of the abutment specimens and could be lowered and raised as needed to suit the height of the deck end plates.

The LVDTs used for measuring the deflection of both the abutment wall and the deck portion were then installed using a frame which was constructed from 50 mm circular hollow sections and multiple 12 mm lengths of rebar (Figure 3-11, Figure 3-17). The LVDT frame was designed as a modular frame which allowed specific positioning of the LVDTs for any abutment that was tested.

The LVDT frame was positioned for the abutment specimen being tested and secured using appropriate bracing to ensure that the deflection caused during cycling of the abutment did not result in deflection of the LVDT frame. Friction between the vertical LVDTs used for measuring the deflection of the deck portion was minimised by using duct tape to ensure that sliding could occur.

Figure 3-11: LVDT frame used for connecting all LVDTs (abutment wall and deck portion).

A pin connection (allowing rotation but no vertical displacement) between the jack and the end of the deck was achieved by welding two 20 mm thick pieces of steel to a piece of 5 mm thick flat bar which was then welded to the end of the deck (Figure 3-6).

3.3.5 Filling technique used for sand

The sand was placed into the steel box using *air pluviation*. A large steel hopper (Figure 3-12) was filled and hoisted over the top of the box in order to pluviate the sand easily. A 2.5 m long pipe was used to allow for a constant free fall height of 1 m to achieve consistent relative density of the sand mass after pluviation for all the abutment specimens that were tested. A total of 6 loads of the hopper were necessary to completely fill the steel frame strong box with the abutment specimen inside.

Figure 3-12: Hopper used to pluviate sand into the steel box.

3.3.6 Interface connections between the abutment specimen and the glass panel and steel sheeting

To eliminate the possibility of sand leaking out at the concrete interfaces between the 5 mm steel sheet and the glass panel surface, different techniques were employed to provide a tight seal where no sand particles can escape during cyclic loading. The simplest solution was used for the steel sheet interface where multiple layers of masking tape were used to seal the interface and this proved sufficient even at higher pressures during ratcheting of the sand as the view is completely obstructed (Figure 3-13).

The glass panel interface to the concrete wall proved to be the most difficult challenge as a solution was required that simultaneously allowed not only unobstructed movement of the wall, but also provided sufficient visibility of the sand directly against the concrete wall face for the PIV analyses (which the masking tape approach was not suitable for). A sealing strip was stuck to both the concrete wall side surface and the glass panel (Figure 3-13). This interface allowed movement with minimal friction whilst still providing the necessary confinement of the sand and allowing a sufficiently clear view of the sand against the concrete abutment face for PIV purposes.

Figure 3-13: Sealing strips used for concrete-glass interface and masking tape used for the concrete-steel sheeting interface.

3.3.7 Actuator and force transducer setup

A linear actuator (capable of 50 mm displacement) was used to load the abutment specimens using displacement control. The actuator was mounted to I-beams that were fastened to the concrete strong wall (Figure 3-14). Movement of the actuator was controlled by hand (i.e., manually) during all experimental tests to ensure consistency and reliability in terms of the displacement magnitude and number of cycles. A 50 kN force transducer/load cell (Figure 3-14) was connected to the end of the actuator and was mounted to a custom-made bracket (Figure 3-15). This connection allowed for horizontal movement and rotation only and was

assumed to resist all vertical forces generated during testing (i.e., it was assumed that the support at the end of the deck functioned as a perfect roller support).

Figure 3-14: Actuator positioned onto mounting frame.

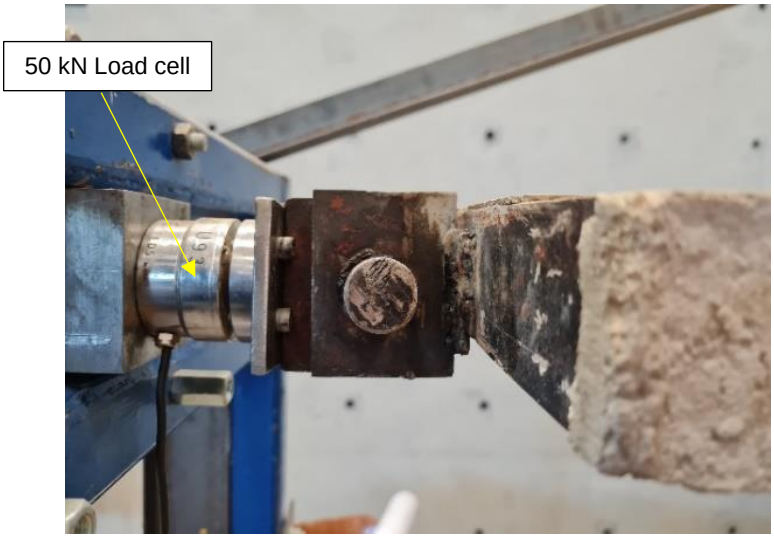

Figure 3-15: Custom-made mounting bracket for load cell and actuator.

3.4 Instrumentation used for abutment-deck specimens

The strains in the abutment walls as well as the deck portions that developed from the ratcheting cyclic loads caused by the adjacent sand were measured using *strain gauges* stuck to opposite sides at fifth points along the length of both the deck and the abutment parts as can be seen in Figure 3-2 and Figure 3-16.

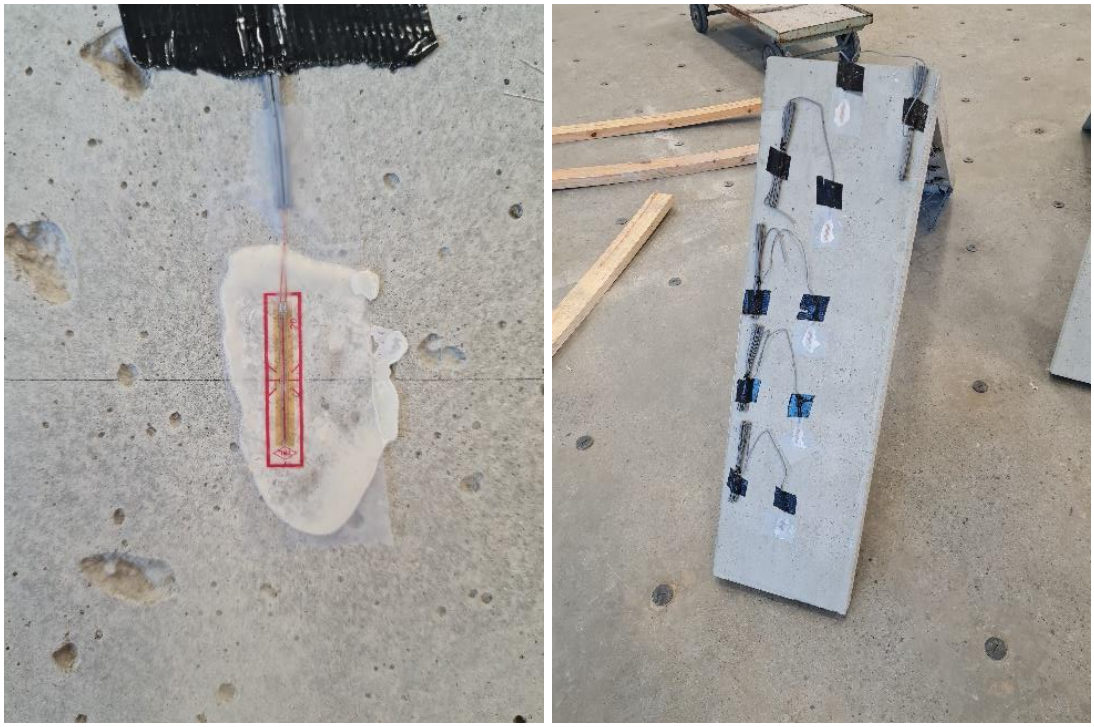

Figure 3-16: Strain gauges glued to concrete abutment specimens.

All abutment walls were instrumented identically where the strain gauges were positioned starting from each specimen's inside joint corner. Wheatstone quarter-bridge strain gauges were used to measure the strain on the surfaces of the concrete. The five locations positioned along the length of the abutment wall corresponded to both the locations of the LVDTs used as well as the earth pressure sensors in order to allow possible back-calculation of data measured (deflection of the concrete and horizontal earth pressures in particular). The placement of the instrumentation is indicated in Figure 3-17.

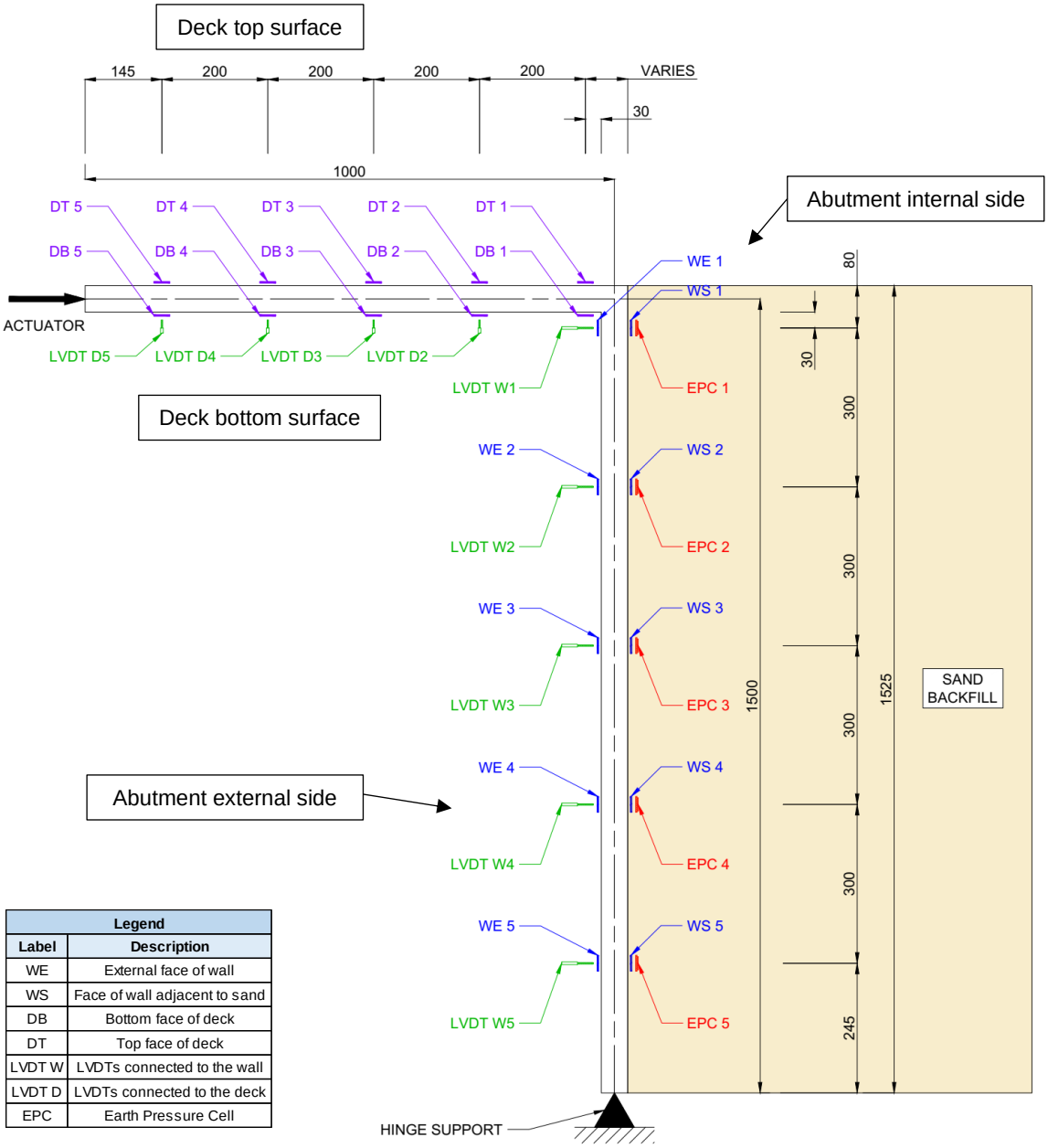

Legend	
Label	**Description**
WE	External face of wall
WS	Face of wall adjacent to sand
DB	Bottom face of deck
DT	Top face of deck
LVDT W	LVDTs connected to the wall
LVDT D	LVDTs connected to the deck
EPC	Earth Pressure Cell

Figure 3-17: Sensors installed onto abutment specimens (dimensioned).

The strain gauges were bonded to the concrete after adequate surface preparation which involved thorough sanding of the concrete surface and proper choice of placement of the gauges at locations where there were insignificant indentations/holes in the concrete which could potentially jeopardise the strain measurements of the gauges. A strong bonding agent (X60 cold curing glue) was used to ensure proper adhesion of the gauges to the concrete material and to fill any possible small holes in the concrete. Each strain gauge was covered with both a layer of electrical tape and a layer of duct tape to prevent any accidental damage to the instrument. A total of 20 gauges were installed per experimental specimen (10 gauges each for the deck and abutment wall). The manufacturer's gauge specifications are detailed in Table 3-2.

Table 3-2: Strain gauge manufacturer specifications.

Gauge property:	Value/Description:
Strain gauge length	20 mm
Gauge resistance	118.5 ± 0.5 Ω
Gauge factor	2.12 ±1 %
Temp. compensation	$11x10^6$ /C
Manufacturer of gauges	Tokyo Sokki Kenkyujo Co., Ltd.
Gauge type	PFL-20-11-3LJC-F

Using the strains measured by the gauges, the bending moments can be calculated using Equation 3-1:

$$M = \frac{(\epsilon_1 - \epsilon_2) \cdot E_c \cdot Z_c}{2}$$ Equation 3-1

Where:

ϵ_1 = Tensile strain measured by a particular strain gauge

ϵ_2 = Compressive strain measured by the strain gauge positioned opposite to ϵ_1

E_c = Modulus of elasticity (Young's modulus) of the concrete

The deflection of the abutment wall and the deck portion was measured using 50 mm (HBM WA-T/50 mm) and 10 mm (HBM WI/10 mm) L*inear Variable Differential Transformers* (LVDTs) respectively, positioned in line with the strain gauges installed on each part. The size of the steel frame strong box's outer frame allowed for the installation of only 4 LVDTs onto the deck portion. Locations of the LVDTs are shown in Figure 3-17.

It should be noted that only the measurements from the instrumentation connected to the abutment part of the specimens were analysed as the readings collected for the deck were considered beyond the scope of the study.

Earth pressure sensors (i.e., total stress cells) were custom made (Figure 3-18). As such, the earth pressure sensors measured 15 mm thick with a diameter of 50 mm and allowed for the measurement of pressures up to 500 kPa in order to compensate for the expected large increase of earth pressure adjacent to the abutment specimens during cyclic loading. The earth pressures cells were attached to the concrete surface using silicone gel to ensure minimal movement of the cells during cyclic loading and sand particle flow.

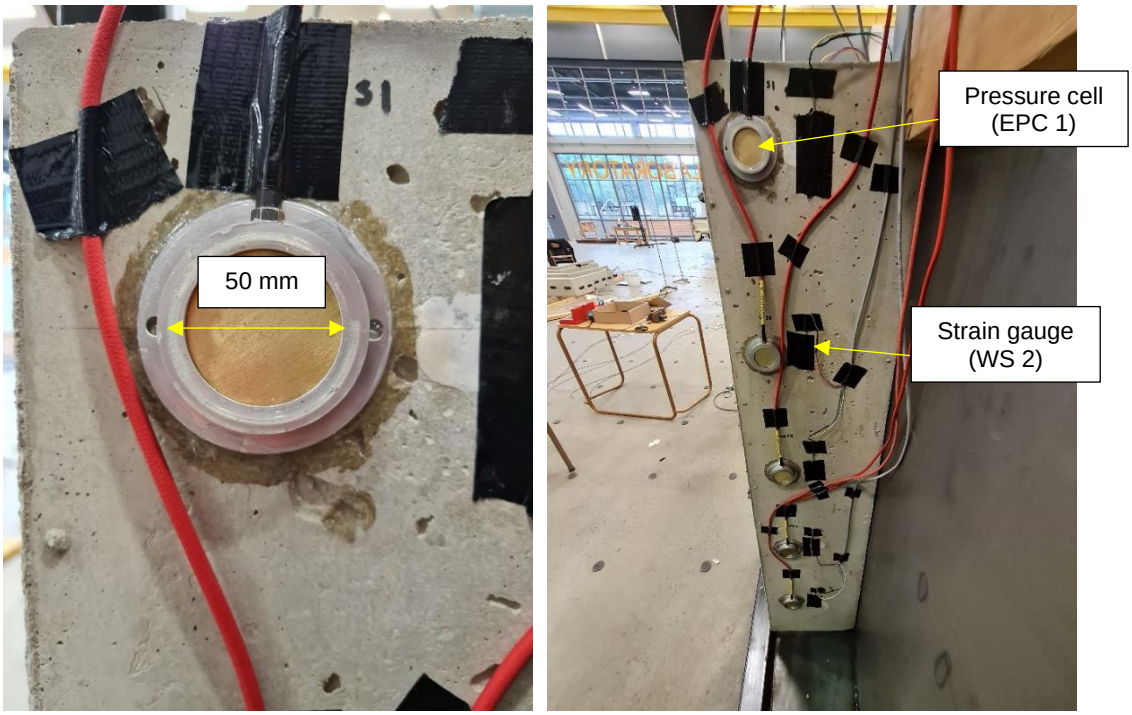

Figure 3-18: Custom built earth pressure transducers and placement on abutment specimens.

It should be noted that the role of stiffness of the stress cells was not assessed and were assumed to be stiff enough for experimental purposes.

The calibration for the cells were performed using a PVC tube where each cell was positioned at the bottom. The tube was then filled with water at different levels to represent different levels of applied pressure. The calibration curves used for each of the sensors is shown in Figure 3-19.

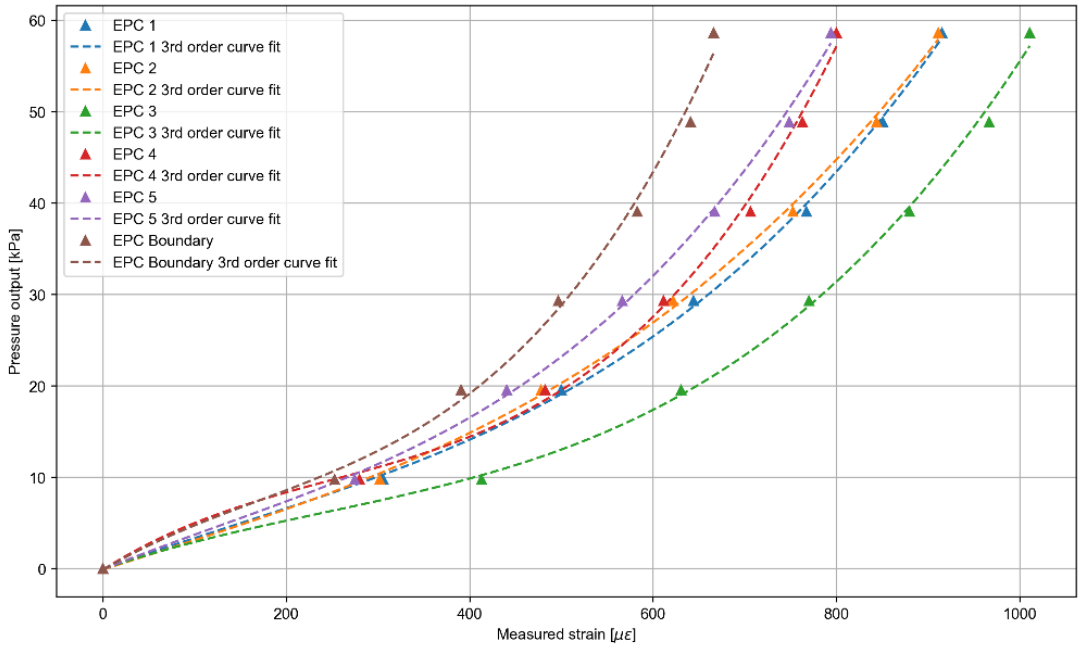

Figure 3-19: Calibration curves for total stress cells.

3.5 Concrete properties

The following section details the results obtained for the concrete according to the relevant SANS and ASTM standards for laboratory testing. Two sets of samples were cast and were both subjected to two different curing methods: the first set of samples were cured dry (representing the properties of the actual abutment specimens), and the second set was cured in 25°C water for 28 days (representing the characteristic properties of the concrete). Each material property therefore has been distinguished as either *characteristic* or *experimental* (i.e., the water cured and dry cured sets respectively) for the purpose of maintaining consistency in the following subsections. The curing of the concrete testing specimens were done in accordance with ASTM C192/C192M–18 and ASTM C511–19.

3.5.1 Concrete mix design/mix composition

For the mix design of the concrete, the goal was to simply achieve a mixture that was close to what can be expected in the field used for real integral bridges. A compressive strength target of roughly 50 MPa was used to determine the constituent mix proportions used for the abutment wall specimens. A CEM 1 52.5R cement was used for the concrete binder.

The mix design required the use of small aggregates in order to be compacted in the thinner sections such as for the 50 mm wall and for the deck portion of all the abutment specimens, and 9.5 mm granite stone and fine granite sand was used for the coarse aggregates and for the fines respectively. The final mix design used to cast the specimens is given in Table 3-3.

Table 3-3: Mix design/Mix composition for concrete abutment specimens.

Material	Mass [kg] per m^3	Density [kg/m^3]	Volume [m^3]
CEM 1 (52.5R)	418.0	3040	0.1375
9.5 mm Granite stone	692.2	2655	0.2607
Granite sand	991.9	2665	0.3722
Water	230.0	1000	0.2300
	Σ= 2332		Σ= 1.000

3.5.2 Compressive strength

The compressive strength testing was done in accordance with SANS 5863:2006. A total of 3 100 mm cubes were cast for the characteristic compressive strength and a total of 15 for the experimental compressive strength. The large number of experimental cubes consist of 3 cubes which were cast for each abutment specimen (5 specimens in total) and were tested just before each corresponding abutment's cyclic loading experiment. The characteristic strength was evaluated after the samples remained submerged in water for 28 days and the experimental strength results were obtained for samples that were exposed to the same dry curing conditions as the specimens. The results for the compressive strengths of the cubes are summarised in Table 3-4.

Table 3-4: Compressive strength values of concrete cubes tested.

		Compressive strengths: [MPa]			
	Abutment specimen	**Cube 1**	**Cube 2**	**Cube 3**	**Average**
Characteristic	-	*46.95*	*47.19*	*51.34*	***48.49***
Experimental	50 mm	57.69	58.27	56.72	57.56
	75 mm	60.01	59.69	54.41	58.04
	100 mm	57.68	59.34	59.06	58.69
	125 mm	61.32	59.79	56.08	59.06
	150 mm	57.73	49.96	56.48	54.72

3.5.3 Concrete density

The concrete cubes were weighed dry and submerged in water to determine the density values in accordance with ASTM C642-21. Table 3-5 details the results for each abutment wall specimen.

Table 3-5: Concrete density of cubes tested.

		Density: [kg/m3]			
	Abutment specimen	**Cube 1**	**Cube 2**	**Cube 3**	**Average**
Characteristic	-	*2285*	*2281*	*2286*	***2284***
Experimental	50 mm	2229	2229	2222	2227
	75 mm	2222	2214	2214	2217
	100 mm	2215	2226	2221	2221
	125 mm	2233	2218	2224	2225
	150 mm	2218	2218	2221	2219

3.5.4 Static Modulus of Elasticity

The static modulus of elasticity for the dry cured and water cured sets were determined in accordance with ASTM C469/C469M-14e1. For the dry cured set of concrete, 2 cylinders were cast for each abutment specimen, and 2 cylinders were cast for the wet cured set. Table 3-6 summarises the characteristic and experimental results for the concrete specimen.

Table 3-6: Static Modulus of Elasticity of concrete cylinders tested.

		Static Modulus of Elasticity: [GPa]		
	Abutment specimen	**Cylinder 1**	**Cylinder 2**	**Average**
Characteristic	-	*24.3*	*24.7*	***24.5***
Experimental	50 mm	24.9	23.5	24.2
	75 mm	24.4	23.3	23.9
	100 mm	24.5	23.5	24.0
	125 mm	25.4	23.2	24.3
	150 mm	23.1	23.9	23.5

From the results it can be observed that there is little to no variation, therefore it can be confirmed that the dimension change/relative stiffness of the abutment specimens were the only variable and that no difference in material properties existed between specimens.

3.5.5 Indirect tensile strength

The tensile splitting strength of the concrete cast was tested in accordance with SANS 6253:2006. The final results are summarised in Table 3-7.

Table 3-7: Tensile splitting strength of concrete cylinders tested.

		Splitting tensile strength: [MPa]				
		Cylinder 1		Cylinder 2		Average
	Abutment specimen	Top	Bottom	Top	Bottom	Top & Bottom
Characteristic	-	*3.501*	*3.755*	*3.382*	*3.537*	***3.65***
Experimental	50 mm	3.669	3.991	3.553	3.656	3.72
	75 mm	3.817	3.882	4.094	4.409	4.05
	100 mm	3.450	3.811	3.508	3.952	3.68
	125 mm	3.624	4.042	3.109	3.611	3.60
	150 mm	3.920	4.062	4.042	4.004	4.01

3.5.6 Tensile cracking strain of concrete

Based on the values of indirect tensile strength and static modulus of elasticity of the tested samples, the *tensile cracking strain* could be estimated using the following relationship:

$$\sigma_t = \epsilon_t \times E$$

$$\therefore \epsilon = \frac{\sigma_t}{E} \qquad \text{Equation 3-2}$$

Using Equation 3-2 above, the characteristic value for the tensile cracking strain for the concrete used for the abutment specimens was determined and is given in Table 3-8.

Table 3-8: Tensile cracking strains for the specimens.

	Abutment specimen	σ_t [MPa]	E [GPa]	ϵ [$\mu\epsilon$]
Characteristic	-	3.65	24.5	***134***
Experimental	50 mm	3.72	24.2	139
	75 mm	4.05	23.9	152
	100 mm	3.68	24	138
	125 mm	3.6	24.3	133
	150 mm	4.01	23.5	154

The characteristic value for the tensile cracking strain for the concrete was determined to be approximately 134 $\mu\epsilon$ (taking into account that tensile strength is 0.9 times the splitting tensile strength in accordance with EN1992-1-1:2004).

3.6 Soil properties

3.6.1 Particle size distribution and soil type

The particle size distribution of the silica sand that was used to fill the steel frame strong box was measured using a Malvern 3000 as shown in Figure 3-20.

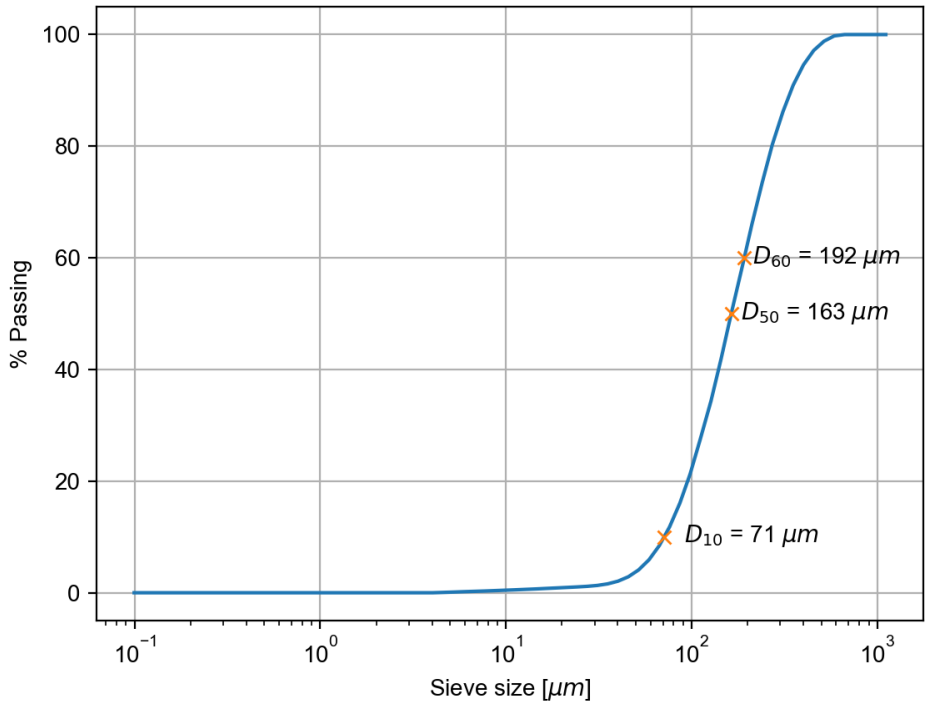

Figure 3-20: Particle size distribution of silica sand used for testing.

From Figure 3-20, the *average/mean particle size* D_{50} was determined as 163 μm. Values for D_{10} and D_{60} were found to be 71 μm and 192 μm respectively. The corresponding *coefficient of uniformity* C_U based on the values for D_{10} and D_{60} is given as 2.704 ($C_U < 4$, uniform grading). The soil was classified as a *fine sand* according to Table 3-9.

Table 3-9: Classification of soils according to particle size (Knappet and Craig, 2012).

Representative Particle dimension [mm]									
Clay	Silt			Sand			Gravel		
	Fine	Medium	Coarse	Fine	Medium	Coarse	Fine	Medium	Coarse
<0.002	0.002 - 0.006	0.006 - 0.02	0.02 - 0.06	0.06 - 0.2	0.2 - 0.6	0.6 - 2	2 - 6	6 - 20	20 - 60

3.6.2 Specific gravity/Relative density

The speficific gravity (also known as the relative density) of the silica sand was determined using an AccuPyc II 1340 Pycnometer. Three tests were performed on a sample to determine the average G_s value, which was found to be 2.667 g/cm^3 for the sand.

3.6.3 Oedometer testing (E-value)

Due to the nonlinear nature of soil in general, the soil stiffness (Young's modulus) was estimated from a modified version of the one-dimensional oedometer test as specified in ASTM Standard D4546-14e1. The sand was placed into the confining ring and cylinder of the oedometer using the same pluviation technique used for placing sand in the steel frame strong box. The relative density was calculated as 0.7128 (compared to 0.5470 for the sand in the steel box) as per Table 3-11. The prepared sand specimen was placed into the oedometer apparatus and a seating pressure of 1 kPa was applied. The oedometer setup utilised a 20 mm dial gauge (with a resolution of 0.02 mm) to measure the displacement of the sample. The sand was placed into the oedometer completely dry as the intention of the test was to only determine a characteristic value for the Young's modulus of the sand in the steel frame strong box. No swelling nor collapse properties of the sand were determined as this was deemed outside of the scope of the current investigation.

Tests were performed on 2 representative samples of the silica sand. The samples were each loaded in equal increments of 760.81 g (which are amplified by a factor of 10 by the moment arm of the oedometer apparatus corresponding to a true incremental loading of 16.91 kPa on the sample), of which each increment represented 25% of the expected load at the bottom of the steel frame strong box. This value was determined from *Rankine's theory of passive earth pressure* at the base of the abutment wall where the pressure was theoretically expected to be at its greatest (K = 3 for a friction angle of approximately 30° for sands). The expected total horizontal passive pressure at the bottom was determined to be 67.64 kPa based on the assumption of a friction angle of 30° and a soil unit weight of 1533 kg/m^3.

The samples were loaded to 100% of the expected theoretical pressure, where after the samples were unloaded back to 0% (i.e., the 1 kPa initial pressure). The samples were then loaded to 200% and again unloaded to 0%. The second test was identical to the first but differed slightly as the sample was first loaded to 50% of the expected theoretical load and then also loaded to 300% again after the 200% loading cycle in order to assess the variability in the stiffness of the sand in response to different pressure ranges as well as to verify the repeatability and degree of consistency of the testing that was conducted. This pressure range was most likely an overestimate of the true pressures that can exist behind the abutment wall and was thus assumed to cover the entire range of possible pressures behind the abutment.

The axial (vertical) strain was then calculated from the measured displacement (based on the zero reading of the sample's initial height before testing commenced). The stress-strain curves of the oedometer tests conducted are given in Figure 3-21.

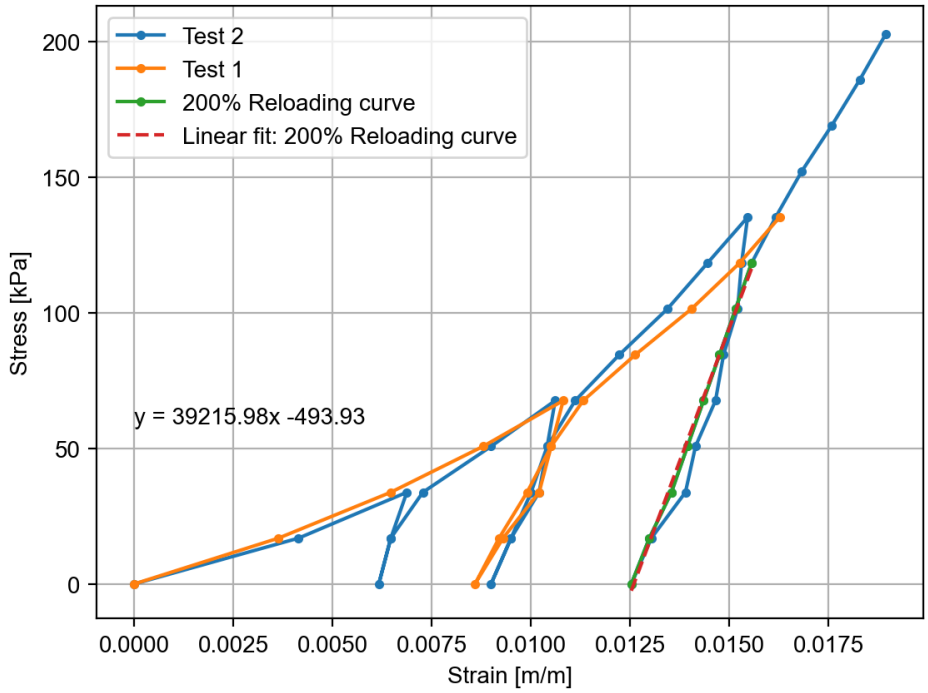

Figure 3-21: Oedometer results for silica sand.

From inspection of Figure 3-21, the repeatability of the test was verified and the data of the second test was used to determine the characteristic stiffness value for the silica sand.

A simplified approach was used to determine the characteristic stiffness value of the sand based on the stress-strain curves by calculation of an approximate *constraint modulus* E_0 for the silica sand through the process of curve fitting a linear function through the data points of the 300% reloading curve (up until 200% of the loading was achieved) and obtaining the gradient of the trendline. The constraint modulus for the silica sand was determined as 39.2 MPa.

The characteristic stiffness (Young's modulus) E_s of the silica sand was then calculated using Equation 3-3:

$$E_s = \frac{E_0 \cdot (1-v)}{(1+v)(1-2v)} \qquad \text{Equation 3-3}$$

Where:

v = Poisson's ratio of the silica sand

A value of 0.3 was assumed for the Poisson's ratio for the silica sand for the calculation of the Young's modulus (E_s) as per Equation 3-3. The characteristic stiffness (Young's modulus) was calculated as 52.8 MPa for the sand.

3.6.4 Angle of internal friction

Triaxial testing was conducted to calculate the *angle of internal friction* of the sand ϕ'. Consolidated undrained triaxial testing was conducted in accordance with ASTM D4767-11. A total of 3 triaxial tests were conducted on 100 kPa, 300 kPa, and 500 kPa confining pressures. The data from the 500 kPa test was unfortunately not useable to determine the friction angle and as such historical data (Archer, 2014) was used to supplement in calculating the strength characteristic of the sand. The shear strength parameters for the silica sand were determined from the relationship between the *deviatoric stress invariant* t' and the *mean stress invariant* s' for the experimental results and have been overlain on the historical data, shown in Figure 3-22.

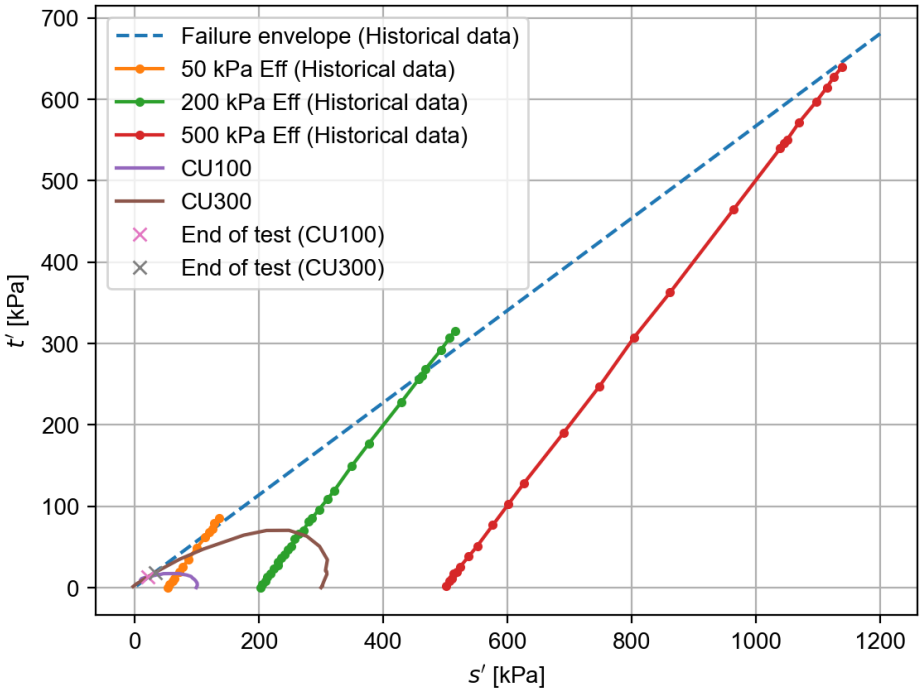

Figure 3-22: Stress path results for triaxial tests and historical data for silica sand (Archer, 2014).

Based on the slope of the failure envelope, the angle of internal friction for the silica sand was determined to be approximately 34° with cohesion of $c' = 0$ kPa.

3.6.5 Density and void ratio

The density (or rather *relative density*) of the sand was determined as specified by the ASTM whereby the current state of the silica sand's compactness was expressed in terms of the maximum and minimum possible densities in which the sand can be placed. The relative density can be expressed as the ratio of the difference between the maximum and current compaction states to the difference between the maximum and minimum compaction states. Mathematically, the ratio can be written as:

$$D_r = \frac{e_{max} - e}{e_{max} - e_{min}}$$ Equation 3-4

Where:

D_r = relative density of a soil

e = void ratio of the current state of compactness (density) of the soil

The maximum and minimum void ratios required by Equation 3-4 were determined using Equation 3-5 and Equation 3-6 using the respective maximum and minimum *dry density values* of the sand.

$$e_{max} = \left(\frac{\rho_{water} \cdot G_s}{\rho_{min}}\right) - 1$$ Equation 3-5

$$e_{min} = \left(\frac{\rho_{water} \cdot G_s}{\rho_{max}}\right) - 1$$ Equation 3-6

Where:

ρ_{water} = density of water at approximately 20 C (≈997 kg/m^3)

The dry densities were determined in accordance with ASTM Standard D4253-16 and D4254-16. The results for the dry density tests are summarised in Table 3-10.

Table 3-10: Maximum, minimum, and pluviation densities for silica sand.

	Density: [kg/m^3]			
	Sample 1	**Sample 2**	**Sample 3**	**Average**
Maximum	1616	1596	1583	1598
Minimum	1462	1456	1463	1460
Pluviation	1532	1533	-	1533

From the density results above, ρ_{min}, ρ_{max}, and $\rho_{pluviation}$ were determined to be 1459, 1598, and 1532 kg/m^3 respectively. The corresponding void ratios and relative densities are summarised in Table 3-11.

Table 3-11: Void ratios and relative densities determined for silica sand.

	Void ratio e:	**Relative density D_r:**
Maximum	0.8213	0.000
Minimum	0.6635	1.000
Pluviation (steel box)	0.7350	0.5470
Oedometer testing	0.7089	0.7128

Based on the void ratios given in Table 3-11, the relative density of the silica sand in the steel box for each experimental setup was approximated as 0.5470.

3.6.6 GeoPIV-RG parameters

The distance of the camera from the glass panel door was the primary limitation of the PIV analyses conducted for the dissertation as the results computed by GeoPIV-RG are heavily dependent on the quality (or rather resolution) of the images taken of the sand. Table 3-12 details the parameters and corresponding values entered for all PIV analyses conducted.

Table 3-12: GeoPIV-RG parameters used for all PIV analyses.

GeoPIV-RG parameter:	Value used in all analyses:
Patch size	200 pixels
Patch spacing	100 pixels
Maximum iterations	50
Cut-off tolerance	$1x10^{-5}$
$CC_{ZNCC\ seed\ tolerance}$	-0.1 (0.75 recommended)
$CC_{ZNCC\ min\ tolerance}$	-0.1

In order to guarantee successful computation of all PIV analyses, the tolerance parameters were lowered significantly from the recommended values. A patch size of 200 pixels spaced at 100-pixel intervals was chosen in order to compensate for the large distance between the camera and the laminated glass door of the steel frame strong box whilst still providing enough detail in terms of the calculated displacements of the sand particles.

All results computed by the PIV software were therefore only used for qualitative evaluation where emphasis was placed on overall sand mass behaviour and flow patterns. The total number of photos used for each test (all of which were 3456 x 5184 pixels in resolution) and stray subsets removed per analysis are shown in Table 3-13.

Table 3-13: Number of photos used for PIV analyses and stray subsets removed per analysis.

	50 mm specimen	75 mm specimen	100 mm specimen	125 mm specimen
Stray subsets	58	27	49	46
Number of photos used for analysis	137	123	136	139

On average, roughly 1800 subsets were generated per analysis and based on the data shown in Table 3-13, an approximate loss of 3% was present for any given PIV analysis.

4 Preliminary test results

4.1 Introduction

The following chapter is dedicated to the measured results of the specimen with an abutment thickness of 150 mm (i.e., the most rigid specimen) which was loaded cyclically at 1g scale to a displacement magnitude of 1 mm, 2 mm, 3 mm, and 4 mm (measured horizontally at the top of the abutment wall) for a total of 20 cycles at each displacement level. The displacement magnitude and number of cycles applied to the final specimens (i.e., having thicknesses of 50 mm, 75 mm, 100 mm, and 125 mm) was determined based on the measured strains of the preliminary test.

This report follows specific sign conventions for the deck and abutment specimens regarding the active and passive movement directions, bending moments, and deflections as illustrated in Figure 4-1. It should be noted that the shapes of the displacement, bending moment, and deflection diagrams shown in Figure 4-1 are for illustrative purposes only to clarify the sign convention used and is not intended to represent the measured results.

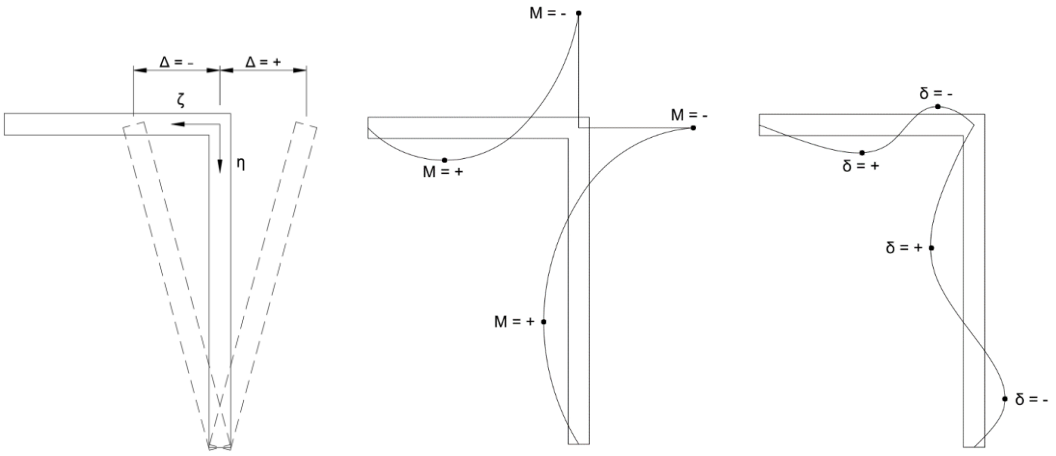

Figure 4-1: Sign conventions used for (a) displacement of the abutment wall, (b) bending moments, and (c) deflections.

All figures reflect this sign convention, with strain data being the only exception where tensile strain is represented by a positive value and compressive strain is represented by a negative value. For the deck in particular, data has been visualised as represented graphically in Figure 4-1 (a) where $\zeta = 0$ and $\eta = 0$ represent the position of the abutment-deck joint. For the purposes of this dissertation ζ is referred to as the normalised length of the deck and η is referred to as the normalised depth of the retained sand.

For a single applied cycle, the neutral position represented the starting point (i.e., $\Delta = 0$ as shown in Figure 4-1 (a)) where the abutment was then first displaced towards the retained sand. This position is referred to as the passive position having a cycle number of +0.25 and was then moved away from the fill, passing the neutral position (i.e., cycle +0.5) and moving the same amplitude away which represented the active position having a cycle number of

+0.75. The abutment would then be displaced towards the neutral position again which would represent the completion of a single cycle. The cycle number notation used for any given cycle is detailed schematically in Figure 4-2.

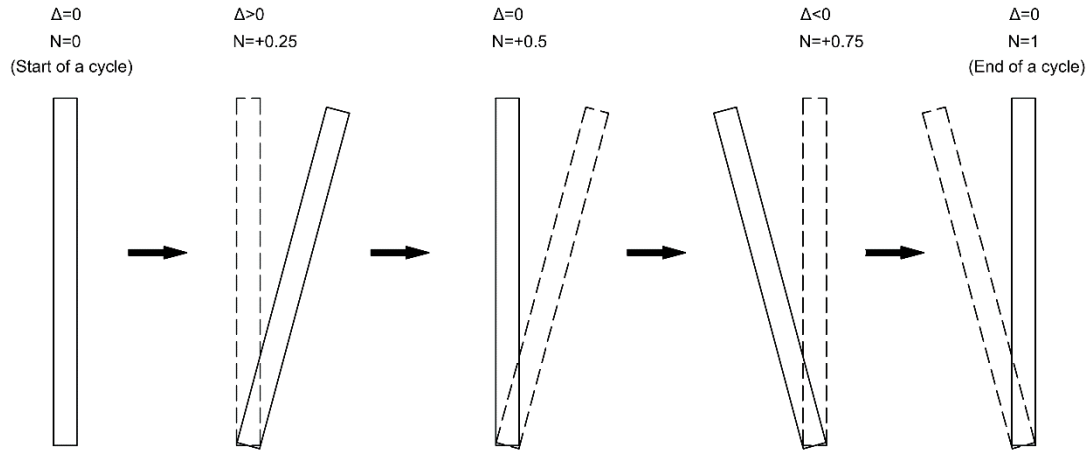

Figure 4-2: Schematic representation of the movement of the abutment for any given cycle.

In order to determine the magnitude for the displacement of the abutment wall which would allow for the stress-strain behaviour of the concrete to remain in the elastic response region and also to ensure that ratcheting (strain hardening) could take place (Table 2-1), the most rigid abutment-deck specimen was first tested to evaluate what displacement would be most suitable for all the specimens. Displacement amplitudes of 1 mm, 2 mm, 3 mm, and 4 mm were cycled successively in this order (Figure 4-3), where each level of displacement was loaded with 20 cycles to assess the magnitude of forces and earth pressures that would develop as well as to check if the abutment and deck parts exhibited any significant strains that could possibly cause cracking and hence not adhere to elastic material behaviour. The cycles were applied at a rate of 0.12 mm/s (7.4 mm/min) by the actuator and was assumed adequate for experimental testing. It is acknowledged that the chosen rate of 0.12 mm/s is not representative of the rate of thermal expansion and contraction and the effects of loading rate on the specimens were deemed beyond the scope of the study.

It should be noted that for this preliminary test, no deflection data was captured using the LVDT setup.

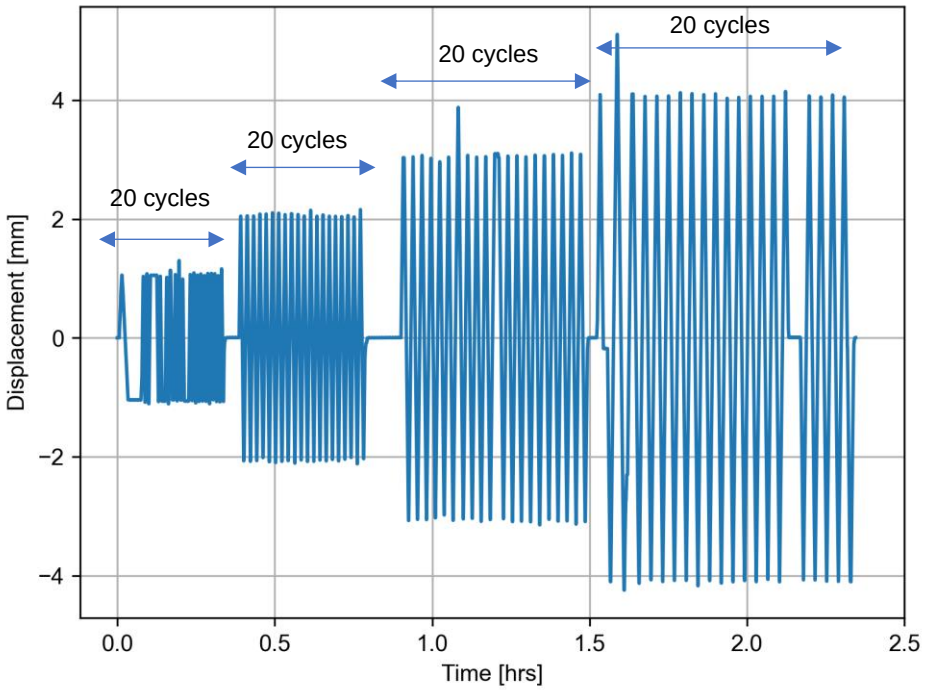

Figure 4-3: Initial pairs of 20 cycle loadings for 150 mm preliminary specimen.

It should be noted that for all measurements (i.e., the measured earth pressures, strains and displacements) the data was zeroed before the pluviation of the sand into the steel frame strong box. This zeroing strategy was intentional as the measured results therefore also show the stresses, strains and deflections of the specimens immediately before the commencement of the cyclic loading.

4.2 Measured earth pressures

The earth pressures for the 150 mm specimen are represented graphically in Figure 4-4. Based on the results for the different levels of displacement magnitude, it becomes evident that the greater amplitudes (3 mm and 4 mm) demonstrated greater increases in earth pressure for successive cycles than for the 1 mm and 2 mm displacement amplitudes.

For the 3 mm and 4 mm displacement amplitudes, applying only 20 cycles resulted in an increase in the maximum pressure (as measured by EPC 2) by a factor of nearly 3 for the 3 mm amplitude and by a factor of roughly 6 for the 4 mm amplitude compared to the 2 mm amplitude (Figure 4-4). It should be noted that during the testing procedure for the 150 mm specimen, a sand leak developed during cycling which was more prominent during the 4 mm cycles. This caused rapid drops in the measured earth pressures as can be seen starting at the 1.6-hour mark, especially for earth pressures measured at EPCs 1 and 5 (the top and bottom cells respectively). In an effort to maintain a consistent vertical total earth pressure, sand was continuously poured back into the steel frame strong box during the last 20 cycles, however this was not sufficient to maintain the same reliable trend in lateral/horizontal pressure increase as for the 1 mm, 2 mm, and 3 mm amplitude cycles.

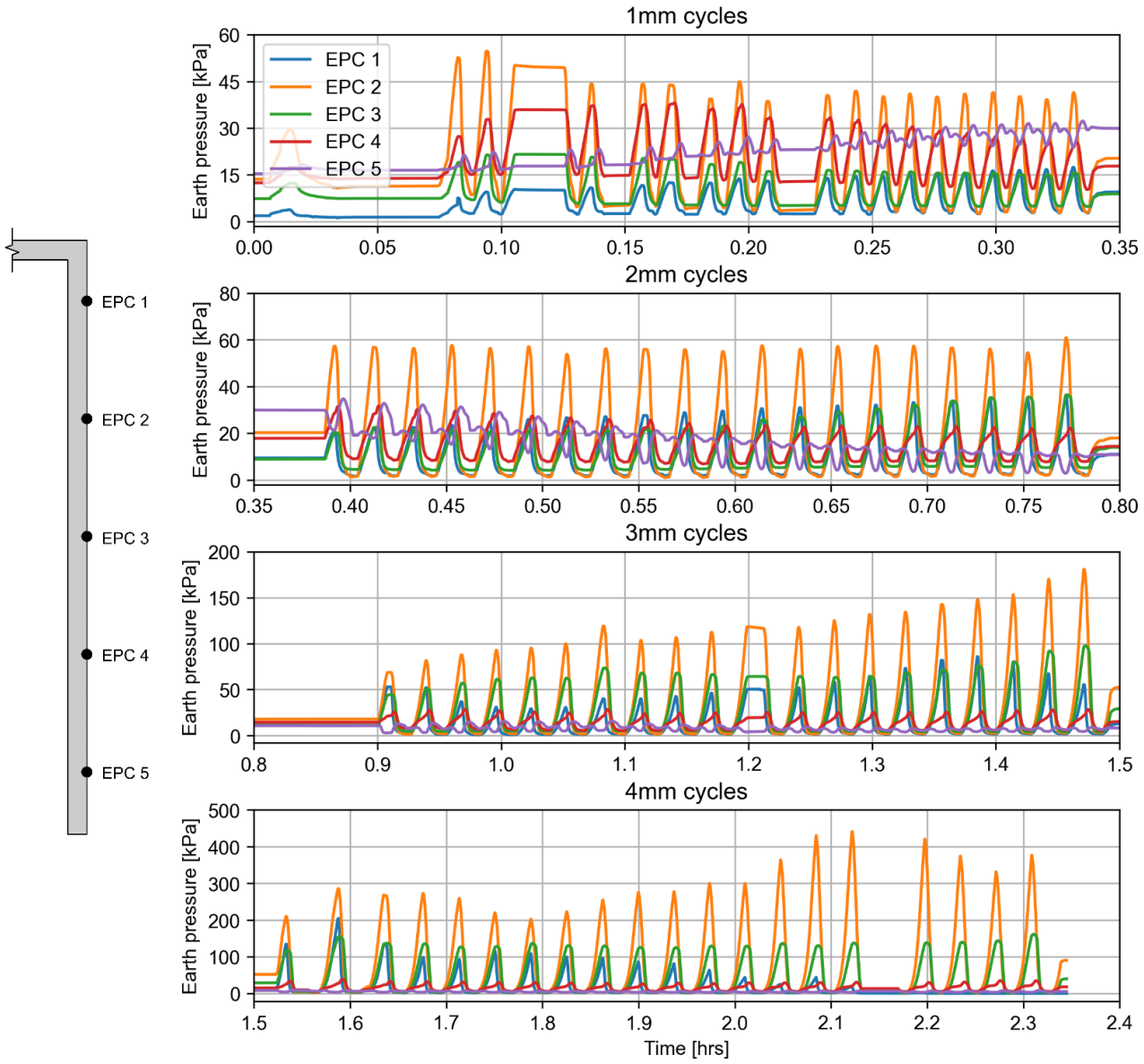

Figure 4-4: Earth pressures recorded for each 20-cycle loading pair for 150 mm specimen.

Readings for the boundary earth pressure cell (refer to Figure 4-5) revealed that 1 mm displacements (i.e., both expansion and contraction) were enough for ratcheting to occur in the sand, albeit relatively small compared to the larger displacement amplitudes. The 1 mm displacement magnitude corresponds to a Δ/H value equal to 0.000667, which is 15 times less than the minimum ratio required to reach passive pressures as determined by Barker *et al.* (1991) for a dense sand.

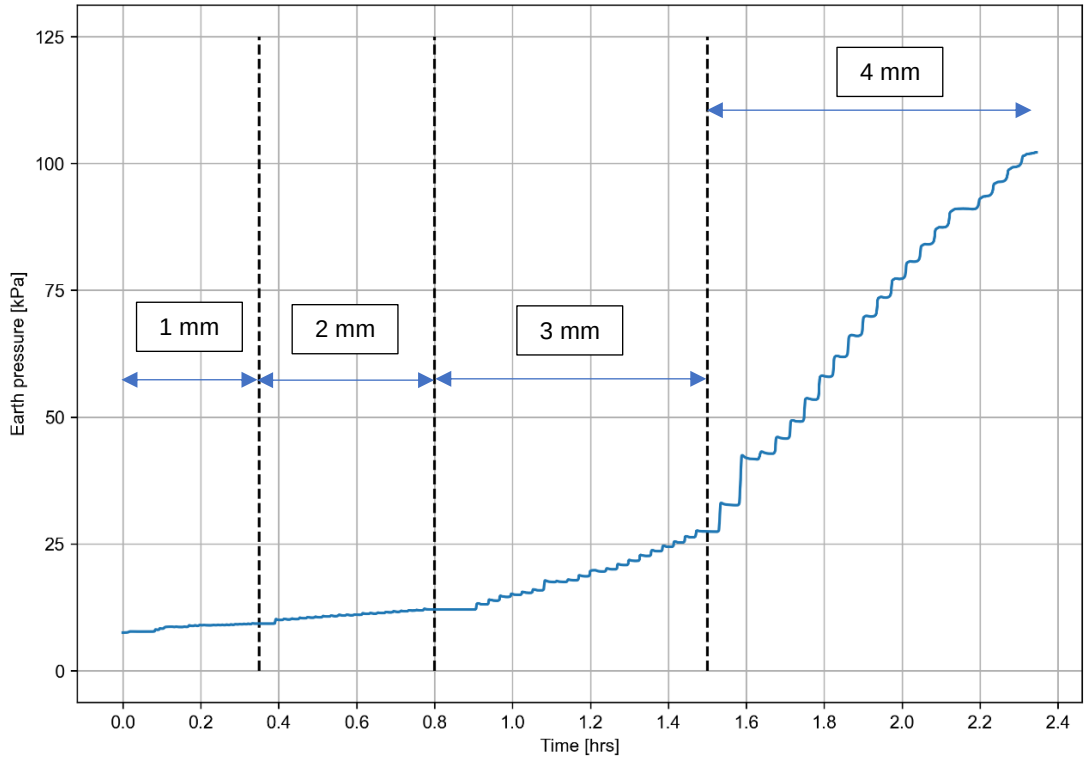

Figure 4-5: Boundary earth pressure cell readings for each 20-cycle loading pair for 150 mm specimen.

Based on the *stepped* appearance of the data shown in Figure 4-5 it is evident that active movements cause little change in the overall pressure measured at the boundary earth pressure cellFigure 4-5. The whole sand mass is densified for each passive movement applied by the concrete abutment specimen with no apparent asymptotic pressure after the applied 80 cycles.

It should be noted that the high horizontal earth pressures measured at EPC2 close to the top of the abutment wall may possibly indicate unwanted boundary effects. The influence of the boundary effects on the measured results was assumed negligible and the assessment of adequate box width was deemed beyond the scope of the study.

4.3 Measured abutment strains

Strains measured in the abutment for the 150 mm specimen at the external and internal sides (refer to Figure 3-17) are shown in Figure 4-6 and Figure 4-7 respectively. The strains in the abutment walls demonstrated the same trends at all amplitudes compared to the deck part, with the exception of the 4 mm amplitude. All strains measured for the abutments remained at a strain value below the 134 $\mu\epsilon$ mark which indicates that the deck part of the structure is the critical member. Strains showed increases in magnitude for increasing number of cycles for all amplitudes. The degree/rate of increase achieved per cycle was directly proportional to the applied amplitude (which is in agreement with the findings of England and Tsang (2000; 2001) and Ng *et al.* (1998a; 1998b)).

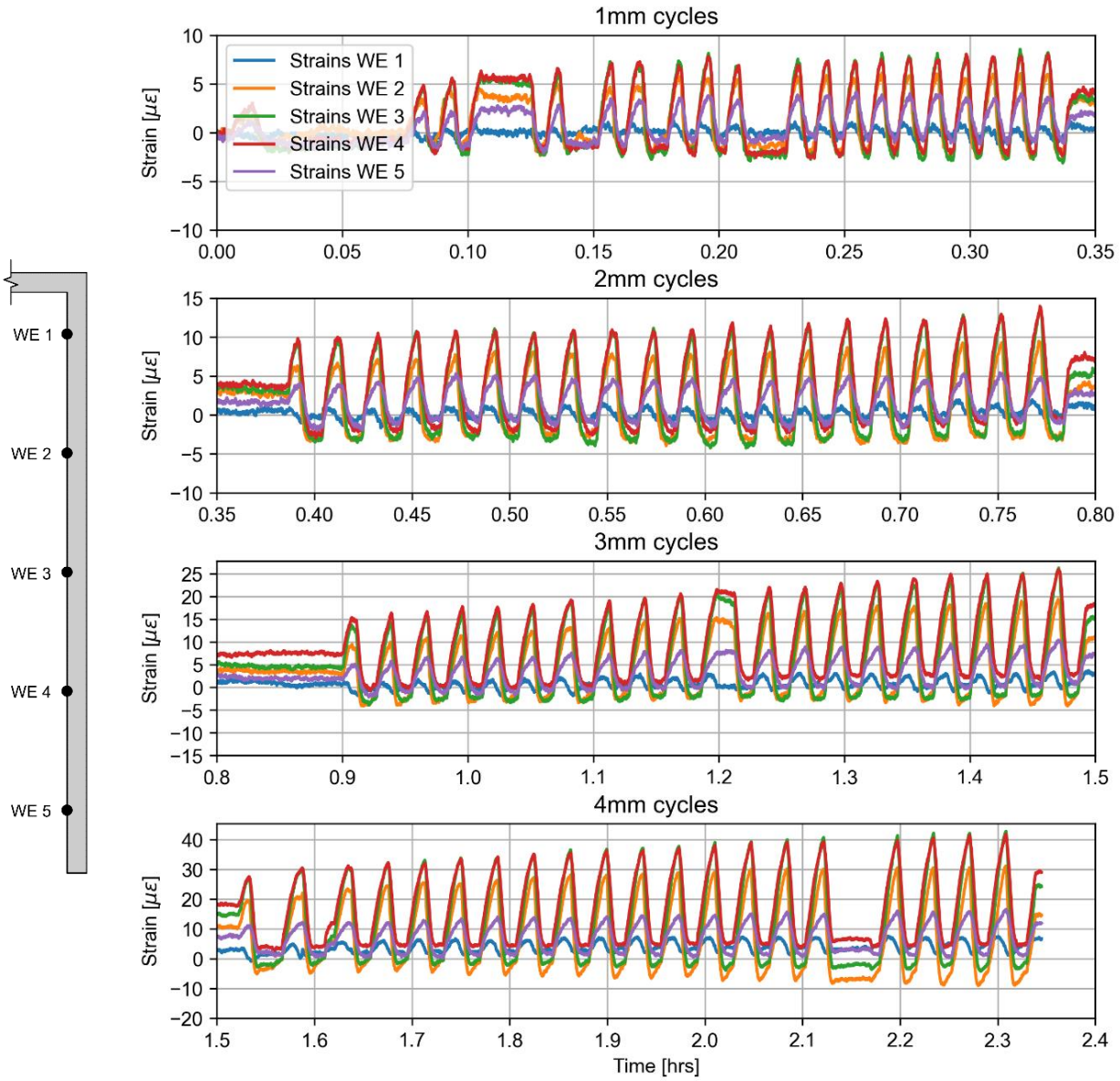

Figure 4-6: External abutment strains caused by 20-cycles loading pairs for 150 mm specimen.

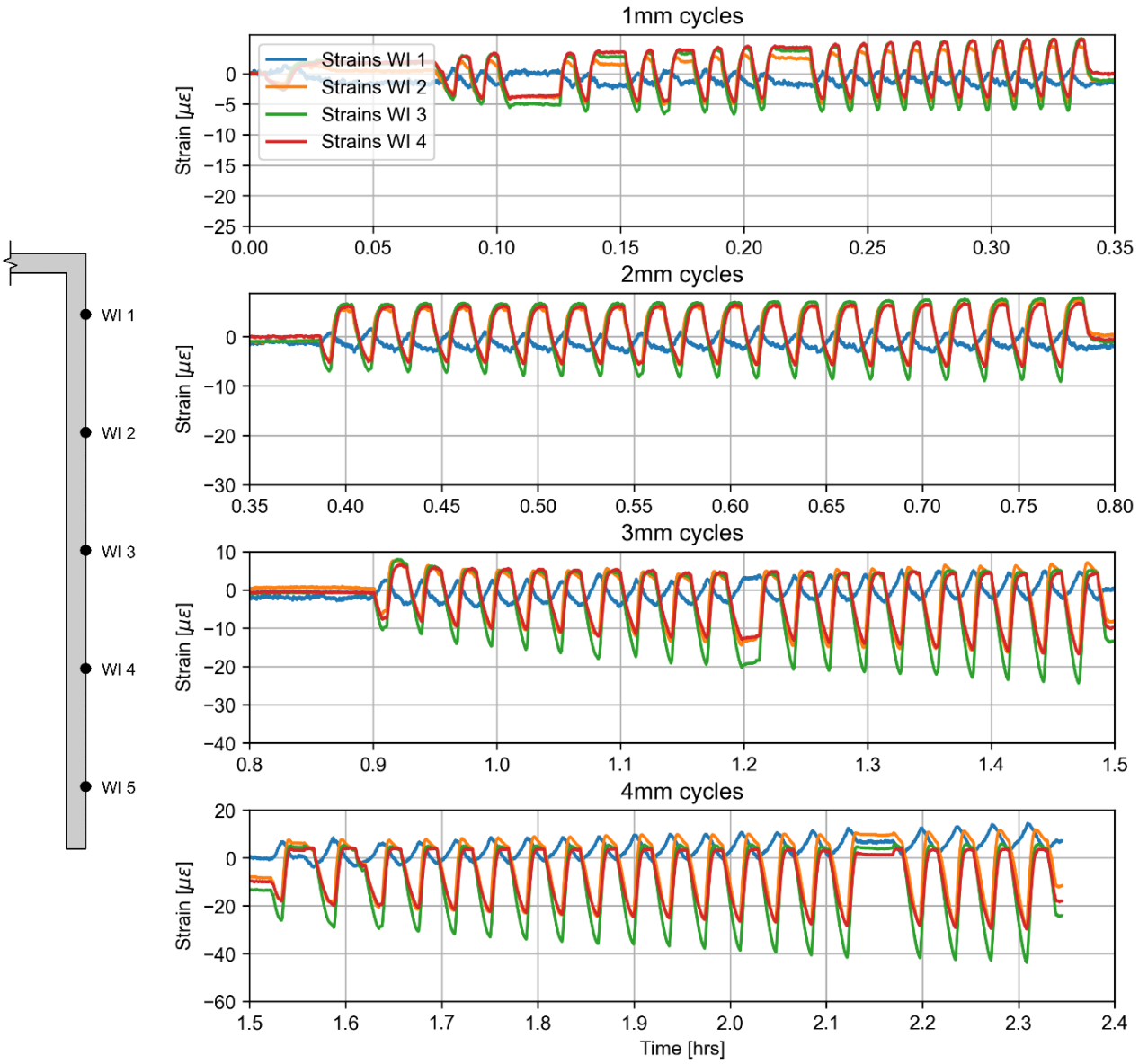

Figure 4-7: Internal abutment strains caused by 20-cycles loading pairs for 150 mm specimen.

4.4 Measured deck strains

The deck strains for the top and bottom surfaces are shown in Figure 4-8 and Figure 4-9 respectively. The strains remained small for the 1 mm and 2 mm displacement amplitudes whereas for the 3 mm amplitude, the strains exceeded the 134 $\mu\epsilon$ value after the first 5 cycles which is sufficient for the development of fine cracks in the concrete. The 4 mm displacement magnitude resulted in a large crack at the position of the first and second strain gauges (DT 1 and DT 2 respectively, refer to Figure 3-17) immediately after the first cycle at this amplitude.

Cracking occurred in the 150 mm specimen and the results were therefore only used to determine the adequate amplitude for all further tests conducted on the rest of the specimens.

Strains at the lower amplitudes were consistent with each other and all amplitudes showed an increase in strain (both for the top and bottom surfaces) for increasing cycles, indicating that a greater axial force was developing over time in the deck portion of the 150 mm specimen, hence indicating that ratcheting occurred in the retained sand.

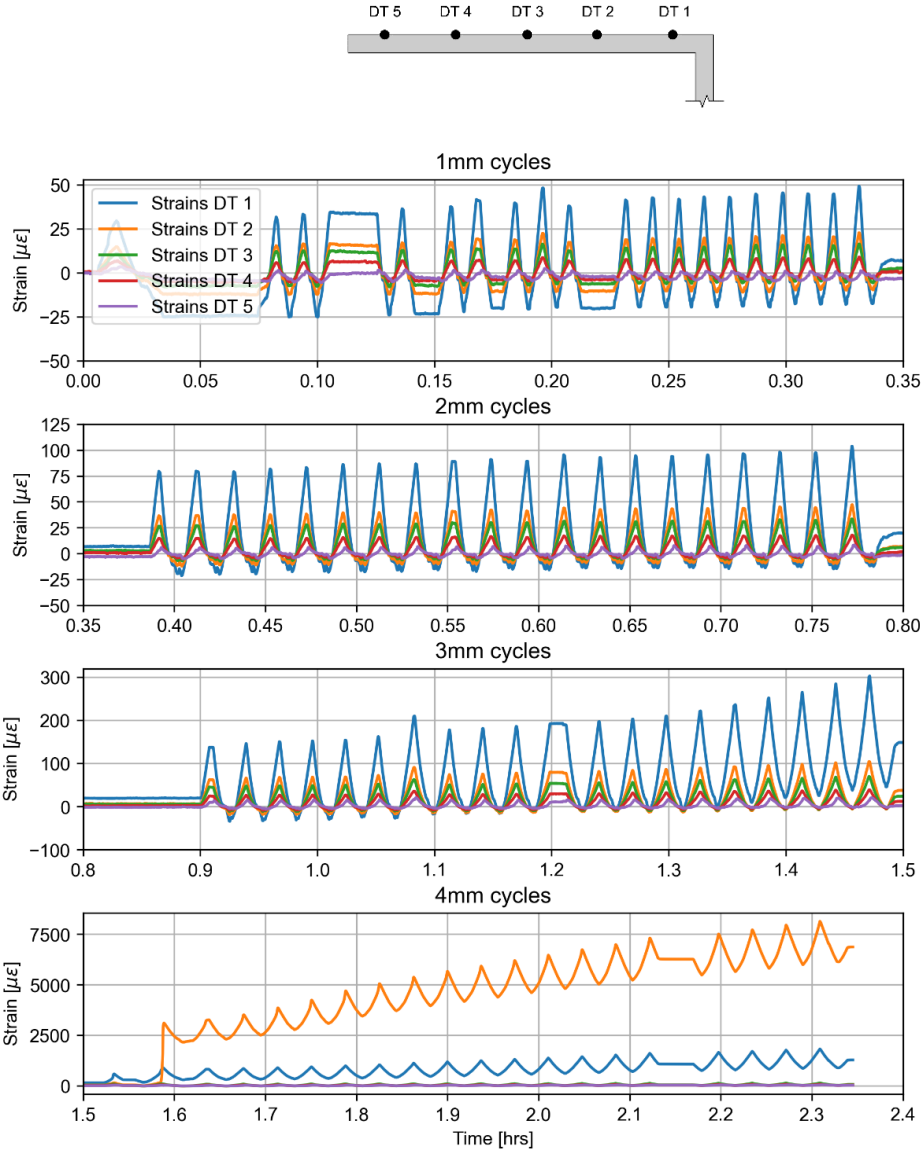

Figure 4-8: Top deck strains caused by 20-cycle loading pairs for 150 mm specimen.

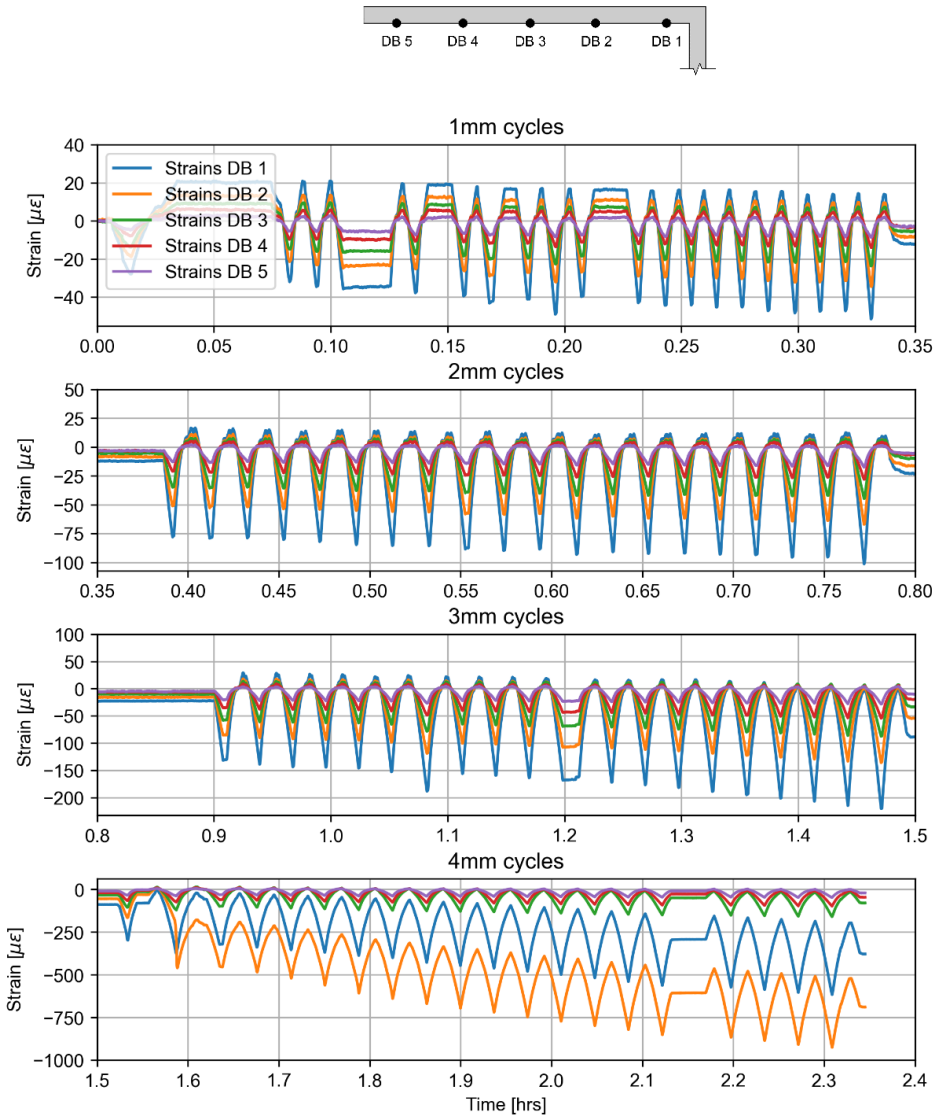

Figure 4-9: Bottom deck strains caused by 20-cycle loading pairs for 150 mm specimen.

4.5 Displacement amplitude for testing of other specimens

From the strain data gathered for the 150 mm specimen, it can be concluded that the deck portion of the structure is the critical member since it will fail first (i.e., a plastic hinge will form in the deck) near the joint connection to the abutment wall if a displacement amplitude of 4 mm or higher is applied to the structure.

The displacement amplitude for all successive testing was chosen to be 2 mm. The 1 mm displacements were considered too small to be comparable to a real integral bridge's thermal expansion and contraction as well as the Δ/H value. The 3 mm amplitude was not used due to the tensile strain in the deck reaching the cracking strain of 134 $\mu\epsilon$ within 20 displacement cycles. As part of the design of the experiment, it was critical to ensure that the material properties of the abutment wall and deck portions behaved elastically, which based on the above strain results indicated that 2 mm would be the most suitable amplitude. It is acknowledged that the choice of 2 mm displacement amplitudes is a significant limitation on

the study since real integral bridges experience expansion and contraction displacements at an order of magnitude larger than 2 mm but was deemed beyond the scope of the study.

4.6 Number of cycles used for testing of other specimens

As the effect of seasonal temperature cycles was the primary focus of the experiments, a total of 120 cycles was performed on each specimen, representing an equivalent service life of 120 years for a real integral abutment bridge as recommended by the British Standards. Other works such as Sandberg *et al.* (2020), Springman *et al.* (1997), Ng *et al.* (1998a; 1998b), England and Tsang (2000; 2001), and Caristo *et al.* (2018) have also numerically and/or experimentally analysed integral bridge structures using 120 years as the design service life period. Other codes such as the Eurocode require a service life of 100 years, hence the chosen 120 seasonal cycles were regarded as the most conservative case for evaluation of the ratcheting effect over the long term.

4.7 Summary

The results from the preliminary test are summarised as follows:

- Preliminary testing of the 150 mm specimen (most rigid) indicated that a displacement amplitude of merely 1 mm ($\Delta/H = 0.000667$) was sufficient to induce the strain hardening/ratcheting effect in the retained silica sand.
- Amplitudes larger than 2 mm would either eventually lead to severe strains after enough cycles have been applied or would immediately result in significant strains causing crack formations in the deck part of the specimen.
- The deck part of the specimen governs the overall capacity of the model structure (critical member). It was also found that the rate of increase in earth pressure achieved per cycle is proportional to the applied displacement amplitude.
- A final displacement amplitude of 2 mm was chosen for all successive experimental testing based on the preliminary test results.
- A total of 120 seasonal cycles was chosen for all successive tests (representing a 120-year design life for an integral bridge) as recommended by the British Standards which is conservative compared to the 100-year design life recommended by the Eurocodes.

5 Experimental results

5.1 Introduction

The following chapter is dedicated to the analysis and discussion of the measured results for the 4 abutment specimens which ranged in thickness from 50 mm to 125 mm.

5.2 Abutment wall deflection

Two distinct modes of deflection have been analysed. Firstly the actual true deflection measured by the LVDTs was investigated (without any offsetting or modification of the raw data) and secondly the curvature of each wall was isolated. Each mode is detailed in the following sections specifically for the abutment wall of each specimen:

The deflection data measured by the abutment wall LVDTs are plotted as a function of the normalised depth of the sand (denoted by η) and is shown in Figure 5-1, Figure 5-2, Figure 5-3, and Figure 5-4.

Each cycle is denoted by its number where the first movement towards the retained sand (referred to as the passive movement) is denoted by cycle +0.25 and therefore the first movement away from the fill is denoted by cycle +0.75 (referred to as the active movement). The neutral position represents the point where a full cycle has been completed and is thus the position where each specimen returns to after completion of the 120 cycles.

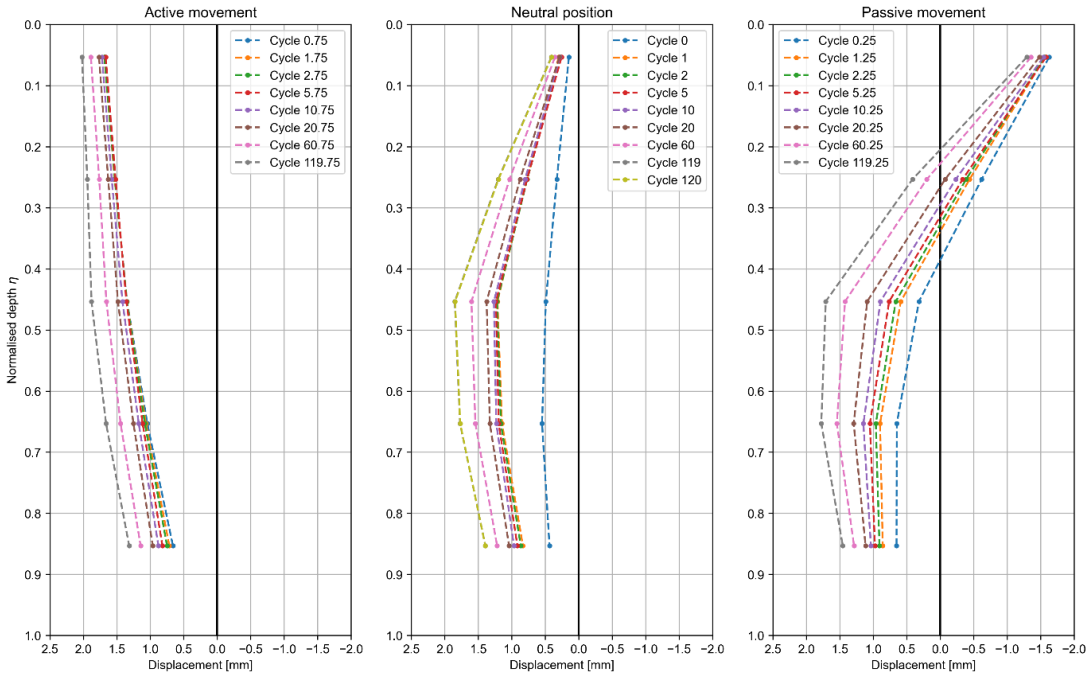

Figure 5-1: Measured abutment deflection for the 50 mm specimen.

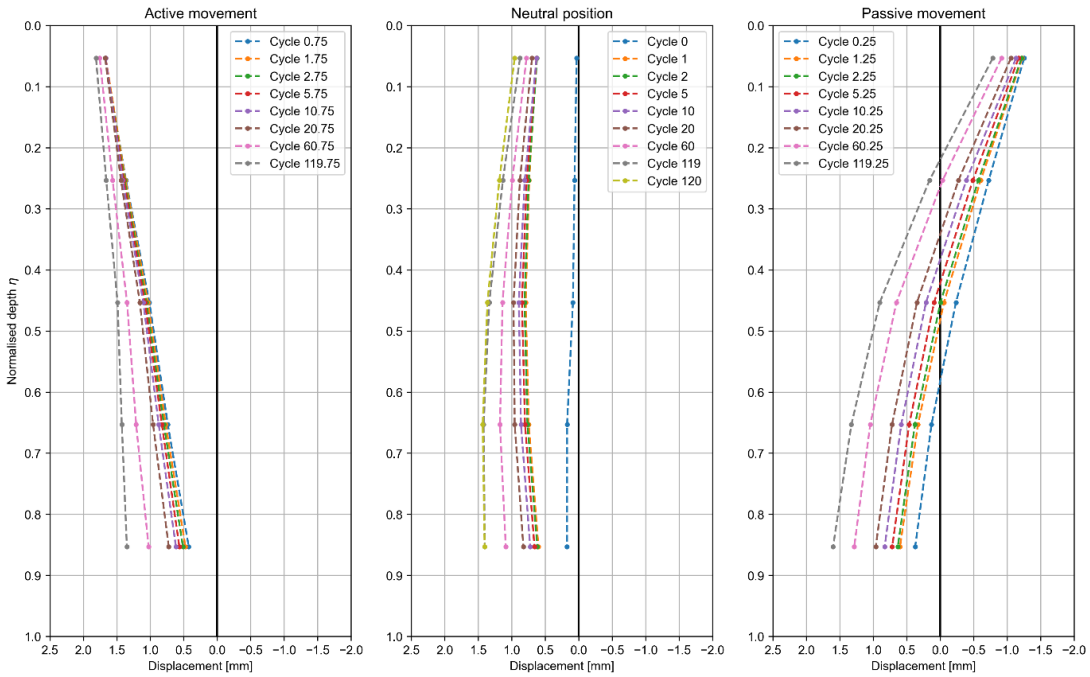

Figure 5-2: Measured abutment deflection for the 75 mm specimen.

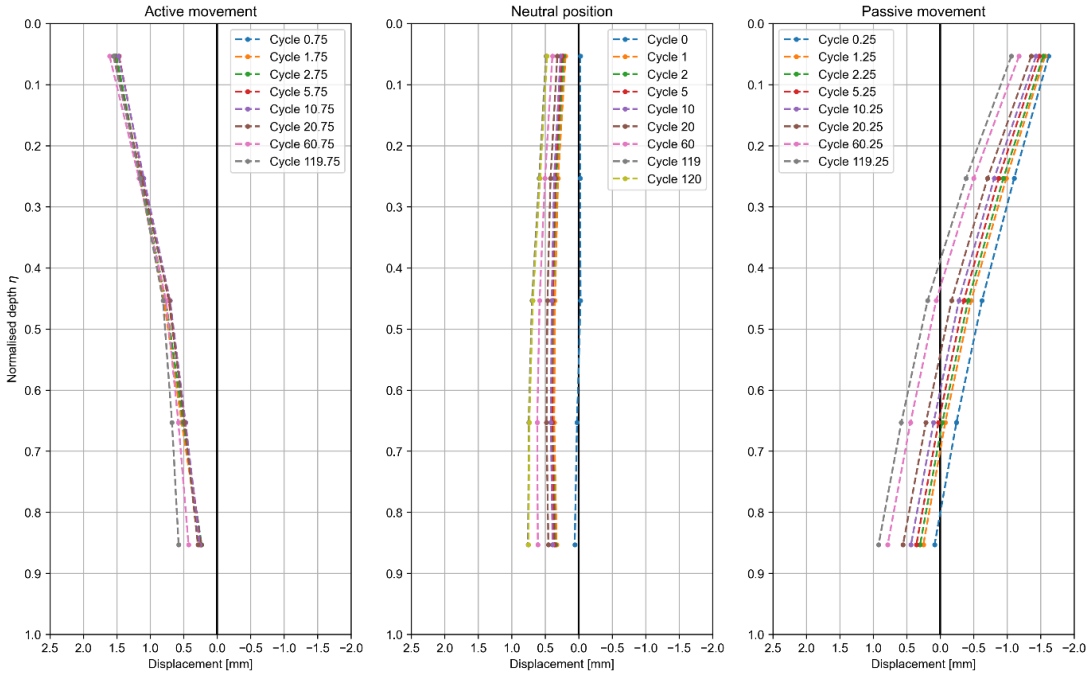

Figure 5-3: Measured abutment deflection for the 100 mm specimen.

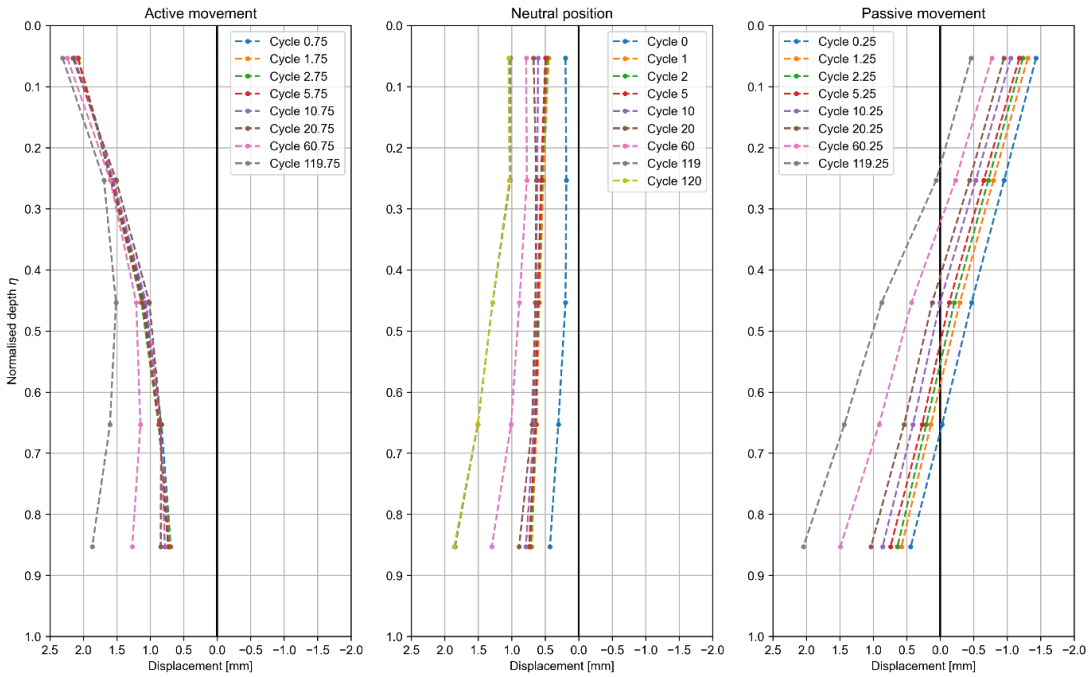

Figure 5-4: Measured abutment deflection for the 125 mm specimen.

All specimens showed an increase in deflection at all LVDT positions for increasing number of applied cycles, indicating that the sand mass densified during testing and was exerting more force compared to the initial at-rest pressures measured at cycle 0. For the more rigid specimens (thickness greater than the 50 mm abutment), the most displacement is present at the very bottom of the abutment walls. Due to the flexibility of the 50 mm specimen, the greatest deflection at cycle 0 took place at a normalised depth of roughly $\eta = 0.67$ (i.e., two thirds of the depth from the surface of the sand). The top of the abutment wall did not return to the at-rest position of cycle 0 ever after commencement of the cyclic loading. Compared to earth pressures shown in Figure 5-19 through Figure 5-22 prior, this discrepancy can be explained by the additional forces generated in the sand mass due to the densification occurring over time. The s*and's restraint to the rotational movement* of the abutment therefore appears to increase over time which causes the deck to shift away from the sand at an increasing magnitude as cyclic loading continues.

All specimens were pushed into the sand mass for an initial distance of 1.5 mm. The greatest displacements were observed for the 50 mm specimen (most flexible) and the 125 mm specimen (most rigid) at $\eta = 0.67$ and $\eta = 1.0$ respectively, similar to the neutral position. It is evident that the amount of deflection along the height of the abutment walls reduces for increasing stiffness. Again, the increasing restraint provided by the sand becomes more apparent for increasing number of cycles as there is a net shift away from the sand mass for each successive cycle as observed for the case of the neutral position, but only more pronounced. Based on the results of the true deflection as shown in Figure 5-1 through Figure 5-4, it is acknowledged that the base support designed for the experiment no longer restricted movement along the horizontal direction as the specimens were loaded cyclically and therefore can no longer be considered a *true hinged or pinned connection*. The horizontal movement of the base of the abutments could not be successfully restricted even with the presence of the

large self-weight of the more rigid specimens, which further reinforces the conclusion that the restraint of the sand mass becomes greater over time due to the ratcheting effect.

The overall deflected shape is reversed for the 50 mm specimen (most flexible) compared to the more rigid abutments. The familiar net shift away is also present for the active/negative movements during cycling with the exception of the 100 mm specimen where the position of the abutment wall remained relatively constant regardless of the number of cycles applied. The most deflection was measured for the 125 mm specimen (most rigid) where a distinct bent deflected shape occurred for each active movement. This was most likely due to the large horizontal displacement of the wall during cycling where the active movement of the deck portion of the specimen induced additional stresses within the abutment.

5.2.1 Curved shape of abutments

The *curved shape* was obtained by curve fitting a linear function using the very top and bottom readings of deflection and was used to offset all readings for the purposes of highlighting the bent shape of the abutment specimens. The *curved shapes* of the abutments for each specimen are shown in Figure 5-5, Figure 5-6, Figure 5-7, and Figure 5-8.

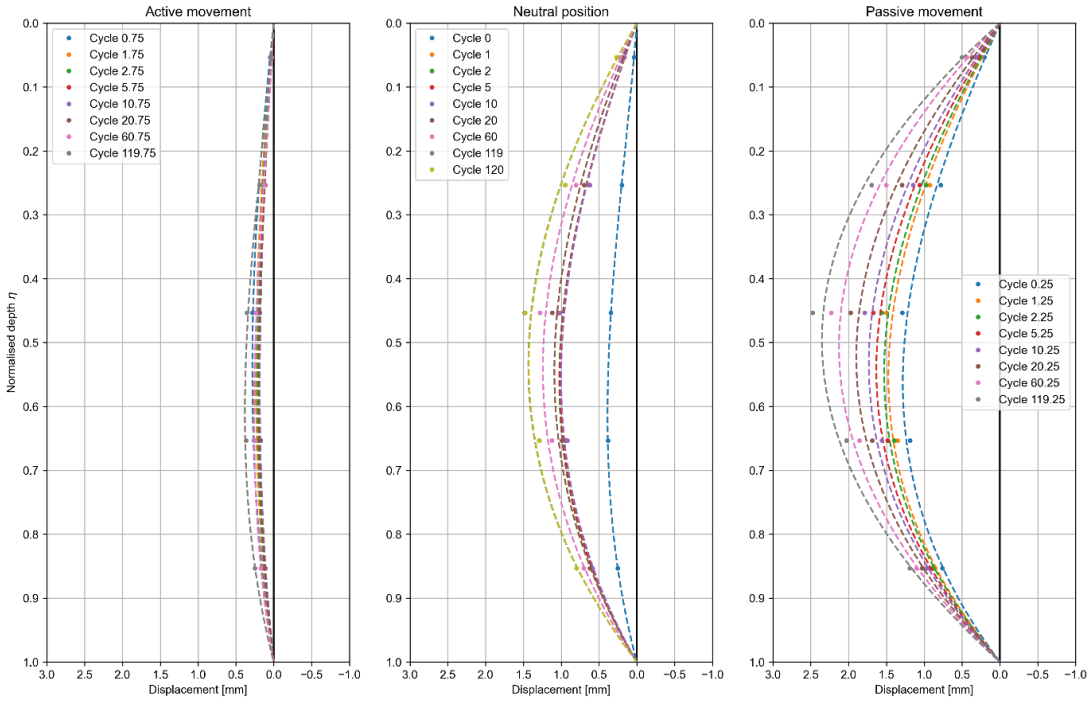

Figure 5-5: Abutment curvature shape for the 50 mm specimen.

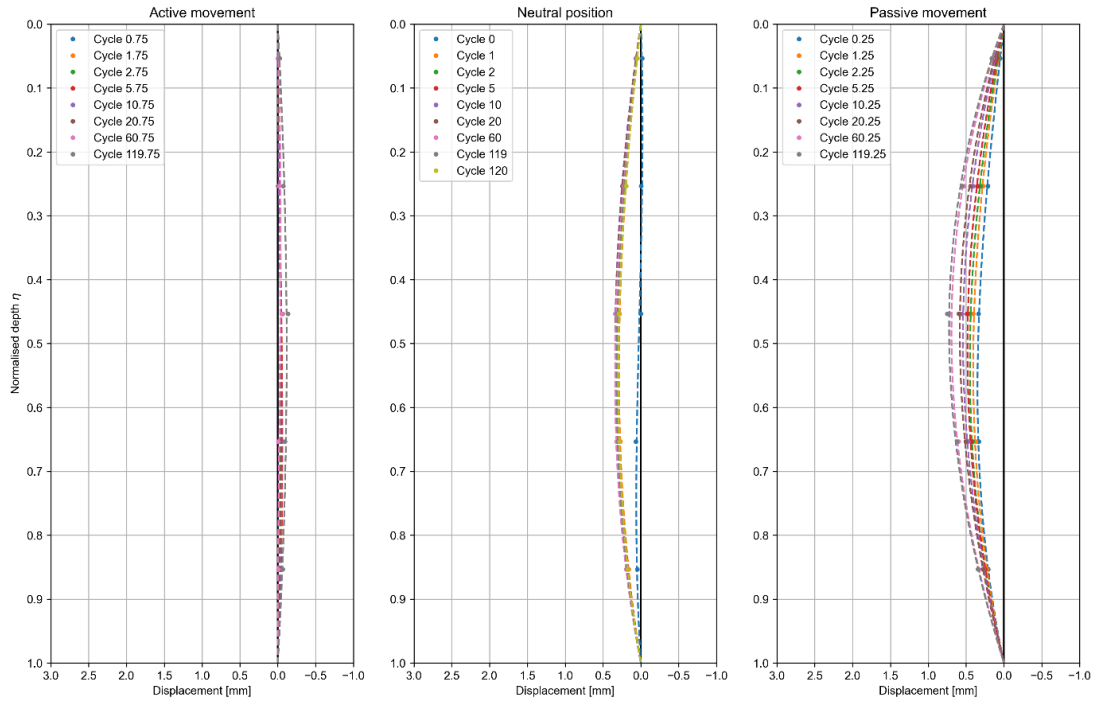

Figure 5-6: Abutment curvature shape for the 75 mm specimen.

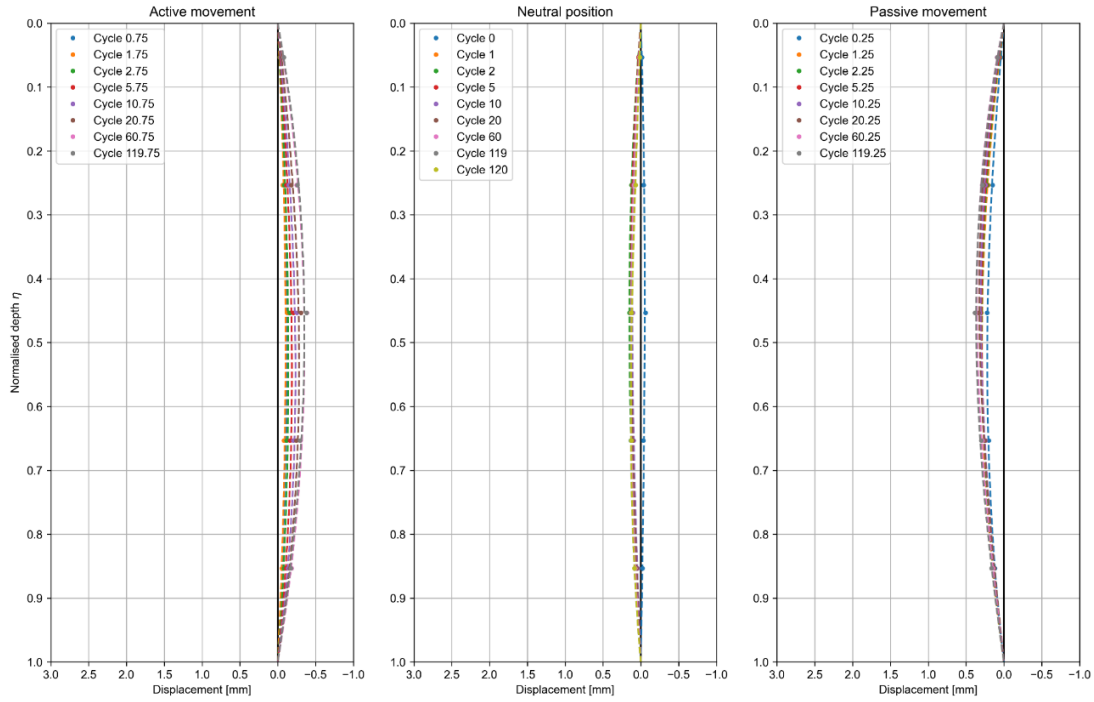

Figure 5-7: Abutment curvature shape for the 100 mm specimen.

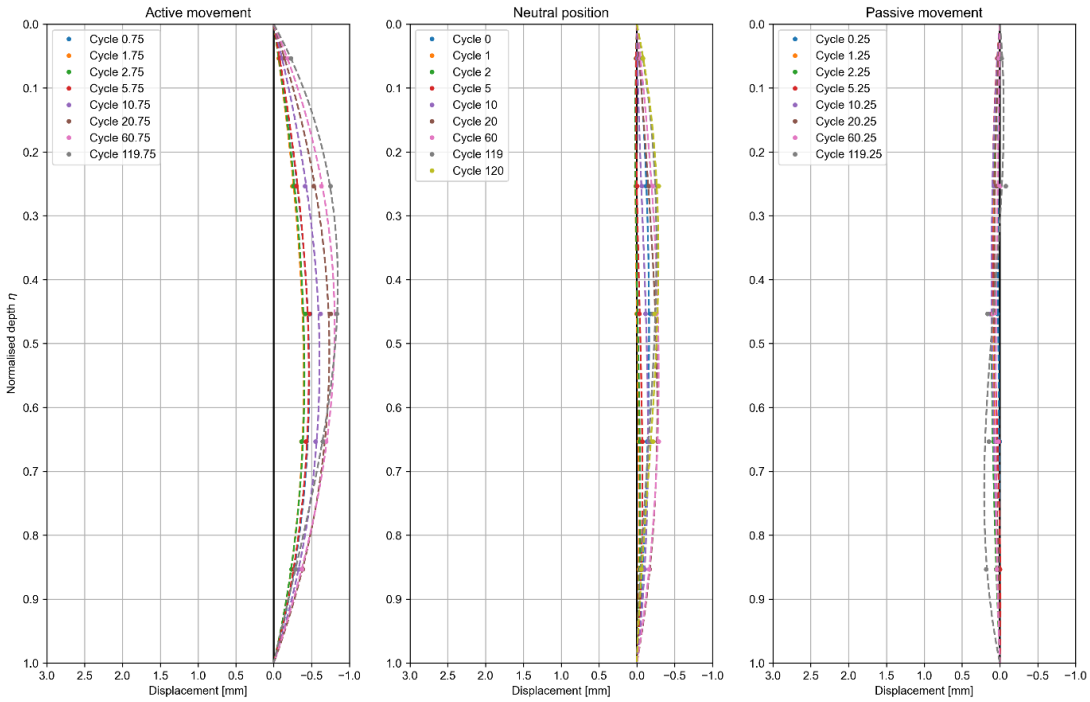

Figure 5-8: Abutment curvature shape for the 125 mm specimen.

For increasing thickness/stiffness of the abutment walls, a decrease in the curved shape takes place. The 125 mm specimen (most rigid) however showed more curvature in the reversed direction compared to the other specimens. This could again be attributed to the upwards and net shift away from the sand mass which in turn resulted in more bending taking place due to the test setup compared to the forces exerted by the sand mass. For all the specimens, the curved shape for any given cycle after cycle 0 specifically portray the shape of an arc with its point of maximum curvature located at approximately half-way along the height of the abutments. For the 75 mm and 100 mm specimens, the curved shape after cycle 0 remained roughly constant regardless of the number of applied cycles.

It can clearly be shown that for increasing stiffness/thickness of the abutments, the curved shape for every passive/positive movement showed a decrease. The 50 mm specimen (most flexible) demonstrated the most critical curvature amongst the specimens where every cycle led to an increase. This rate of increase rapidly decreases for the more rigid specimens such that the 125 mm specimen (most rigid) showed almost no curvature (at least enough to counteract the curvature caused by the experimental setup and the net shift upward and away from the sand mass).

The curvature for the 50 mm specimen (most flexible) was the only specimen that showed reversed curvature away from the retained sand compared to the more rigid specimens. It becomes evident that the more rigid specimens are far more susceptible to the effects of the active movement where the degree of abutment wall bending is governed by the active/negative movement instead of the forces applied by the sand mass. This effect is more pronounced for increasing stiffness/thickness of the abutment. Curvatures remain consistent regardless of the number of cycles for the 50 mm and 75 mm specimens only, where the 100 mm and 125 mm specimens developed much greater curvatures during the course of testing.

5.3 Abutment bending moments

The calculated bending moments for each specimen's abutment are shown in Figure 5-9, Figure 5-10, Figure 5-11, and Figure 5-12. The bending moments have been calculated based on the strain readings at the external and internal surfaces of the abutment wall (see Appendix A).

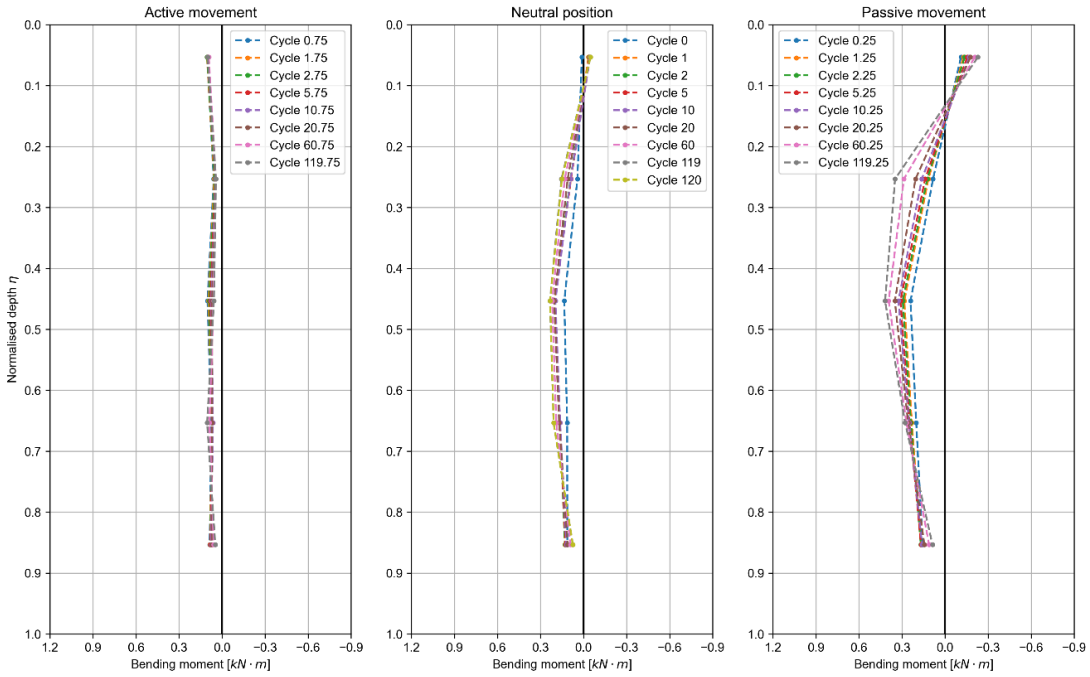

Figure 5-9: Abutment bending moments for the 50 mm specimen.

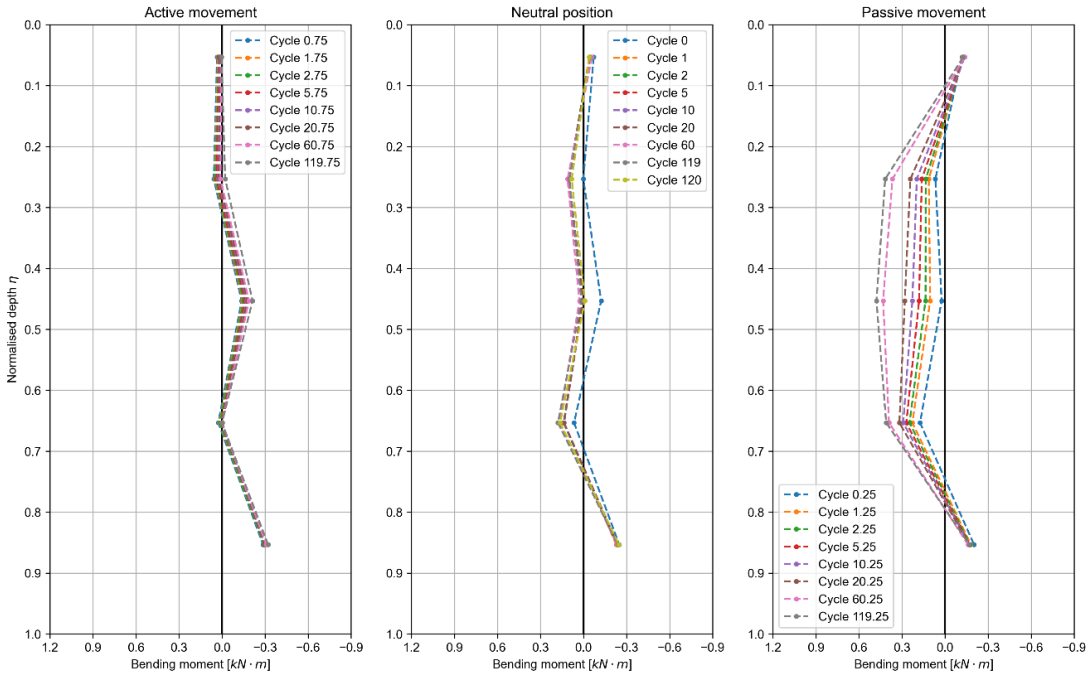

Figure 5-10: Abutment bending moments for the 75 mm specimen.

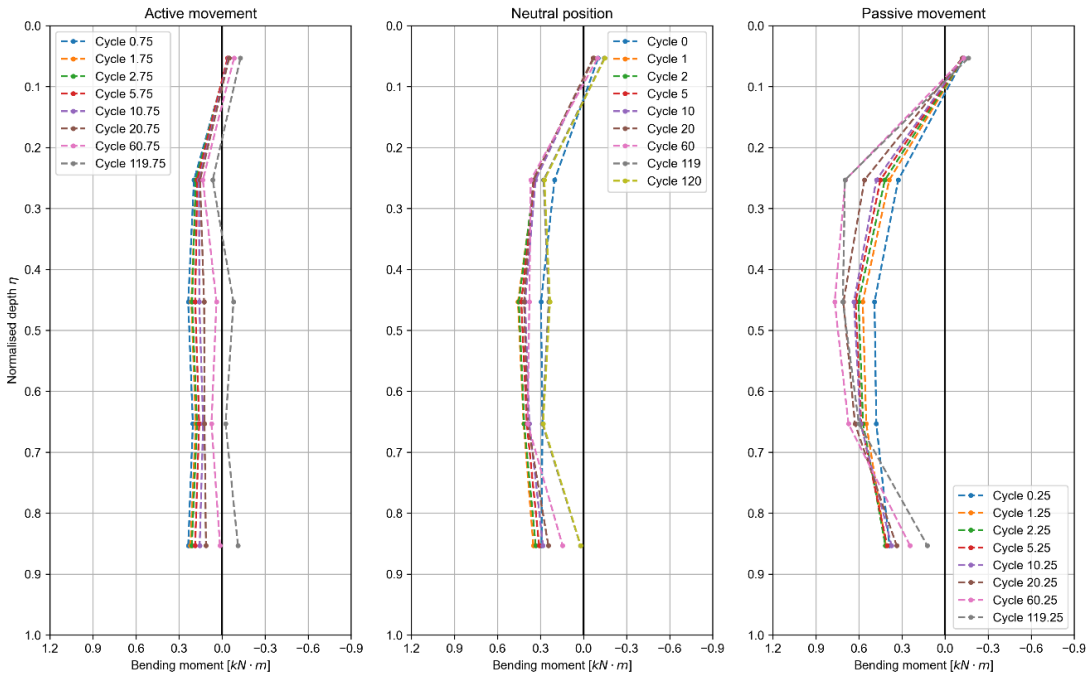

Figure 5-11: Abutment bending moments for the 100 mm specimen.

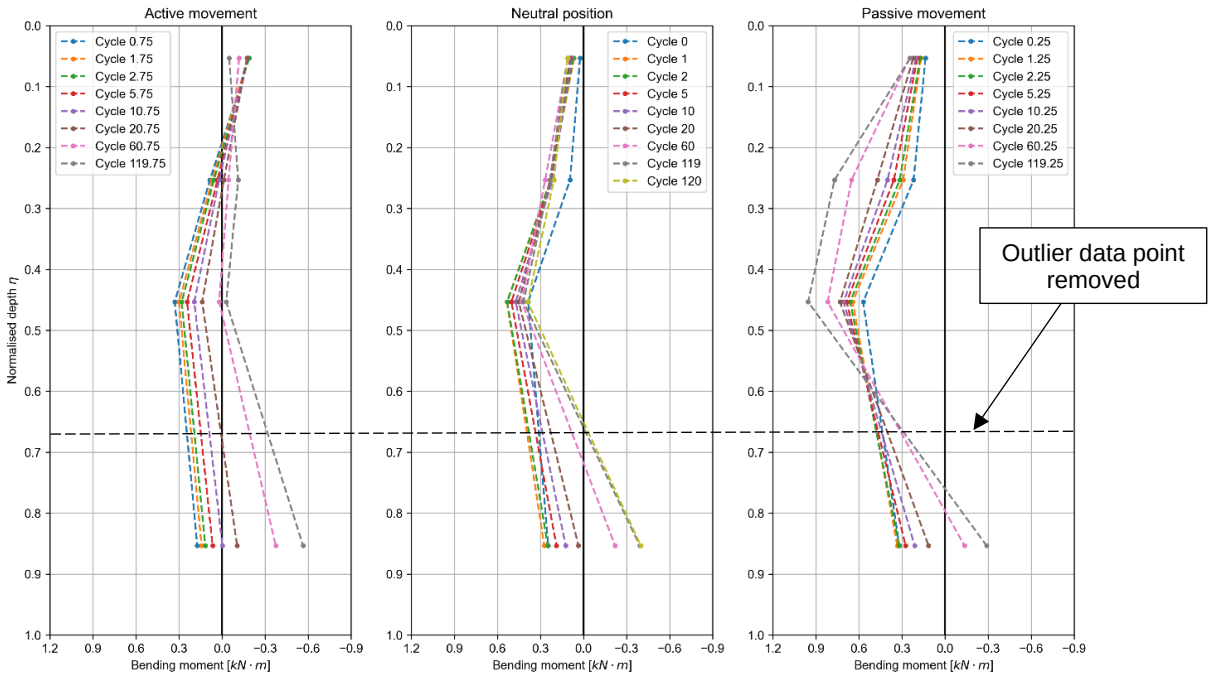

Figure 5-12: Abutment bending moments for the 125 mm specimen.

5.3.1 Discussion of abutment strains and bending moments

The internal strains at the neutral position were always negative, indicating that the internal side (refer to Figure 3-17) was always in compression (as per sign convention detailed in Chapter 4). For increasing number of cycles, it can be seen that the magnitude of the compressive strains at the internal face also increased for all specimens. As can be expected, for increasing stiffness of the abutment, the amount of compressive strain reduces as the section is stronger (i.e., section properties such as greater cross-sectional area and greater moment of inertia) and can resist greater pressures for the same levels of forces generated by the sand.

Strains generated at the external side at the neutral position showed tensile strains with the exception of the 75 mm specimen (possibly the consequence of the imperfect restraint at the bottom of the abutment wall). For increasing number of cycles, the strains become more compressive over time. The initial state of strains for the external side correlate with the mainly compressive strains of the internal side as there is an initial outward (positive) bending moment that is generated. Both sides of the abutment parts for all specimens encountered greater compressive strains over time. This can be explained by the net outward and upward shifts that occurred due to the increasing restraint exerted by the sand mass, and subsequently these compressive forces were generated due to a *more pronounced lack-of-fit effect* due to the confinement of the test setup and influence of the abutment-deck joint. In general (with the exception of the 75 mm specimen), for increasing stiffness of the abutment, it can be expected that the magnitude of the tensile strains generated on the external face of the wall will reduce.

Bending moments appear to increase for increasing stiffness/thickness of the abutment. The curvatures were mainly outward (positive according to the sign convention detailed in Chapter 4) which also increased for increasing number of cycles as the restraint of the sand increased due to the ratcheting effect.

Passive/Positive movements ($\Delta > 0$) followed the same behaviour as for the neutral position with only more pronounced magnitudes due to the higher earth pressures. The highest compressive and tensile strains recorded measured at roughly $160\ \mu\epsilon$ and $120\ \mu\epsilon$ respectively (excluding the measurements recorded at strain gauge 4 for the 125 mm specimen). These strains are large enough to potentially cause hairline cracking in the section which may have resulted in slightly more plastic material behaviour after the first half of applied cycles. These strains were thus not considered to have resulted in *plastic hinge formation* in either of the tested specimens.

In general, the abutment wall's external face strains for each specimen (again with the exception of the 75 mm specimen) demonstrate mostly tensile strains. For increasing number of cycles, it can be seen that the tensile strains reduce and become more compressive over time. The 75 mm specimen demonstrated purely compressive behaviour and remained relatively constant with slight deviation over time. The 125 mm specimen however showed significant initial tensile strains at strain gauge 4 (second lowest gauge) with strains exceeding $200\ \mu\epsilon$ which were considered to be an outlier and was thus excluded from Figure A-5, Figure A-9, and Figure 5-12.

It is acknowledged that the readings recorded by strain gauge 4 are potential outliers compared to the rest of the strain gauges as the other readings all agree with each other in terms of magnitude. For the purposes of this dissertation, the readings of strain gauge 4 for the 125 mm specimen (at the external side of the abutment) were considered potentially erroneous and were therefore neglected and are therefore not shown in Figure 5-12.

Bending moments at the active position are mainly positive. The 75 mm specimen demonstrated bending moments that were more negative overall. For increasing number of cycles, the bending moments of the specimens generated more negative bending moments which correlated with the strain readings and increased lack-of-fit effects as detailed prior.

5.4 Deck deflection, strains, & bending moments

The results for the deflection, strain and corresponding bending moments of the deck portion of the specimens were considered beyond the scope of the study and have therefore been excluded.

5.5 Measured earth pressures

Each earth pressure cell's measured data has been summarised into its active and passive cycles and are shown in Figure 5-13, Figure 5-14, Figure 5-15, Figure 5-16, Figure 5-17, and Figure 5-18.

The passive pressure measured at EPC 1 (Figure 5-13) showed a gradual increase at the start of testing and stabilised at around cycle 10 (100 mm specimen) to cycle 50 (50 mm specimen) where the earth pressures would then proceed to decrease. This trend is evident for all 4 specimens tested. The greatest pressure recorded by EPC 1 was measured as approximately 43 kPa for the 125 mm specimen (most rigid). The 50 mm specimen (most flexible) reached a maximum pressure that was comparable to the 50 mm specimen which reached approximately 38 kPa.

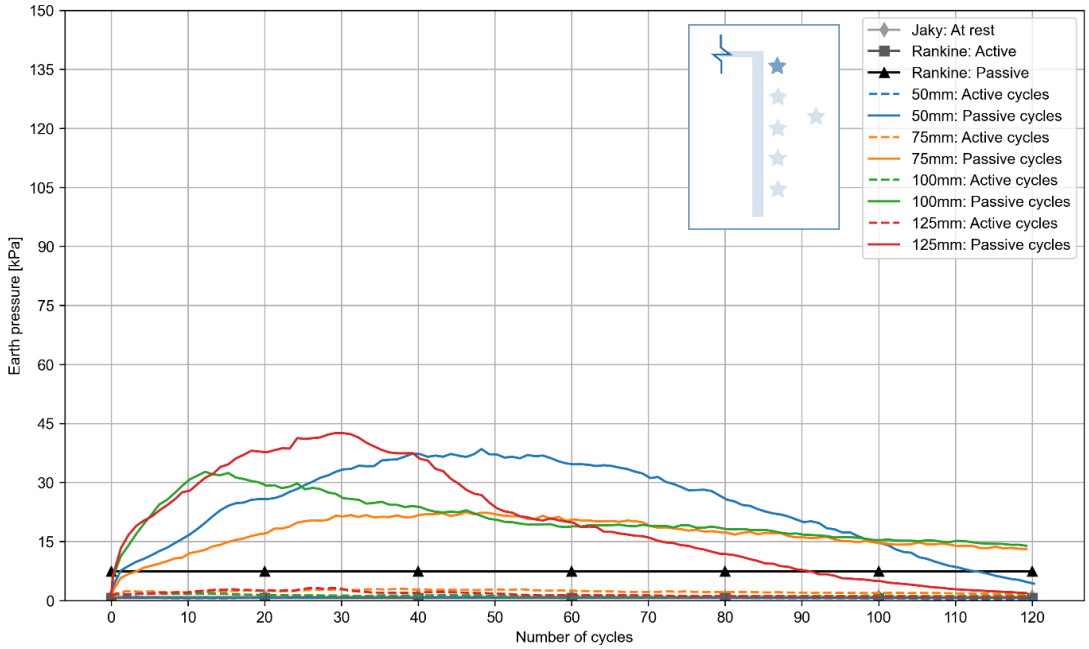

Figure 5-13: Active and passive pressures measured at EPC 1.

The rapid increase is most likely due to the fact that the greatest displacement occurs at the very top and that once the turning point is reached the decrease in pressure is as a result of the settlement that occurs over time until eventually the whole earth pressure cell is exposed (as was the case for the 50 mm and 125 mm specimens).

EPC 2's passive pressures (Figure 5-14) show a rapid increase for the first few cycles but immediately reduced and continued this reduction for about an average of 10 cycles where pressures then picked up again and continued until another turning point was reached (similar to the first turning point). Except for the case of the 100 mm specimen where the pressures appeared to plateau at a consistent value, all other specimens demonstrated a final stage where the pressures increased with no indication of another turning point nor plateau. It should be noted that EPC 2 demonstrated the greatest pressure measurement amongst all other earth pressure cells, specifically for the 125 mm (most rigid) specimen.

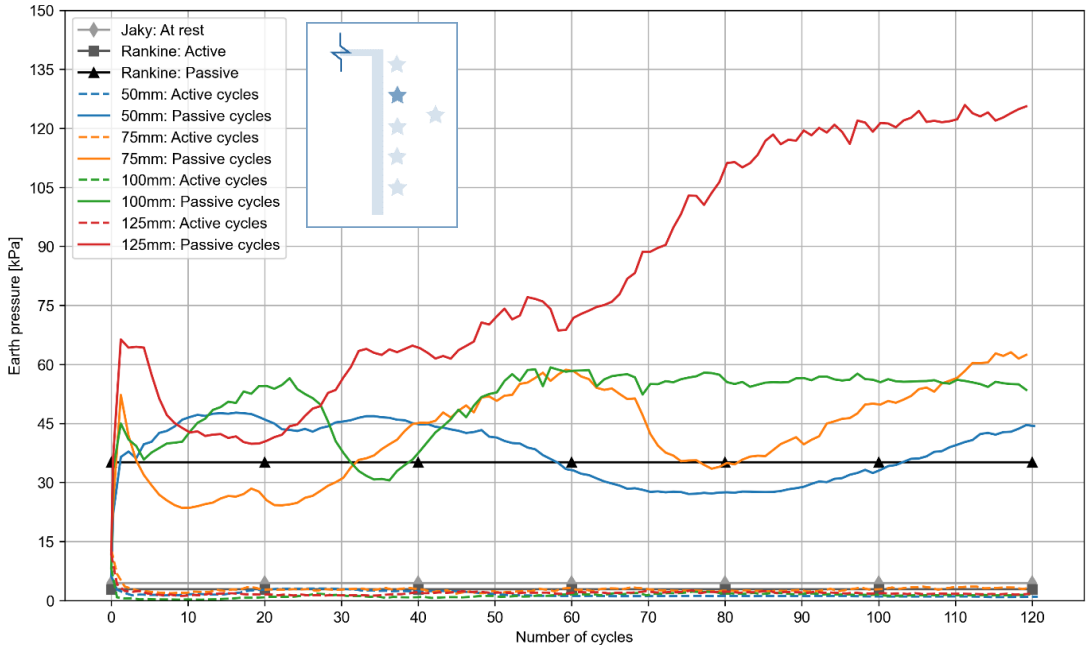

Figure 5-14: Active and passive pressures measured at EPC 2.

In general, the positions of each local peak in earth pressure vary for different abutment stiffnesses with no apparent trend with the exception of the 75 mm and 125 mm specimens which resembled each other closely in terms of the positioning of the local peaks and overall pressure trend. The 50 mm specimen (most flexible) appeared to *lag* behind the more rigid specimens where only 1 turning point is visible for the 120 cycles.

The turning points are most likely as a result of the settlement coupled with the ratcheting action taking place over time where a point is reached such that the increase in settlement per cycle is almost negligible (i.e., settlement no longer occurs) and therefore the pressure is finally allowed to increase again as seen near the end of the tests.

The passive pressures measured by EPC 3 (Figure 5-15) showed the greatest increase at the start of cycling where a rapid decrease occurred and continued for the following 20 cycles on average. Pressures at this point appeared to stabilise and were subject to a small rate of increase over time (albeit almost negligible in comparison to the largest rate of pressure increase) for the duration of the test. The 50 mm and 125 mm specimens (most flexible and most rigid respectively) showed nearly identical initial pressures whereas the 75 mm and 100 mm specimens also showed nearly identical pressures during the first few cycles.

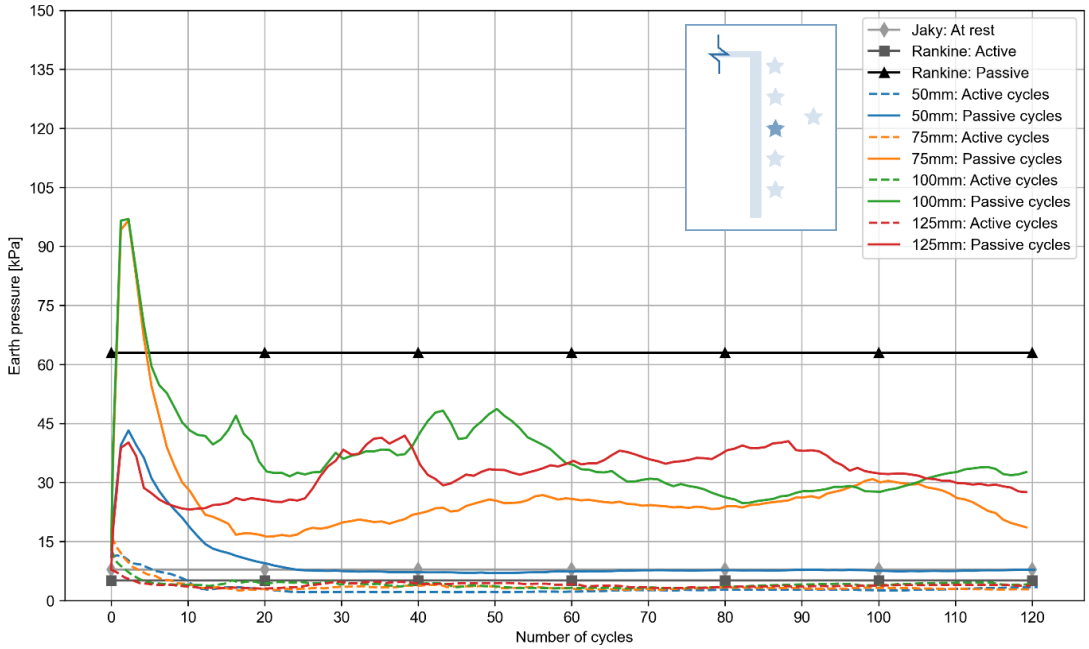

Figure 5-15: Active and passive pressures measured at EPC 3.

It should be noted that for the 50 mm specimen (most flexible), pressures recorded at this depth after the first 20 cycles resembled the at-rest pressures calculated from Jaky's equation for the earth pressure at rest and remained virtually the same throughout the test.

The passive pressures measured by EPC 4 (Figure 5-16) demonstrated a consistent trend amongst all specimens excluding the 50 mm specimen (most flexible). It can be seen that for increasing thickness (or stiffness) of the abutment, greater initial pressures can be expected with a corresponding rapid decrease over the first 20 cycles (similar to the EPC 3 measurements). The pressures soon reached a plateau with the 125 mm specimen (most rigid) having the largest overall pressure at this depth over time (although the very small difference between the specimens is acknowledged).

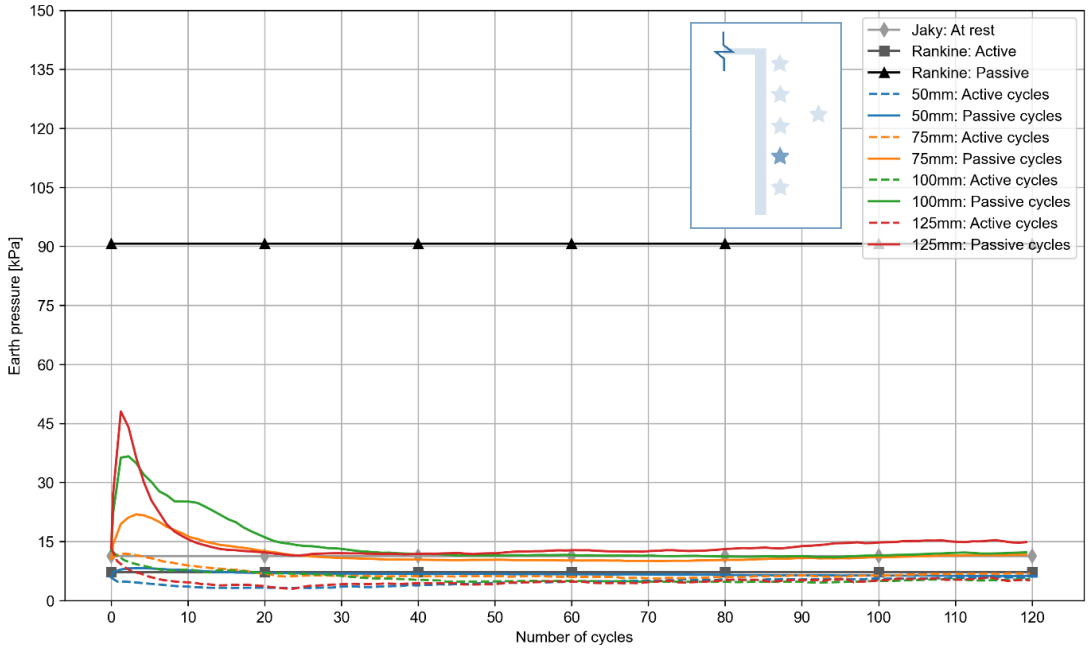

Figure 5-16: Active and passive pressures measured at EPC 4.

The 50 mm specimen however demonstrated almost no change after the 1st cycle. Passive pressures for the 50 mm specimen at EPC 4 closely resembled the calculated Rankine active pressure at this depth.

The pressures measured at EPC 5 (Figure 5-17), which was located close to the very bottom of the abutment, showed the lowest pressures amongst all the other earth pressure cells. Specimens with abutment thickness greater than the 50 mm specimen demonstrated decreasing passive pressures over the 120-cycle period which were less than the recorded active pressures at this depth. Beyond cycle 20, the more rigid specimens showed active and passive pressures that were smaller than the calculated Rankine active pressures. The passive pressures recorded at the very bottom earth pressure cell were in general smaller than the active pressures most likely as a result of the imperfect hinge at the bottom of the abutments which allowed movement away from the fill at the base.

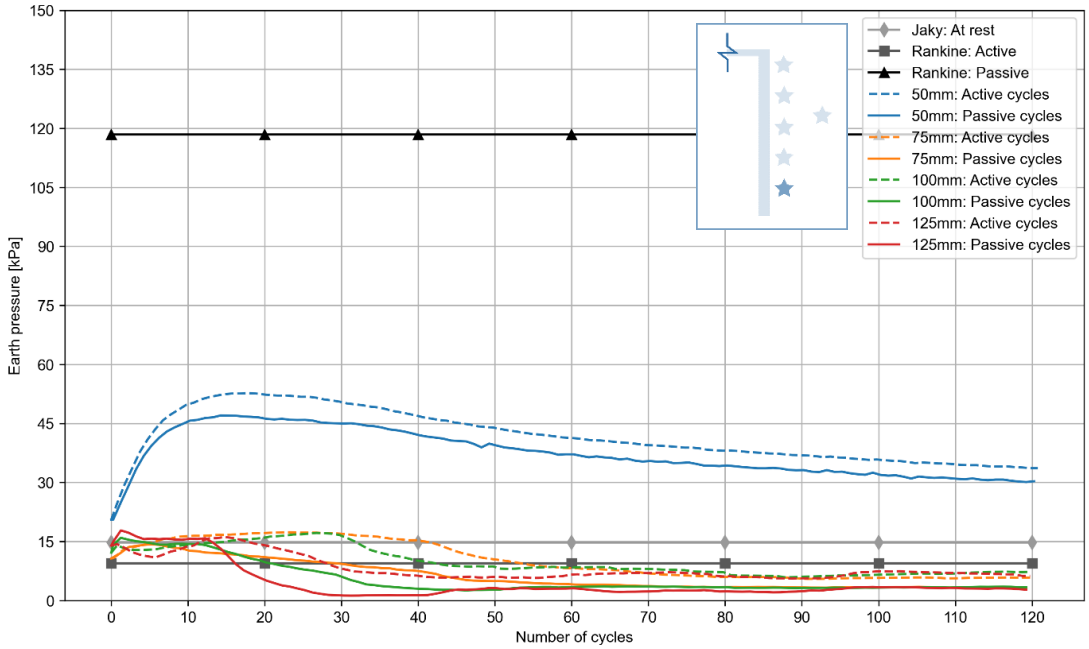

Figure 5-17: Active and passive pressures measured at EPC 5.

The 50 mm (most flexible) specimen's pressures recorded at EPC 5 however were anomalous in comparison to the other specimens. Both the active and passive pressures measured for the 50 mm specimen at this depth showed a much greater initial rate of increase and continued to increase for more cycles, peaking at around cycle 15 and slowly decreasing for the rest of the test. It can again be seen that for the very bottom cell, the 50 mm specimen's active pressures closely matched the passive pressure trend and even exceeded the passive pressures. A possible explanation for the irregular behaviour of the 50 mm specimen could be as a result of much greater deflection occurring along the abutment for each cycle. This greater magnitude of deflection could therefore have compensated for the imperfect hinge condition at the base of the abutment wall and can be substantiated by the results shown in Figure 5-1 through Figure 5-4 where the observed increase in deflection.

At the boundary cell, on the back wall of the steel frame strong box, passive and active pressure readings were recorded as indicated in Figure 5-18 and closely resembled each other during the test, regardless of stiffness/thickness of the abutment. The active movements did not reduce nor increase the overall pressures recorded at the boundary cell. The pressure increase observed over time was thus only as a result of passive movements and corresponding overall densification of the retained sand in the steel frame strong box (i.e., due to excessive restraint provided by the steel frame strong box).

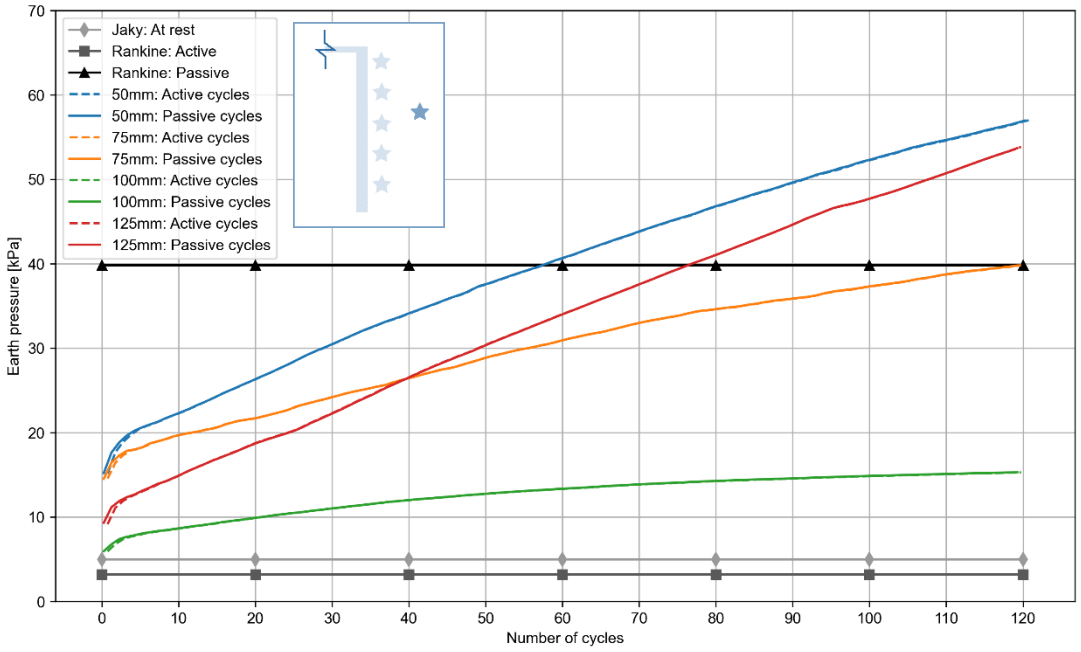

Figure 5-18: Active and passive pressures measured at the boundary EPC.

Comparing EPC 3's readings with the boundary EPC (which were both located at roughly the same height), it can be concluded that the movement of the sand particles due to the ratcheting effect which influenced the pressure trends of the specimens at EPC 3 and did not increase as smoothly and gradually over time as seen for the boundary EPC. This could explain the fluctuating trend observed for EPC 3's pressures.

5.5.1 Earth pressure sensor trends

The data recorded by cells 4 and 5 seem to imply that the sand located at increased depth (represented as η on the figures) was not exposed to the same degree of ratcheting (with the exception of the 50 mm specimen's results) which was most likely the consequence of an imperfect hinge at the base of the abutment wall.

It could therefore be concluded that there seems to exist a zone of influence caused by cycling where rotation is the governing form of movement of an integral bridge abutment. This zone therefore marks the region where the sand particles develop passive stresses due to particle interlocking effects and all other regions of sand outside of this zone are either virtually stationary (i.e., particles moved much less) or develop active pressures at the abutment as particles are shifted downward by each rotation of the abutment or due to the possibility of an imperfect hinge connection at the base of the abutment specimens.

The overall densification is therefore a result of the positive/passive movements only, as can be seen from the data recorded by the boundary cell (Figure 5-18).

In general, all earth pressure cells recorded active pressures which showed close agreement with the calculated Rankine active pressure and also remained relatively constant throughout the 120 cycles with the exception of the 50 mm specimen's pressures measured at EPC 5 (very bottom cell) as detailed before.

5.5.2 Earth pressure as a function of the normalised depth

The pressures displayed by Figure 5-19, Figure 5-20, Figure 5-21, and Figure 5-22 can be summarised and plotted as a function of the normalised depth (represented as η on the figures) for each specimen. The pressures were grouped and distinguished by movement of the abutment wall at different depths - either active (denoting a negative movement), neutral (the initial position of the abutment at the start of the test), and passive (denoting a positive displacement of the deck).

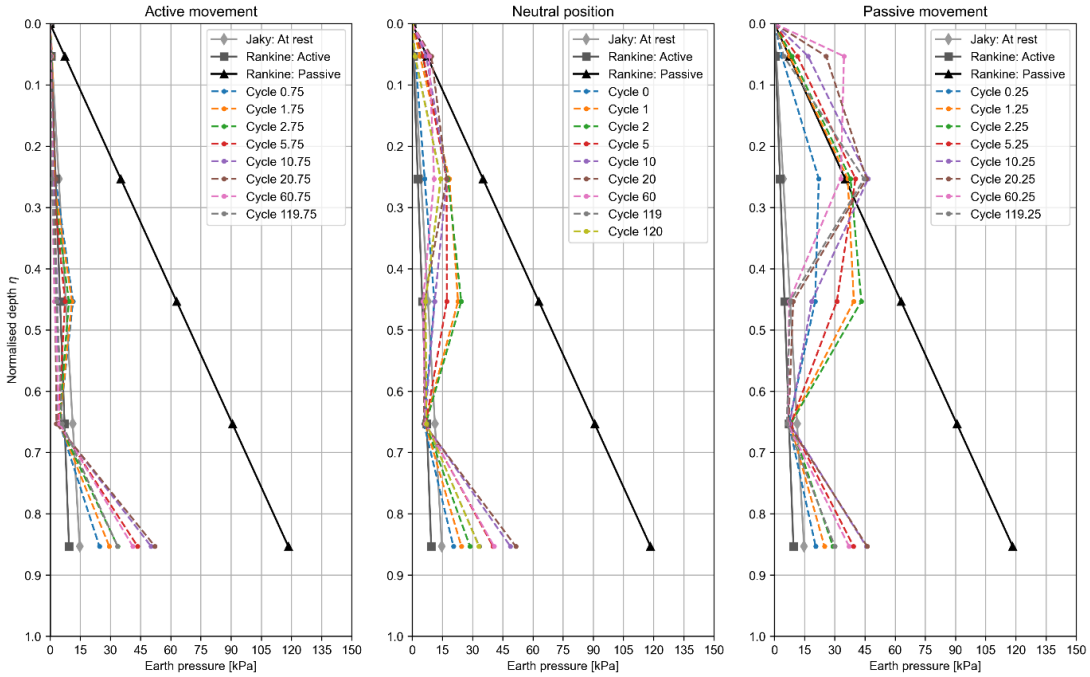

Figure 5-19: Measured earth pressures along abutment wall for 50 mm specimen.

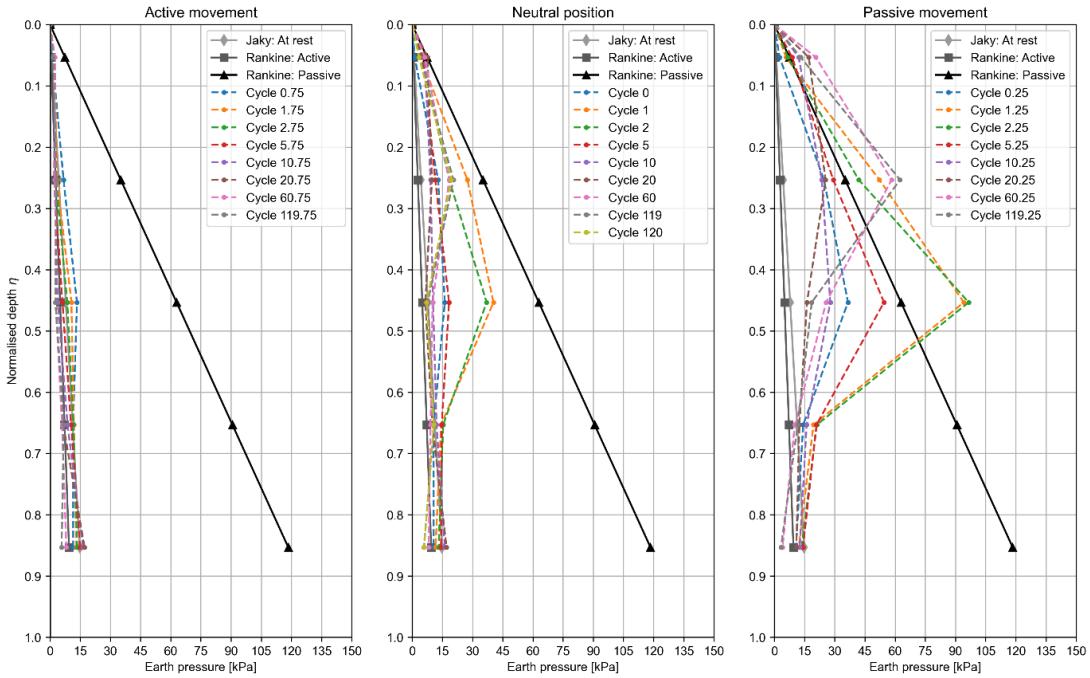

Figure 5-20: Measured earth pressure along abutment wall for 75 mm specimen.

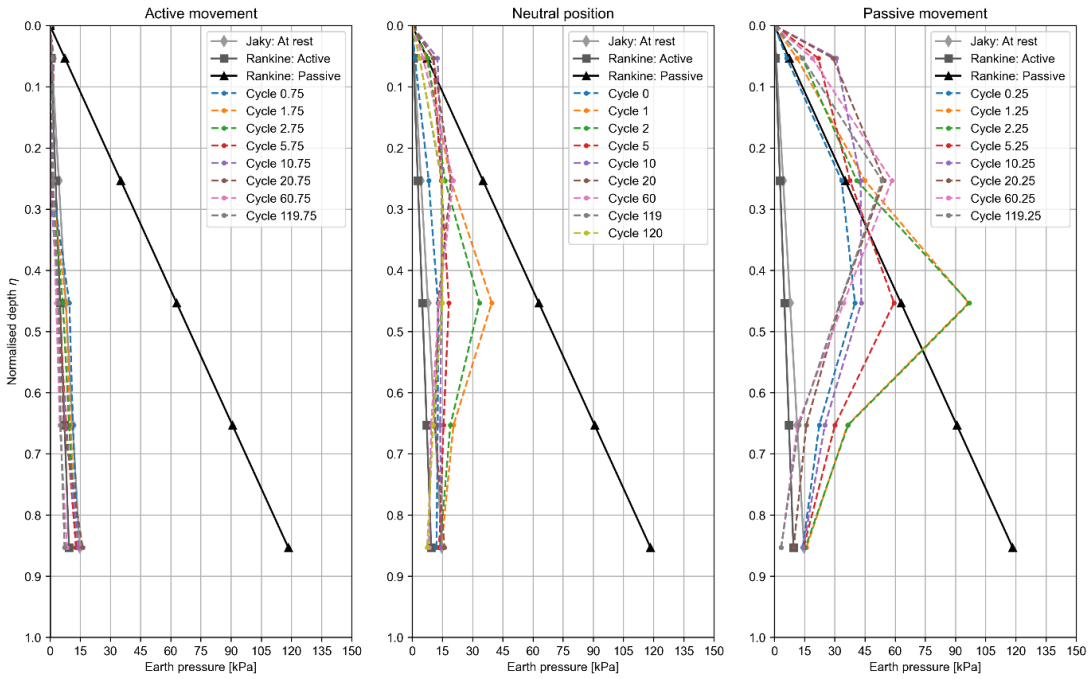

Figure 5-21: Measured earth pressures along abutment wall for 100 mm specimen.

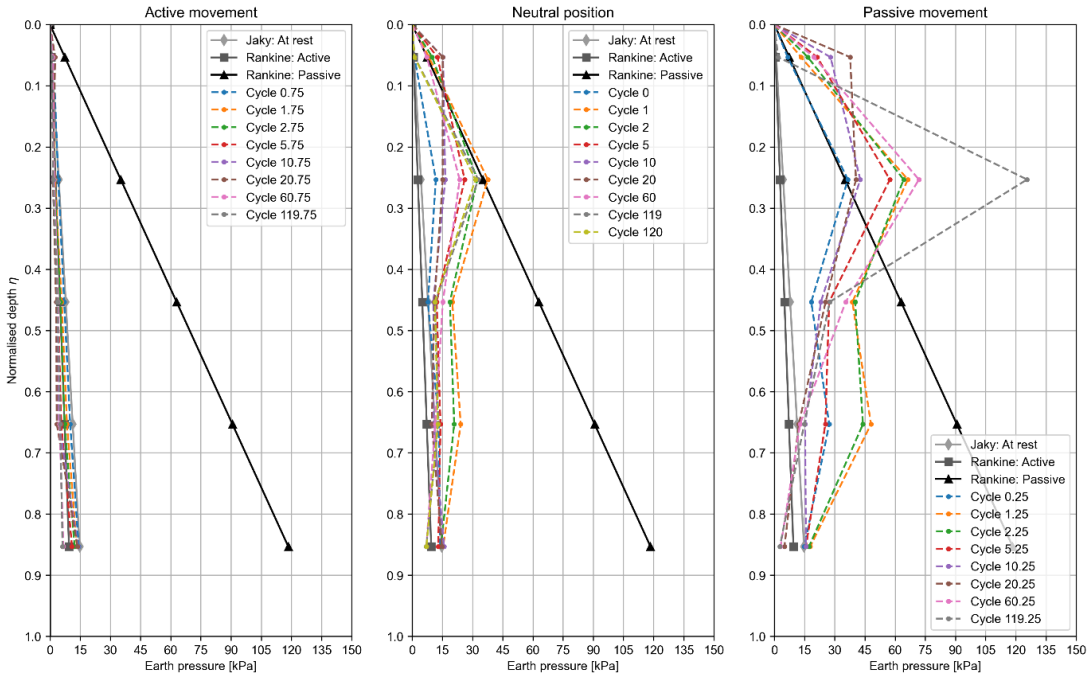

Figure 5-22: Measured earth pressures along abutment wall for 125 mm specimen.

Based on the results of Figure 5-19 through Figure 5-22, all specimens reached the calculated Rankine passive earth pressures at the top 3 earth pressure cells (namely EPC 1, 2, and 3) from either the first few cycles or by the end of the test due to the compounding lateral stress increase caused by ratcheting of the sand mass. The 125 mm specimen (most rigid) was able to reach full Rankine passive pressure at the neutral position after the first few cycles. The pressure distributions for the neutral and passive/positive movements of the deck are *non-linear* where a peak pressure is reached either at ECP 2 or EPC 3 which is roughly in the

middle. The experimental results from Figure 5-19 through Figure 5-22 are in good agreement with the work done by Walter *et al.* (2018), Lehane (2011), Nam and Park (2015), Sandberg *et al.* (2020), and Springman *et al.* (1996).

5.5.3 Measured resistance to movement

Measurements made by the force transducer positioned at the end of the actuator that was used to displace the deck horizontally (and therefore the top of the abutment) were analysed to assess the overall impact of the densification occurring due to ratcheting for each specimen.

The net force measured by the force transducer over the course of the tests are shown for each specimen in Figure 5-23. This force is indicative of the resistance of the sand to movement induced by the actuator. It is clear that all specimens showed increasing force exerted by the sand for every successive cycle applied to the abutment wall. This therefore proves that ratcheting (densification) occurred in the retained sand for the applied displacement amplitude of 2 mm for every specimen tested. Based on the data shown in Figure 5-23, there is no apparent plateau after an applied 120 cycles (i.e., no *resilient behaviour* has yet been reached) but the data does seem to suggest that there is an existence of an asymptote beyond 120 cycles.

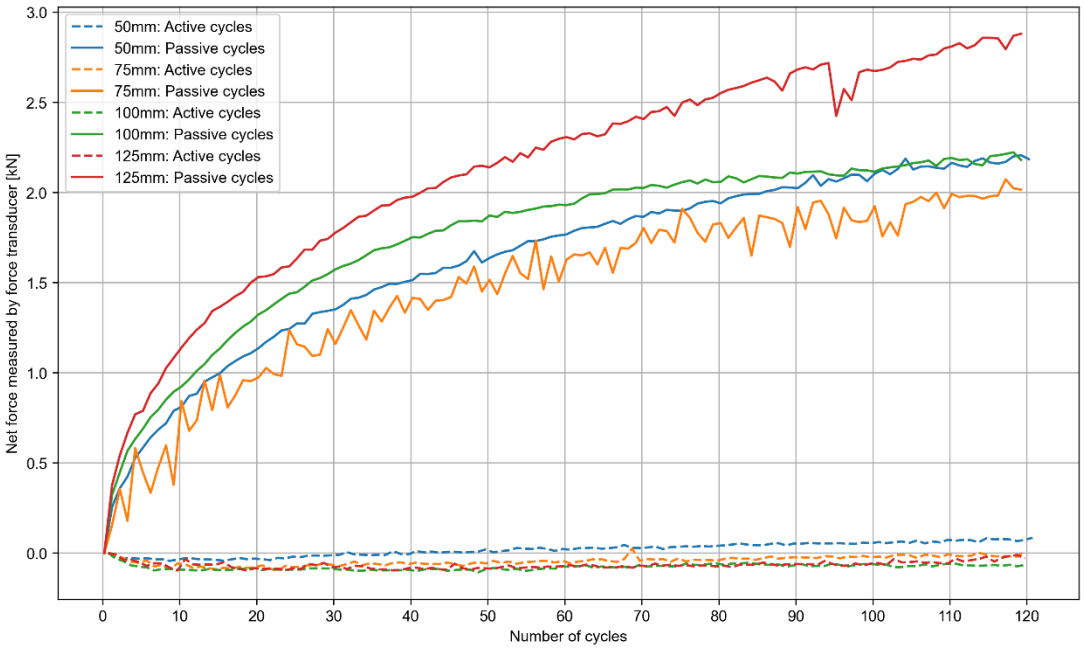

Figure 5-23: Net force measured by the force transducer (due to both active and passive movements) for each abutment specimen over 120 cycles.

It should be noted that the expected monotonic increase in net force measured by the force transducer is contradicted by the results from the 75 mm specimen's test as the lowest measured force at the end of the 120 cycles occurred for the 75 mm specimen. This could possibly imply that there is a behaviour change at a certain abutment stiffness between rigid and flexible abutments.

Figure 5-24 shows the factor of increase in force measured by the force transducer for each cycle. This factor is calculated by offsetting all force values using the first passive/positive movement's measurement of force ($F_{Cycle\ 0.25}$), expressed mathematically as follows:

$$factor = \frac{F_{Cycle\ N} - F_{Cycle\ 0.25}}{F_{Cycle\ 0.25}}\ for\ N \geq 0.25 \qquad \text{Equation 5-1}$$

The first passive movement force is used to correct any potential lack-of-fit forces present for any given specimen. This is possible due to the fact that the friction forces caused by the test setup are virtually negligible in comparison to the passive movement forces for each positive movement induced by the actuator. This factor therefore represents the change in force in comparison to each positive/passive displacement of the deck and not the neutral position.

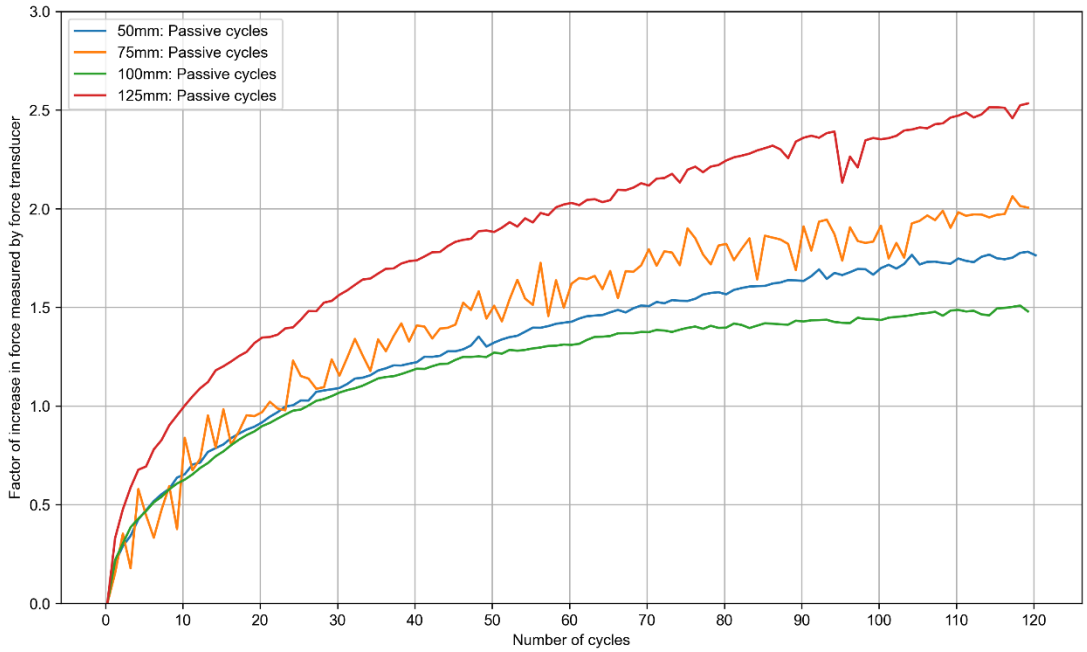

Figure 5-24: Factor of increase in force measured by the force transducer (due to both active and passive movements) over 120 cycles.

Figure 5-23, Figure 5-24, and Figure 5-26 demonstrate that the 125 mm specimen (most rigid) showed the greatest overall increase in force measured by the force transducer. From Figure 5-25 which shows the maximum force measured for varying abutment stiffnesses in terms of both the wall thickness and the dimensionless modified Rowe's flexibility number (as defined in Equation 2-4 and Table 5-1), a turning point is evident where the 75 mm specimen showed the smallest maximum resistance to movement developed after 120 cycles.

Table 5-1: Dimensionless modified Rowe's flexibility number for abutment specimens as defined by Potts and Bond (1994) (Equation 2-4).

Abutment specimen:	$\boldsymbol{log(\rho^*)}$:
50 mm	3.53
75 mm	2.99
100 mm	2.61
125 mm	2.32

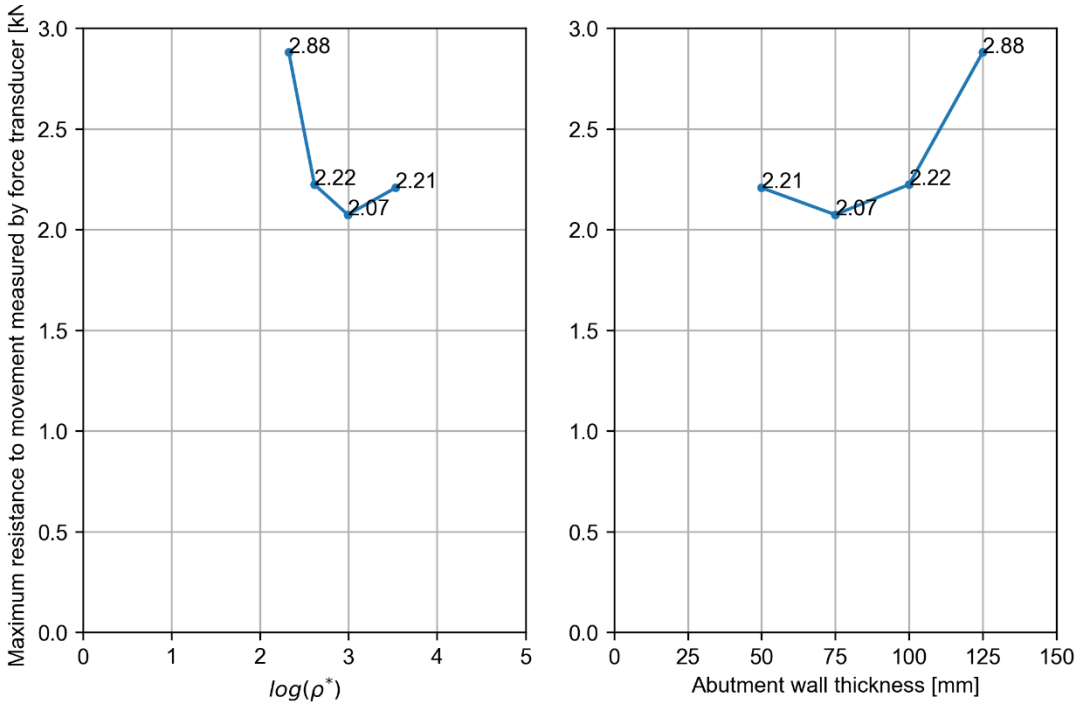

Figure 5-25: Maximum resistance to movement measured by the force transducer for different flexibility numbers/wall thicknesses.

Figure 5-26 shows the fraction of the maximum force measured by the force transducer over time. Analogous to the factor of increase calculation, this fraction is calculated by offsetting all force values using the first passive/positive movement's measurement of force ($F_{Cycle\ 0.25}$), and is expressed mathematically as follows:

$$fraction = \frac{F_{Cycle\ N} - F_{Cycle\ 0.25}}{F_{max}} \quad for\ N \geq 0.25 \qquad \text{Equation 5-2}$$

Where:

$$F_{max} = \max\{F_{all\ cycles} - F_{Cycle\ 0.25}\}$$

Analysis of Figure 5-26 revealed that, in general, all specimens reached the same ratio of earth pressure to the force measured at cycle 120 at any particular cycle throughout the test. The 100 mm specimen appears to deviate slightly by an additional fraction of 0.1 at any given cycle beyond cycle 15 compared to all other specimens. For all specimens tested, roughly 40% of the expected maximum earth pressure that can develop over 120 cycles is reached after only 10 cycles. This is in good agreement with the approximate 50% evident in the experimental data acquired by England and Tsang (2000; 2001; 2007).

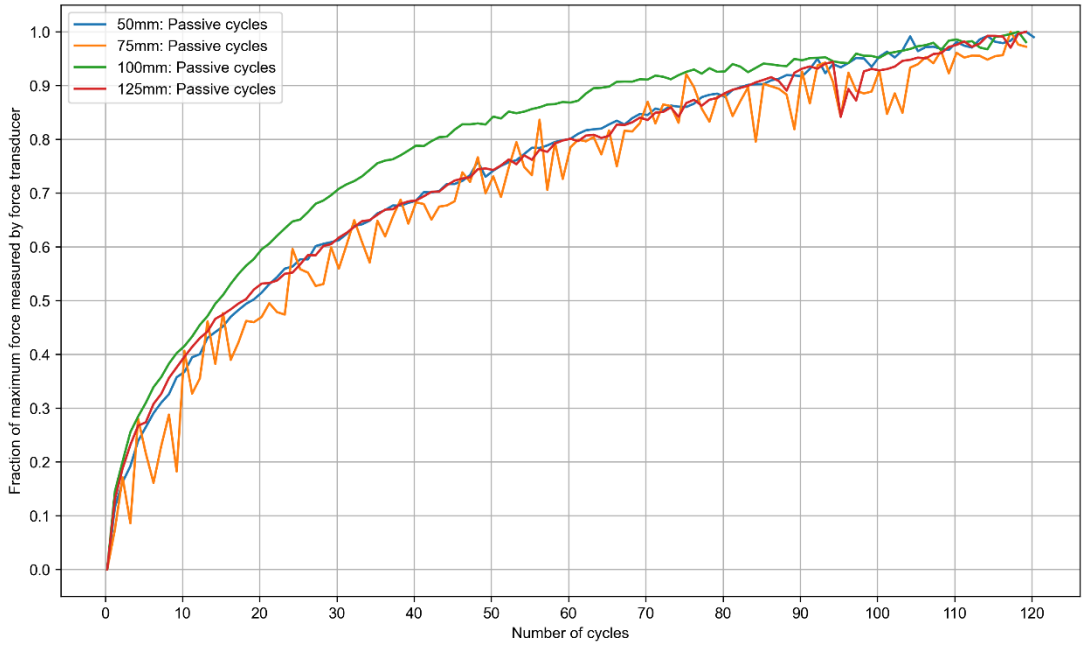

Figure 5-26: Fraction of maximum force measured by the force transducer for each abutment specimen over 120 cycles.

5.6 Fixity of abutment wall during testing

It is acknowledged that the connection at the bottom of the abutment wall may have been an imperfect hinge and is a significant shortcoming of the study. This could potentially explain the anomalous behaviour the measurements recorded by the instrumentation installed at the lower half of the abutment wall as the abutment wall did unintentionally experience both vertical movement and horizontal movement away from the retained sand. The self-weight of the abutment specimens was not sufficient to eliminate the possibility of uplift of the abutment wall. The implication of the recorded uplift on piled or framed abutments should therefore be considered by design engineers.

5.7 Particle image velocimetry of the abutment-retained sand

The following section details the results obtained from *Particle Image Velocimetry* (PIV) of the images taken of the sand mass during each test using GeoPIV-RG (Stanier *et al.*, 2015). It should be noted that all results contained in this section are based on the calculations performed for the last cycle relative to cycle 0 of each test.

5.7.1 Sand displacement contours

The horizontal, vertical and resultant displacements calculated from the PIV analyses for each specimen can be seen in Figure 5-27, Figure 5-28, and Figure 5-29 respectively. It is important to note that the blank areas in the displacement contours at the top left corner of each plot

shown are the *stray subsets* (detailed in Table 3-13) and is not a visual indication of the settlement that occurred.

Analysis of the total calculated horizontal displacement of the sand (Figure 5-27) revealed that most of the positive displacement (i.e., to the right towards the back of the steel box) occurs roughly between a quarter to a third of the depth as measured from the surface of the sand. This is in excellent agreement with the measured earth pressures of EPC 2 and EPC 3 (Figure 5-14, Figure 5-15, and Figure 5-19 through Figure 5-22). The surface of each test's retained sand showed a negative displacement (i.e., to the left towards the face of the abutment) which agrees with the fact that settlement must occur due to the reduction in sand volume from the densification caused by the cyclic loading.

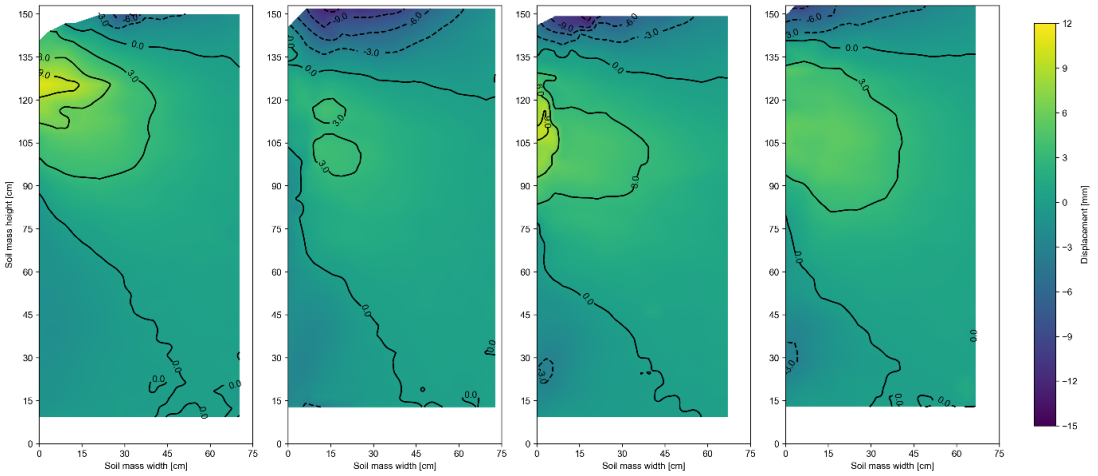

Figure 5-27: PIV horizontal sand displacement contours for (a) 50 mm, (b) 75 mm, (c) 100 mm, and (d) 125 mm specimens.

For the specimens that have an abutment thickness greater than 50 mm, for increasing abutment thickness, the greater the *bulb of positive horizontal displacement* that is taking place at the quarter to third of the depth range from the surface of the sand. The 50 mm specimen showed the greatest amount of positive horizontal displacement, whereas the 75 mm specimen showed the greatest amount of negative horizontal displacement. The vertical displacements in Figure 5-28 displayed a trend where for increasing abutment thickness, the deeper the extent of negative (downward) vertical displacement, which suggests that the thinner abutments are deflecting more and hence the rotations of the thinner abutment walls are not affecting the full height of the sand mass as opposed to the most rigid specimen. The most flexible specimen seems to show the least vertical displacement whereas the 75 mm specimen appeared to have displaced the most which agrees with the findings from the horizontal displacements calculated.

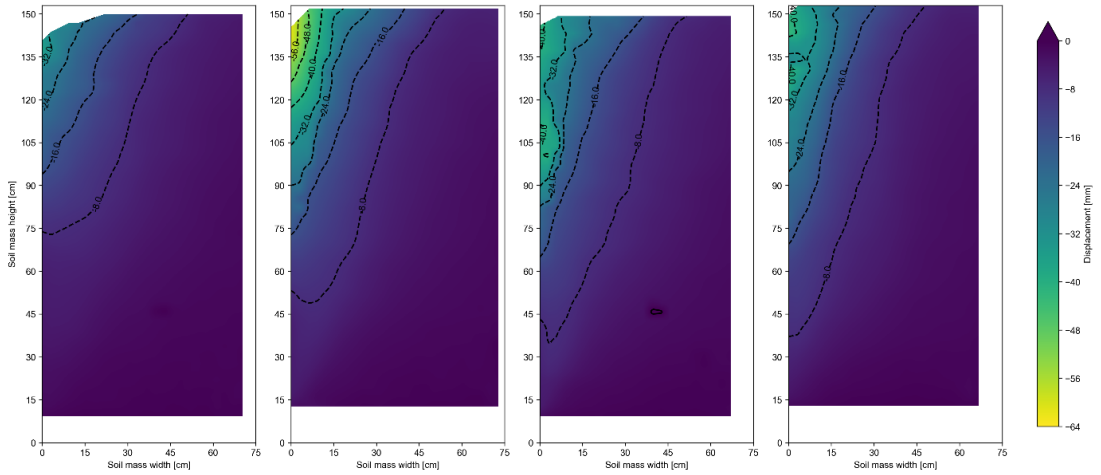

Figure 5-28: PIV vertical sand displacement contours for (a) 50 mm, (b) 75 mm, (c) 100 mm, and (d) 125 mm specimens.

Figure 5-29 shows the resultant displacements derived from Figure 5-27 and Figure 5-28. It is evident that the 50 mm specimen (most flexible) resulted in the least amount of sand displacement, and the 75 mm displayed the most in contrast. For the more rigid specimens (i.e., the 100 mm and 125 mm abutments), the resultant displacements were in good agreement with each other where the 100 mm wall showed slightly higher overall displacements at the face of the abutment wall.

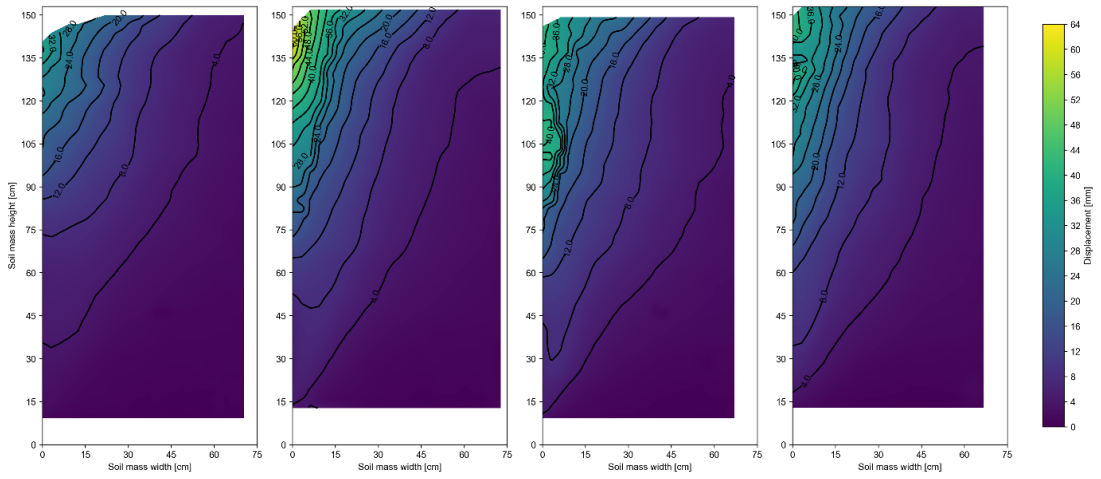

Figure 5-29: PIV resultant sand displacement contours for (a) 50 mm, (b) 75 mm, (c) 100 mm, and (d) 125 mm specimens.

5.7.2 Sand particle flow behaviour

From the PIV results for displacements (horizontal, vertical, and resultant), flow vectors and streamlines were computed for each specimen after exposure to 120, 2 mm displacement cycles as shown in Figure 5-30 and Figure 5-31 respectively.

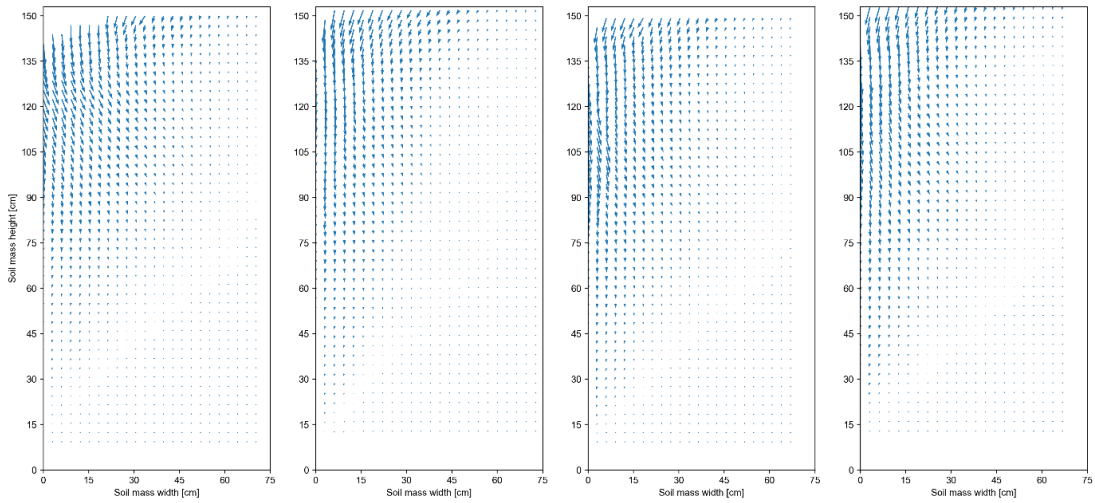

Figure 5-30: PIV sand displacement field vectors after 120 cycles for the (a) 50 mm, (b) 75 mm, (c) 100 mm, and (d) 125 mm specimens.

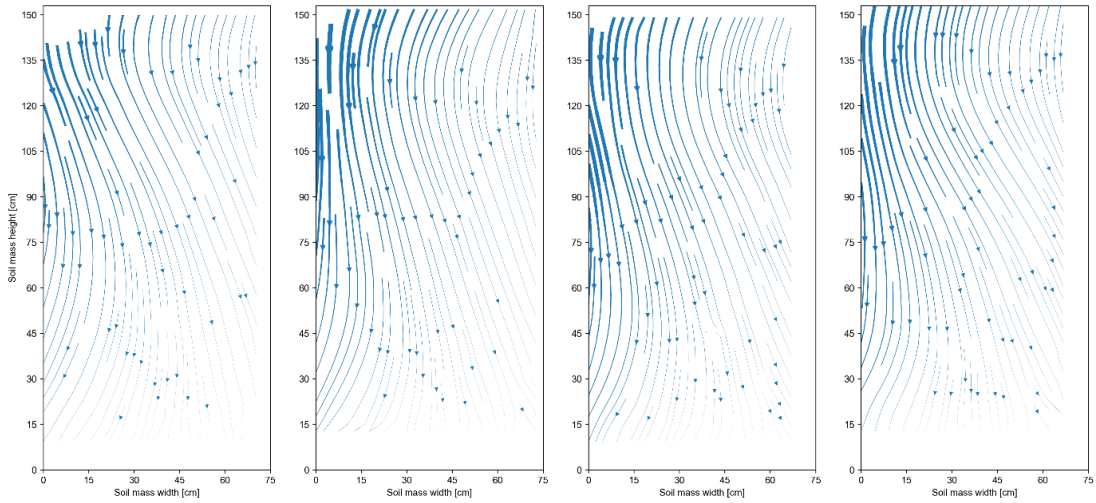

Figure 5-31: PIV streamlines indicating direction and magnitude of sand displacement after 120 cycles for the (a) 50 mm, (b) 75 mm, (c) 100 mm, and (d) 125 mm specimens.

It is evident from the displacement field vectors (Figure 5-30) that a triangular wedge (similar to the findings of Ng *et al.* (1998a)) of movement is present for all specimens after 120 cycles which is approximately situated at the upper third portion of the sand mass.

The particle flow behaviour is represented by the streamlines plot (Figure 5-31) which was derived from the flow vectors. The direction of flow is indicated by arrows and the thickness of each streamline represents the magnitude of the *resultant displacement* that occurred along the individual streamline. All specimens appear to exhibit the same sand particle flow pattern where particles at the surface level of the sand first tend to flow towards the face of the abutment and downward where after a change in the horizontal direction to the right (towards

the back of the steel box) occurs and eventually creates an *S-shape*. The sand particle displacement is greatest at the face of the abutment wall at the upper quarter to upper third depth measured from the surface of the sand. A particle positioned at the surface will therefore initially be displaced downwards towards the face of the abutment due to settlement occurring from the sand mass densifying during cyclic loading and eventually will be pushed further horizontally into the sand mass due to the rotational movement of the abutment.

5.7.3 Horizontal and vertical settlement extent for each specimen

Figure 5-32 and Figure 5-33 indicate the horizontal and vertical settlement extents respectively which have been measured using the final images after cycling (see Appendix A) and have been plotted against the thickness and Rowe's normalised flexibility number (ρ^*) for each specimen. The horizontal settlement extent shown in Figure 5-32 denotes the distance from the face of the abutment wall to the point at the surface of the sand which has not displaced after 120 cycles. Although the horizontal extents of the 75 mm and 100 mm specimens are nearly identical, no apparent trend seems to exist according to the experimental data which was possibly the consequence of the imperfect hinge at the base of the abutment. The horizontal settlement extent for 2 mm amplitudes at 120 cycles can be expected to be roughly in the range of 160 mm to 230 mm for an abutment wall that is 1.5 m tall. The limited extent of the horizontal movement (<240 mm) confirms that the back of the steel frame strong box (1000 mm from the concrete abutment wall) was far enough removed from the moving abutment wall to not affect the measured behaviour.

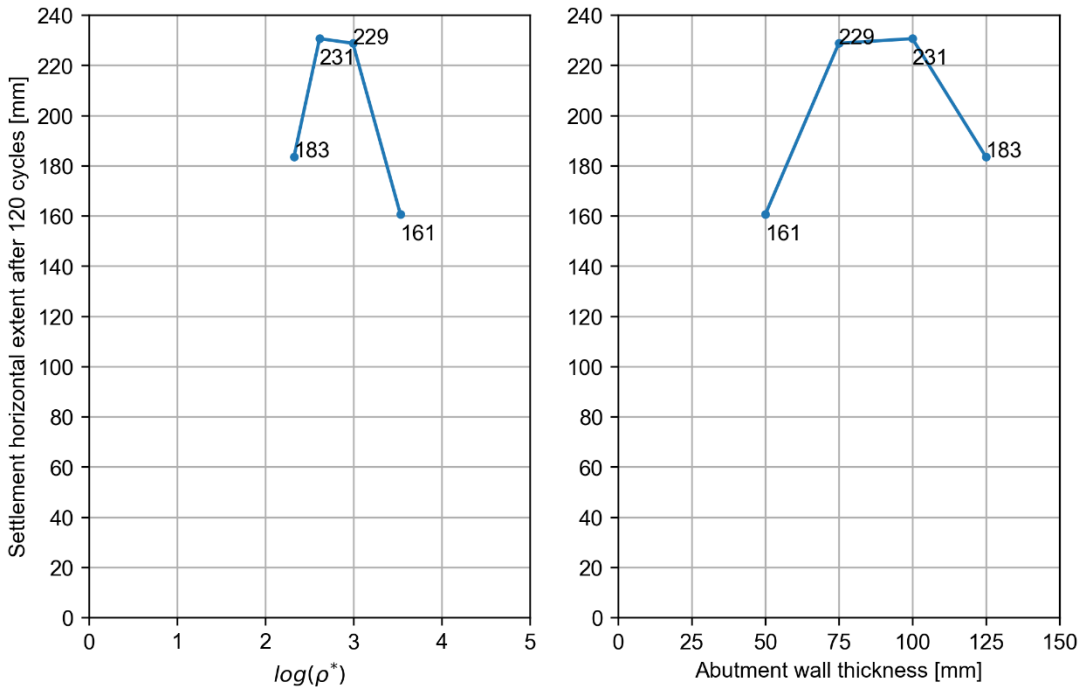

Figure 5-32: Settlement horizontal extent after 120 cycles.

The vertical settlement shown in Figure 5-33 is the vertical displacement of the sand that occurred directly adjacent to the face of the abutment wall. Generally, for increasing abutment

stiffness/thickness, it appears that the vertical settlement can be expected to decrease. However, the 125 mm abutment is an exception to this observed trend. The vertical settlement caused by a 2 mm amplitude for 120 cycles can be expected to be in the range of 65 mm to 90 mm on average for an abutment wall that is 1.5 m tall. The vertical settlement can probably be reduced by increasing the placing density of the material placed in the steel frame strong box.

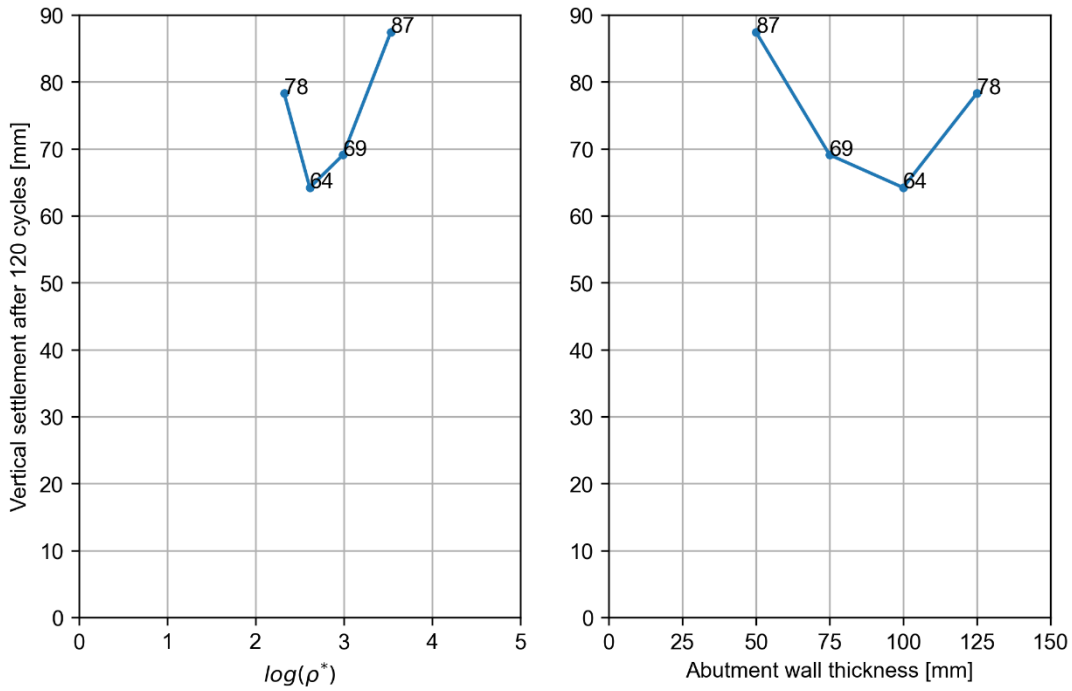

Figure 5-33: Vertical settlement at the abutment interface after 120 cycles.

5.8 Choice of abutment stiffness for integral bridges

Based on the experimental findings for the sand- and structural behaviour of the specimens, for increasing abutment stiffness it can be expected that the amount of displacement that is restricted by the retained sand also increases per cycle and this increase in restraint will take place for any given stiffness due to the ratcheting effect. Prior analysis of the 50 mm specimen (most flexible) reveals that the two opposite ends of the abutment stiffness spectrum (i.e., rigid and flexible) that was evaluated in this study showed similar results for the restricted displacements however it is generally more useful to utilise a more *rigid* abutment compared to using a flexible abutment since it can be expected that the more rigid abutment will result in increased resistance and earth pressure applied by the sand compared to the most flexible abutment. Dicleli (2005), Bloodworth *et al.* (2012), and Luo *et al.* (2022) have reported similar findings in terms of increased pressures for increasing abutment stiffnesses.

This is substantiated by the results shown in Figure 5-34, which depicts the required number of passive cycles that need to be applied to the retained sand to reach a specific net force measured by the force transducer as an indication of the resistance exerted by the retained sand. It can be seen from Figure 5-34 that the 125 mm specimen (most rigid) is capable of

generating the same sand resistance as the other specimens in a fewer number of applied passive/positive movements by thermal expansion of the deck.

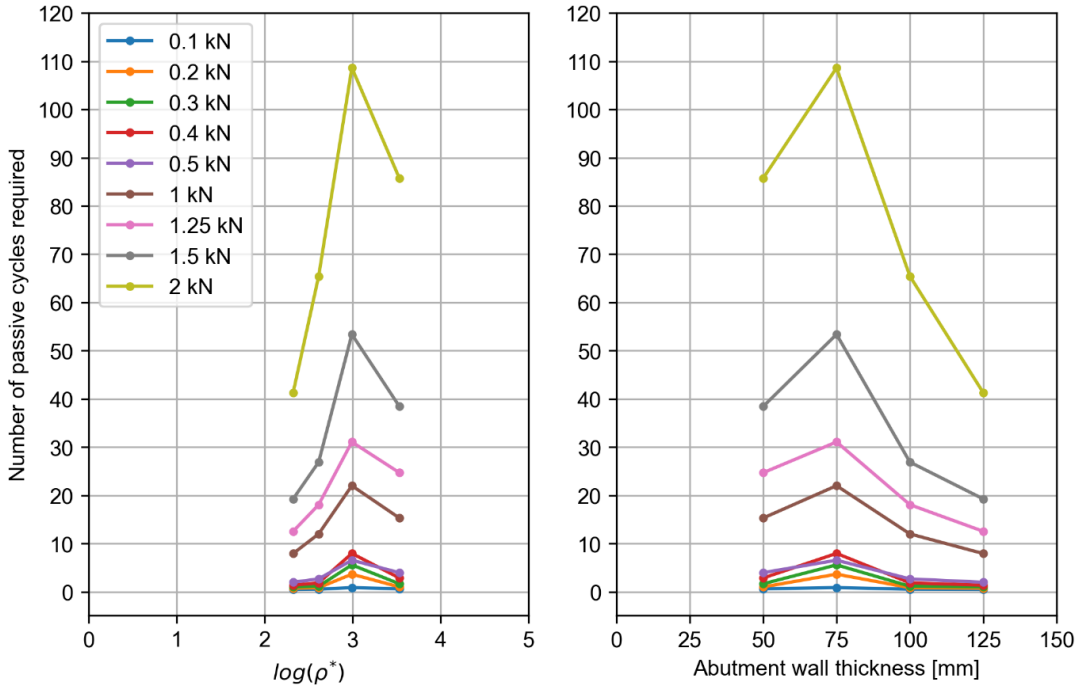

Figure 5-34: Number of passive cycles required to reach a specific measured force for different flexibility numbers/wall thicknesses.

From a serviceability limit states perspective, the findings suggest that the ideal configuration for an integral bridge required to *reduce the surface settlement of the sand at the face of the abutments* by as much as possible (within the context of this dissertation) would be to employ a significantly rigid abutment where the increase in the force exerted by the retained sand over time would be at its greatest potential. As revealed in the literature study, an initially compacted and dense retained sand fill will also lead to much greater force of restraint exerted by the sand mass during cyclic thermal expansions and contractions of the bridge.

The primary purpose of employing a rigid abutment (i.e., for serviceability limit states) is to reduce the displacement of the deck such that seasonal temperature change results in less movement of the abutments both towards the retained sand as well as away from the sand, thereby limiting the amount of settlement that can occur over time due to the ratcheting effect. The benefit of utilising a stiff/rigid abutment for the purpose of reduced surface settlement is however opposed by the expected increase in bending moment (and corresponding strains) in the abutments and any pile foundations that are present as well as increased axial force in the deck. Based on the above, a *diminishing return* effect can be expected for increasing abutment stiffness where the advantages between stiff and flexible abutments must be compared during the design of integral bridges. It should also be noted that concrete will be subject to inevitable shrinkage and creep, therefore the contribution of the movement that is restricted by the sand is further limited by time-dependent effects. Active/negative movements of the deck will therefore always take place due to these time-dependent effects and also have the potential to

initiate ratcheting of the retained sand behind integral bridge abutments as proven by the mere 1 mm amplitude in the 150 mm specimen's preliminary test.

5.9 Summary

The findings from the experimental data are summarised as follows:

- All specimens showed an increase in deflection at all LVDT positions with increasing number of cycles. For the more rigid specimens, the displacement was more pronounced at the bottom of the abutments. Analysis of the measured displacements of the top LVDT positioned onto the abutment part of the specimens against the measured displacement of the actuator demonstrated an increase in the restraint exerted by the sand over time. Even for the reduced amplitude, this was still enough to induce ratcheting in the retained sand.
- For increasing stiffness of abutments, a decrease in the magnitude of the curvature occurred.
- Bending moments were higher for increasing abutment stiffness and also increased after 120 cycles due to higher restraint being exerted by the sand due to ratcheting.
- The behaviour of lateral stresses due to ratcheting behind the abutment part of the specimens is highly sensitive to the depth at which the sensor was installed into the retained sand. Each sensor exhibited different behaviour in comparison to each other and all of these behaviours were consistent amongst the different specimens tested. The greatest earth pressures were recorded at EPC 2 (second highest sensor) at a normalised depth of $\eta \approx 0.25$. For the cells positioned above the midpoint of the abutment, pressures would increase indefinitely over time with no apparent plateau and would only reduce as a result of surface settlement occurring due to densification of the retained sand (as seen for EPC 1). Cells below the midpoint would display a rapid initial increase followed by a small decrease over the course of the applied 120 cycles. The bottom cells more closely represented the at-rest and active pressures predicted by Jaky and Rankine's equations. The upper cells all yielded pressures larger than the theoretical passive pressures according to Rankine's theory.
- The active and passive pressures measured at the cell at the back of the steel frame strong box displayed virtually identical behaviour for all specimens tested. These findings also verified that there were no boundary effects present for the test setup.
- It was found that a distinct zone develops at the upper third/quarter of the abutments where the sand particles interlock due to ratcheting and hence develop high passive pressures. The lower region of the abutment retains particles that are more often in a stationary state (much less movement in comparison) or can only develop active pressures due to sand grains above being shifted downward for each rotation of the abutment. The overall densification effect only takes place for each passive displacement applied to the specimens.
- All specimens showed an increase in the net force for every successive cycle with no apparent plateau evident after 120 cycles (i.e., no resilient behaviour was present). The greatest overall increase in force exerted by the sand occurred for the 125 mm specimen (most rigid) after 120 cycles. The smallest maximum earth pressure reached occurred for

the 75 mm wall and marked the turning point where the 50 mm specimen reached a maximum earth pressure similar to the 100 mm wall. This suggests that there is a behavioural change between flexible and rigid abutments when ratcheting is taking place in retained sand. All specimens reach the same ratio of earth pressure relative to the pressure measured at cycle 120 for any given cycle throughout the test where the 100 mm specimen's measured forces only deviated slightly beyond cycle 15. It can be expected that approximately 40% of the measured sand pressure magnitude at cycle 120 will be reached after only 10 cycles.

- Horizontal displacement contours obtained from the PIV analyses showed that most of the positive displacement occurs roughly between the quarter ($\eta = 0.25$) and the third ($\eta = 0.33$) of the depth as measured from the surface of the sand. The surface of the retained sand exhibited horizontal displacement towards the wall which is in good agreement with the observed surface settlement after each test. For specimens thicker than 50 mm, the bulb of positive displacement (located at quarter to third depth range) increases for increasing stiffness/thickness. The 50 mm specimen (most flexible) showed the greatest amount of positive horizontal displacement whereas the 75 mm specimen showed the greatest amount of negative horizontal displacement.
- Vertical displacement contours showed that for increasing stiffness, the deeper the extent of negative (downward) vertical displacement occurred. This implies that the more flexible abutments can deflect more and hence the rotations did not affect the full height of the sand mass as opposed to the more rigid specimens. The 50 mm specimen (most flexible) showed the least amount of negative vertical displacement whereas the 75 mm specimen showed the greatest amount of negative vertical displacement.
- Based on the resultant displacement contours, the 50 mm specimen showed the least sand displacement in general and the 75 mm the most. Resultant displacements for the 100 mm and 125 mm specimens were in good agreement with each other.
- The displacement vectors obtained from the PIV analyses revealed a clear triangular wedge where most sand particle flow would occur which was located at the upper third portion of the sand mass. The streamlines for the sand particles (derived from the flow vectors) indicated that all specimens had an identical particle flow pattern within the retained sand after 120 cycles. Particles at the surface level first tend to flow toward the face where a change in the horizontal direction occurs to the right and eventually creates an S-shape.
- The horizontal settlement extent was in the range of 160 mm to 230 mm for the 1.5 m tall abutments. Vertical settlement extent was in the range of 65 mm to 90 mm on average. Vertical settlement appeared to decrease for increasing abutment stiffness/thickness.
- For increasing stiffness, the amount of displacement restricted by the retained sand also increased per cycle. The restraint provided by the sand is therefore proportional to the stiffness of the abutments.
- Within the context of the current study, a more rigid abutment is the most effective due to the fact that higher forces of restraint are exerted after a given number of applied cycles compared to more flexible abutment. From a serviceability limit state perspective, a stiff/rigid abutment would reduce the surface settlement of the sand at the face of the abutments due to the greater rate of increase in force compared to a much more flexible

abutment. However, for increasing stiffness of the abutment, higher axial forces in the deck can be expected as well as increased bending moments (and corresponding strains) in the abutment and any piles and the benefits of reduced settlement must therefore be weighed against the advantage of lower forces generated in the structure when utilising a more flexible structure.

6 Conclusions and recommendations

6.1 Introduction

The following chapter is dedicated to the summary of the findings detailed in the dissertation. A section has also been devoted to recommendations regarding the test setup as well as suggestions for future research of integral bridge abutment stiffness effects.

6.2 Conclusions

6.2.1 Earth pressure related to abutment stiffness

The net force measured by the force transducer would increase for increasing number of seasonal cycles and, in general, increasing abutment stiffness would result in greater overall increase in the force of restraint exerted by the silica sand mass however the lowest increase in comparison was measured for the 75 mm specimen possibly as a consequence of an imperfect hinge at the base of the abutment wall. The maximum force reached for the 50 mm specimen (most flexible) resembled that of the 100 mm specimen, suggesting that a turning point exists which possibly indicates the presence of a behavioural change between flexible and rigid abutments for cyclic loading conditions due to temperature change.

The earth pressure behaviour of each EPC over time was dependent on the position along the height of the abutment wall but the experimental trends for each earth pressure sensor were comparable for varying abutment wall stiffnesses. Pressures measured above the midpoint of the abutment were the largest along the height of the abutment (maximum occurring at approximately $\eta = 0.25$) and increased indefinitely over time and reached Rankine passive pressures. These pressures only decreased due to surface settlement at the interface due to the densification of the retained fill.

Pressures measured below the midpoint more closely resembled the Jaky at-rest and Rankine active earth pressures and displayed an initial rapid increase in pressure for the first couple of cycles and would then slowly decrease over the course of testing each sample. The pressures did not reach a well-defined plateau after the applied 120 seasonal cycles and an asymptote was evident but would most likely only be reached for a much larger number of cycles.

The ratio of earth pressure relative to the pressure recorded at cycle 120 for any given cycle is independent of the stiffness of the abutment. The 100 mm specimen's measured net force deviated slightly from the 15-cycle mark but was considered negligible in comparison to the results from the other specimens. Roughly 40% of the magnitude of the pressure measured at cycle 120 (i.e., the end of the test) was reached after only 10 seasonal cycles regardless of the stiffness of the abutment.

6.2.2 Settlement and ratcheting related to abutment stiffness

From the PIV analyses conducted, it was observed that most of the horizontal displacement of the sand particles occurred between the third and the quarter of the depth of the silica sand (i.e., $\eta = 0.25$ and $\eta = 0.33$ respectively) towards the back of the steel frame strong box. In general, this bulb of positive displacement towards the back of the steel frame strong box increased for increasing stiffness of the abutment with the exception of the 50 mm specimen which showed the greatest amount of horizontal displacement of the sand particles, again suggesting that there is a behavioural change for rigid and flexible abutments. The surface of the retained sand showed horizontal movement towards the face of the abutment which was in agreement with the observed surface settlement at the abutment-sand interface after each test.

A distinct zone developed at the upper third/upper quarter of the abutments where the sand particles were subject to interlocking due to the ratcheting action which allowed for higher pressures whereas the lower region generally remained in a more stationary state where less movement was involved in comparison and active pressures were more common due to sand grains above being shifted downward for each rotation of the abutment.

The vertical displacement contours indicated that for increasing abutment stiffness, the deeper the extent of particle movement towards the bottom of the steel frame strong box would occur. The most flexible abutment was able to generate greater deflections compared to the more rigid specimens such that rotation of the abutment was not able to affect as much of the sand mass as opposed to the more rigid specimens.

In general, the horizontal settlement extent appeared to decrease for increasing abutment stiffness whereas the measured vertical settlement at the abutment-sand interface generally increased for increasing abutment stiffness and showed good agreement with the displacement vectors calculated for the retained sand mass from the PIV analyses.

6.2.3 Wall deflection and bending moments related to abutment stiffness

All specimens showed increased deflections for increased number of cycles at all LVDT points along the height of the abutment wall where more pronounced displacement occurred at the bottom of the rigid specimens (i.e., thickness > 50 mm). Comparison between the measured displacements at LVDT 1 that was positioned close to the top of the abutment wall and the actuator's LVDT demonstrated an increase in the restraint exerted by the sand for increasing number of cycles and was able to induce ratcheting despite having a 20% smaller displacement amplitude than originally intended. The displacements were accompanied by a decrease in the curvature that occurred for increasing abutment stiffness.

All specimens were subject to a net upward movement over time where the rigid samples displayed more uniform uplift. The increased restraint of the retained sand was sufficient to exceed the forces of self-weight, frictional forces from the sides and hinge of the steel frame strong box, as well as the resistance provided by the deck portion of the structural frame of the specimens. This net upward movement was accompanied by a net horizontal movement away from the retained sand and was evident from both the PIV analyses as well as the measurements from LVDT 1 at the top of the abutment wall.

Based on the strain gauge readings for the abutment walls, both the external and internal surfaces of the abutment wall displayed a net compressive force over time from ratcheting due to the upward shift caused by the increased restraint and lack-of-fit effects caused by the steel frame strong box. The strains reduced for increasing abutment stiffness. Curvature of the abutments decreased for increasing abutment stiffness/thickness.

6.2.4 Concluding notes on the study

It was observed that the amount of displacement restricted by the retained sand increased for increasing abutment stiffness which also increased over time. For the case of slender abutments, the point of rotation occurred at a higher point above the pinned support of the test setup where the flow/movement of the sand particles downwards was the least but exhibited the most local displacement at the top of the abutment wall compared to the more rigid abutments. The slender abutment also displayed the greatest amount of settlement at the sand surface. For the more rigid abutments, the point of rotation occurred nearer to the pinned support of the test setup where the sand particles displayed more flow/movement downwards which resulted in greater earth pressures due to the greater corresponding ratcheting action of the sand.

Within the context of the study, a more rigid abutment is the most effective choice for an integral bridge abutment due to the higher forces of restraint generated in the retained sand mass for the same number of applied seasonal cycles in comparison to more flexible abutments. The increased amount of restraint results in reduced movement of the deck of the specimens which would theoretically reduce the amount of settlement that occurs at the interface between the abutment and the retained sand as a result of the ratcheting effect. It is therefore beneficial to utilise an initially dense retained fill due to the increased initial pressures as defined in existing literature. This is necessary for the purpose of accelerating the increase in the contribution of the restricted displacement caused by the retained sand from a serviceability limit states perspective.

The benefits of reduced settlements and decreased abutment curvature as a result of utilising a much stiffer abutment can however be offset by the increase in axial forces in the deck and greater bending moments (and corresponding strain) in the abutments and accompanying pile foundations. The use of slender or rigid abutments therefore both have their own advantages and disadvantages. The concrete is also susceptible to time-dependent effects (shrinkage and creep) which can limit the contribution of the restricted movement of the retained sand and can therefore reduce the benefits of using a rigid abutment. The advantages between rigid and flexible abutments must therefore be compared during the design of integral bridges.

6.3 Recommendations

6.3.1 Test setup

The main recommendations for the test setup are as follows:

- Due to the limited number of earth pressure transducers used during testing, equilibrium could unfortunately not be determined to an acceptable degree of accuracy by use of curve fitting and numerical integration. The use of more earth pressure cells could prove advantageous for validation of the force transducer measurements.
- A net upward and outward shift occurred due to increase in restraint exerted by the retained sand and resulted in the connection at the base of the abutment no longer functioning as a perfect hinged/pinned connection (see Appendix A). A possible solution to this problem could be to rather use a fixed connection thereby eliminating any movement of the support. If a hinged support is preferred, the base of the abutment could possibly be connected to the steel box by means of bolts that allow for rotation but simultaneously restrict any horizontal and vertical movement. However, the tolerances of the holes that the bolts will slot into must then be considered during the data analysis phase.
- The effects of the stiffness of the total stress cells were not evaluated and as such were assumed to be sufficient for the scope of the study. It is acknowledged that the flexible adhesive used (i.e., the silicone gel) to attach the cells to the concrete specimens may have potentially influenced the measurements and is a potential flaw in the experiment. It is recommended that the effects of the stiffness of the stress cells and method of their attachment to the specimens be evaluated for future work.
- Based on the calibration curves for the total stress cells, it is acknowledged that the measured results may be incorrect in terms of their magnitude and is a significant shortcoming that was solved through comparing measured results relative to each other. It is recommended that the measured results from the total stress cells be verified for future testing.
- The effects of any potential inelastic strain or permanent deformation of the steel frame strong box and actuator frame were not evaluated and the test setup was assumed to be sufficiently rigid for experimental testing. It is recommended that the deformation of the steel frame strong box and actuator frame be monitored to verify the rigidity of the test setup for future testing.
- The influence of scaled deck and abutment width on backfill soil behaviour was not assessed as it was assumed that a specimen width of 300 mm was adequate for plane strain conditions to apply during experimental testing. It is recommended that the influence of the width of the specimens on the soil behaviour be evaluated for future work.

6.3.2 Future research

Suggestions for future research endeavours with respect to the effects of abutment stiffness for integral bridges are summarised as follows:

- Investigating the effects of abutment stiffness where compressible inclusions are used to reduce the earth pressure increase over time and comparing the amount of surface settlement that occurs after 120 cycles.
- Investigation the effects of abutment stiffness using *saturated* sands (i.e., including the presence of a water table).
- Comparing the behaviour of translational and rotational behaviour and possibly also the combination of the two modes of movement for varying abutment stiffness.
- Testing a greater range of abutment stiffnesses where the behaviour of significantly flexible abutments can be isolated and compared to rigid abutment behaviour.
- Specimens could be exposed to more cycles to verify the presence of a plateau in lateral stress build-up.
- Comparing the results to different types of sand and possibly also investigating behaviour of in-situ gravel.
- The presence of surcharge pressures from vehicle loading and its effects on the lateral stresses that develop over time.
- Geotechnical centrifuge experiments utilising scaled models made from steel or aluminium should also be compared to scaled abutments/retaining walls that are constructed from reinforced concrete.
- The implications of uplift on piled or framed abutments.

7 References

Abdel-Fattah, M.T., Abdel-Fattah, T.T. and Hemada, A.A. (2018). Nonlinear finite-element analysis of integral abutment bridges due to cyclic thermal changes. *Journal of Bridge Engineering*, Volume 23 (2), p.04017134.

Addenbrooke, T.I., Potts, D.M. and Dabee, B. (2000). Displacement flexibility number for multipropped retaining wall design. *Journal of geotechnical and geoenvironmental engineering*, Volume 126 (8), pp.718-726.

Alonso-Marroquin, F. and Herrmann, H.J. (2004). Ratcheting of granular materials. *Physical Review Letters*, Volume 92 (5), p.054301.

Al-Qarawi, A., Leo, C. and Liyanapathirana, D.S. (2020). Effects of wall movements on performance of integral abutment bridges. *International Journal of Geomechanics*, Volume 20 (2), p.04019157.

Archer, A. (2014). *Using small-strain stiffness to predict the settlement of shallow foundations*. MEng dissertation, Pretoria: University of Pretoria.

Arockiasamy, M. and Sivakumar, M. (2005). Time-dependent behavior of continuous composite integral abutment bridges. *Practice Periodical on Structural Design and Construction*, Volume 10 (3), pp.161-170.

Arsoy, S., Barker, R.M. and Duncan, J.M. (1999). The behavior of integral abutment bridges.

Banks, J.R. (2009). Numerical modelling of lateral stress on integral abutments due to cyclic loading (Doctoral dissertation, University of Southampton).

Banks, J.R. and Bloodworth, A.G. (2018). Lateral stress profiles on integral bridge abutments. In *Proceedings of the Institution of Civil Engineers-Bridge Engineering* (Vol. 171, No. 3, pp. 155-168). Thomas Telford Ltd.

Barker, R.M., Duncan, J.M., Rojiani, K.B., Ooi, P.S., Tan, C.K. and Kim, S.G. (1991). Manuals for the design of bridge foundations: shallow foundations; driven piles; retaining walls and abutments; drilled shafts; estimating tolerable movements; load factor design specifications; and commentary.

Bloodworth, A.G., Xu, M., Banks, J.R. and Clayton, C.R. (2012). Predicting the earth pressure on integral bridge abutments. *Journal of Bridge Engineering*, Volume 17 (2), pp.371-381.

Breña, S.F., Bonczar, C.H., Civjan, S.A., DeJong, J.T. and Crovo, D.S. (2007). Evaluation of seasonal and yearly behavior of an integral abutment bridge. *Journal of Bridge Engineering*, Volume 12 (3), pp.296-305.

Broms, B.B. and Ingelson, I. (1971). Earth pressure against the abutments of a rigid frame bridge. *Geotechnique*, Volume 21 (1), pp.15-28.

Caristo, A., Barnes, J. and Mitoulis, S.A. (2018), September. Numerical modelling of integral abutment bridges under seasonal thermal cycles. In *Proceedings of the Institution of Civil Engineers-Bridge Engineering* (Vol. 171, No. 3, pp. 179-190). Thomas Telford Ltd.

Civjan, S.A., Breña, S.F., Butler, D.A. and Crovo, D.S. (2004). Field monitoring of integral abutment bridge in Massachusetts. *Transportation research record*, Volume 1892 (1), pp.160-169.

Clayton, C.R.I. and Symons, I.F. (1992). The pressure of compacted fill on retaining walls. *Géotechnique*, Volume 42 (1), pp.127-130.

Clayton, C.R.I., Xu, M. and Bloodworth, A. (2006). A laboratory study of the development of earth pressure behind integral bridge abutments. *Géotechnique*, Volume 56 (8), pp.561-571.

Cosgrove, E.F. and Lehane, B.M. (2003). Cyclic loading of loose backfill placed adjacent to integral bridge abutments. *International Journal of Physical Modelling in Geotechnics*, Volume 3 (3), pp.09-16.

Darley, P., Carder, D.R. and Barker, K.J. (1998). Seasonal thermal effects over three years on the shallow abutment of an integral bridge in Glasgow.

Day, R.A. and Potts, D.M. (1993). Modelling sheet pile retaining walls. *Computers and Geotechnics*, Volume 15 (3), pp.125-143.

DeJong, J.T., Howey, D.S., Civjan, S.A., Brena, S.F., Butler, D.S., Crovo, D.S., Hourani, N. and Connors, P. (2004). Influence of daily and annual thermal variations on integral abutment bridge performance. In *Geotechnical Engineering for Transportation Projects* (pp. 496-505).

Dicleli, M. (2000). Simplified model for computer-aided analysis of integral bridges. *Journal of Bridge engineering*, Volume 5 (3), pp.240-248.

Dicleli, M. (2005). Integral abutment-backfill behavior on sand soil—Pushover analysis approach. *Journal of Bridge Engineering*, Volume 10 (3), pp.354-364.

Dicleli, M. and Albhaisi, S.M. (2004). Estimation of length limits for integral bridges built on clay. *Journal of Bridge Engineering*, Volume 9 (6), pp.572-581.

England, G.L. and Tsang, N.C.M. (2001). Towards the design of soil loading for integral bridges-experimental evaluation. *Department of Civil and Environmental Engineering*, Imperial College, London.

England, G.L., Tsang, C.M., Dunstan, T. and Wan, R.G. (1997). Drained granular material under cyclic loading with temperature-induced soil/structure interaction.

England, G.L., Tsang, N.C. and Bush, D.I. (2000). Integral bridges: a fundamental approach to the time–temperature loading problem. Thomas Telford.

England, G.L., Tsang, N.C., Ferreira, P. and Teixeira, M.B.S. (2007). Some design improvements for integral bridges. In Bridge design, construction and maintenance: *Proceedings of the two day international conference organised by the Institution of Civil*

Engineers and held in Beijing on 17–18 September 2007 (pp. 93-103). Thomas Telford Publishing.

Faraji, S., Ting, J.M., Crovo, D.S. and Ernst, H. (2001). Nonlinear analysis of integral bridges: finite-element model. *Journal of Geotechnical and Geoenvironmental Engineering*, Volume 127 (5), pp.454-461.

Fennema, J.L., Laman, J.A. and Linzell, D.G. (2005). Predicted and measured response of an integral abutment bridge. *Journal of Bridge Engineering*, Volume 10 (6), pp.666-677.

Hadda, N. and Wan, R. (2018). Micromechanical analysis of cyclic and asymptotic behaviors of a granular backfill. *Acta Geotechnica*, Volume 15 (3), pp.715-734.

Hambly, E.C. (1997), February. INTEGRAL BRIDGES. *In Proceedings of the Institution of Civil Engineers-Transport* (Vol. 123, No. 1, pp. 30-38). Thomas Telford-ICE Virtual Library.

Hirakawa, D., Nojiri, M., Aizawa, H., Tatsuoka, F., Sumiyoshi, T. and Uchimura, T. (2007). Residual earth pressure on a retaining wall with sand backfill subjected to forced cyclic lateral displacements. *In Soil Stress-Strain Behavior: Measurement, Modeling and Analysis* (pp. 865-874). Springer, Dordrecht.

Hoppe, E.J. and Gomez, J. (1996). Field study of an integral backwall bridge (No. VTRC 97-R7). *Virginia Transportation Research Council*.

Jardine, R.J., Potts, D.M., Fourie, A.B. and Burland, J.B. (1986). Studies of the influence of non-linear stress–strain characteristics in soil–structure interaction. *Geotechnique*, Volume 36 (3), pp.377-396.

Khodair, Y. and Hassiotis, S. (2013). Numerical and experimental analyses of an integral bridge. *International Journal of Advanced Structural Engineering*, Volume 5 (14).

Kim, W. and Laman, J.A. (2010a). Integral abutment bridge response under thermal loading. *Engineering Structures*, Volume 32 (6), pp.1495-1508.

Kim, W. and Laman, J.A. (2010b). Numerical analysis method for long-term behavior of integral abutment bridges. *Engineering Structures*, 32(8), pp.2247-2257.

Kunin, J. and Alampalli, S. (2000). Integral Abutment Bridges: Current Practice in the US and Canada. *New York Department of Transportation*.

Luo, S., De Luca, F., De Risi, R., Le Pen, L., Watson, G., Milne, D., Chapman, D., Sextos, A., Cassidy, N., Jefferson, I. and Metje, N. (2022). Challenges and perspectives for integral bridges in the UK: PLEXUS small-scale experiments. *Proceedings of the Institution of Civil Engineers-Smart Infrastructure and Construction*, Volume 40, pp.1-17.

Lehane, B.M. (2011). Lateral soil stiffness adjacent to deep integral bridge abutments. *Géotechnique*, Volume 61 (7), pp.593-603.

Naji, M., Firoozi, A.A., and Firoozi, A.A. (2020). A Review: Study of Integral Abutment Bridge with Consideration of Soil-Structure Interaction. *Latin American Journal of Solids and Structures*, Volume 17 (2).

Nam, M.S. and Park, Y.H. (2015). Relationship between earth pressure and thermally induced movement of integral abutments. *Journal of Performance of Constructed Facilities*, Volume 29 (4), p.04014093.

Ng, C.W., Springman, S.M. and Norrish, A.R. (1998a). Soil-structure interaction of spread-base integral bridge abutments. *Soils and foundations*, Volume 38 (1), pp.145-162.

Ng, C.W., Springman, S.M. and Norrish, A.R. (1998b). Centrifuge modeling of spread-base integral bridge abutments. *Journal of geotechnical and geoenvironmental engineering*, Volume 124 (5), pp.376-388.

Pappin, J.W., Simpson, B., Felton, P.J. and Raison, C. (1986). Numerical analysis of flexible retaining walls. In *Symposium on Computer Applications in Geotechnical Engineering*. The Midland Geotechnical Society, UK.

Peric, D., Miletic, M., Shah, B.R., Esmaeily, A., and Wang, H. (2016). Thermally induced soil structure interaction in the existing integral bridge. *Engineering Structures*, Volume 106, pp. 484-494.

Potts, D.M. and Bond, A.J. (1994). Calculation of structural forces for propped retaining walls. In *International conference on soil mechanics and foundation engineering*, pp. 823-826.

Potts, D.M. and Fourie, A.B. (1985). The effect of wall stiffness on the behaviour of a propped retaining wall. *Geotechnique*, Volume 35 (3), pp.347-352.

Powrie, W. and Li, E.S.F. (1991). Finite element analyses of an in-situ wall propped at formation level. *Geotechnique*, Volume 41 (4), pp.499-514.

Pugasap, K., Kim, W. and Laman, J.A., 2009. Long-term response prediction of integral abutment bridges. *Journal of Bridge Engineering*, 14(2), pp.129-139.

Rhodes, S. and Moses, J. (2016). Integral Bridges and the Modelling of Soil-Structure Interaction.

Ravjee, S., Jacobsz, S.W., Wilke, D.N. and Govender, N. (2018). Discrete element model study into effects of particle shape on backfill response to cyclic loading behind an integral bridge abutment. *Granular Matter*, Volume 20 (4), pp.1-14.

Robberts, J.M. (2003). Behaviour of integral bridges subjected to nonuniform temperature creep and soil-structure interaction loading (*Doctoral dissertation, Imperial College London (University of London)*).

Rowe, P.W (1952). Anchored Sheet-Pile Walls. *Proceedings of the Institution of civil engineers*, Volume 1 (1), pp.27-70.

Salman, N.N. and Issa, M.A. (2021). Calibration and parametric investigation of integral abutment bridges. *Engineering Structures*, Volume 227, p.111381.

Sandberg, J., Magnino, L., Nowak, P., Wiechecki, M. and Thusyanthan, I. (2020), June. The integral bridge design concept for the third runway at Heathrow, UK. *In Proceedings of the*

Institution of Civil Engineers-Bridge Engineering (Vol. 173, No. 2, pp. 112-120). Thomas Telford Ltd.

Sandeep, C.S. and Senetakis, K. (2018). Effect of Young's modulus and surface roughness on the inter-particle friction of granular materials. *Materials*, Volume 11 (2), p.217.

Skinner, A.E. (1969). A note on the influence of interparticle friction on the shearing strength of a random assembly of spherical particles. *Geotechnique*, Volume 19 (1), pp.150-157.

Skorpen, S.A., Kearsley, E.P. and Kruger, E.J. (2018) September. Measured temperature and shrinkage effects on a 90 m long integral bridge in South Africa. In *Proceedings of the Institution of Civil Engineers-Bridge Engineering* (Vol. 171, No. 3, pp. 169-178). Thomas Telford Ltd.

Springman, S.M., Norrish, A.R. and Ng, C.W. (1996). Cycling loading of sand behind integral bridge abutments.

Stanier, S.A., Blaber, J., Take, W.A. and White, D.J. (2015). Improved image-based deformation measurement for geotechnical applications. *Canadian Geotechnical Journal*, Volume 53 (5), pp.727-739.

Stroyer, J.P.R.N. (1928). Earth-Pressure on Flexible Walls. *In Minutes of the Proceedings of the Institution of Civil Engineers* (Vol. 226, No. 1928, pp. 116-134). Thomas Telford-ICE Virtual Library.

Stroyer, J.P.R.N. (1935). Earth-Pressure on Flexible Walls (Includes Photographs and Appendix). *Journal of the Institution of Civil Engineers*, Volume 1 (1), pp.94-139.

Thippeswamy, H.K., GangaRao, H.V. and Franco, J.M. (2002). Performance evaluation of jointless bridges. *Journal of Bridge Engineering*, Volume 7 (5), pp.276-289.

Thippeswamy, H.K., Raju, P.R. and GangaRao, H.V. (1994). Parametric study of single-span jointless steel bridges. *Transportation research record*, 1460, p.25.

Vaziri, H.H. (1996). Numerical study of parameters influencing the response of flexible retaining walls. *Canadian geotechnical journal*, Volume 33 (2), pp.290-308.

Walter, J.R., Morsy, A.M. and Zornberg, J.G. (2018). Experimental and Numerical Investigation of Lateral Earth Pressures Generated from Repeated Loading. *In IFCEE 2018* (pp. 158-168).

Wolde-Tinsae, A.M., Klinger, J.E. and White, E.J. (1988). Performance of jointless bridges. *Journal of performance of constructed facilities*, Volume 2 (2), pp.111-125.

Xu, M. and Guo, J. (2021). DEM study on the development of the earth pressure of granular materials subjected to lateral cyclic loading. *Computers and Geotechnics*, Volume 130, p.103915.

Xu, M., Bloodworth, A.G. and Clayton, C.R. (2007a). Behavior of a stiff clay behind embedded integral abutments. *Journal of geotechnical and geoenvironmental engineering*, Volume 133 (6), pp.721-730.

Xu, M., Clayton, C.R. and Bloodworth, A.G. (2007b). The earth pressure behind full-height frame integral abutments supporting granular fill. *Canadian geotechnical journal*, Volume 44 (3), pp.284-298.

Zhang, J., Shamoto, Y. and Tokimatsu, K. (1998). Evaluation of earth pressure under any lateral deformation. *Soils and Foundations*, Volume 38 (1), pp.15-33.

A Appendix

A.1 Visible shear bands after 120 cycles

After the 120 applied cycles, inspection of the side of the sand mass revealed *shear bands/shear failure surfaces* that were visible to the naked eye. These shear bands are indicated with a red line on the final PIV images taken of each specimen after testing as shown in Figure A-1.

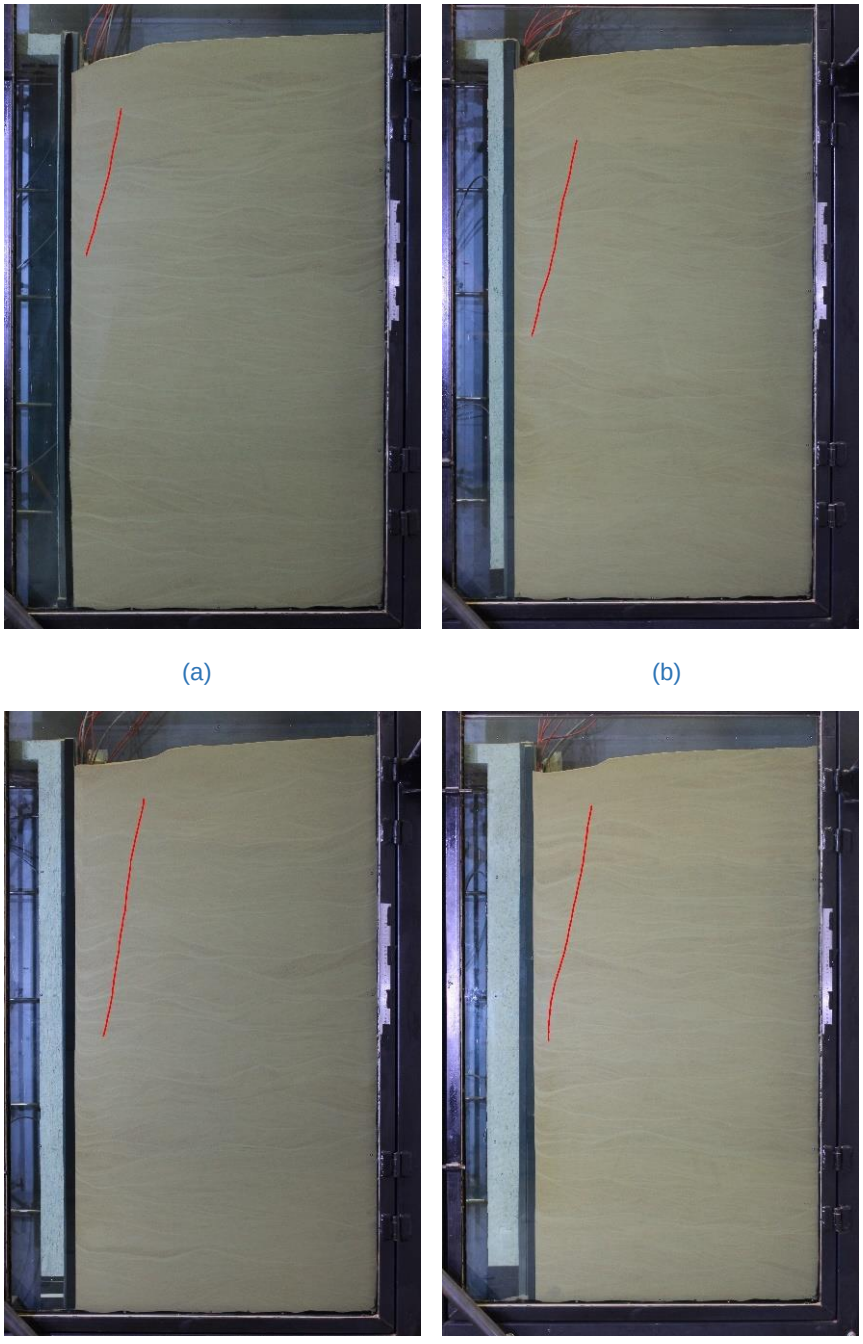

(a) (b)

(c) (d)

Figure A-1: Visible shear bands after 120 cycles for the (a) 50 mm, (b) 75 mm, (c) 100 mm, and (d) 125 mm specimens.

Analysis of the images revealed that a distinct triangular wedge formed after the 120 cycles which closely resembles the triangular region of vectors seen in the displacement vector plots shown prior (Figure 5-30). A trend is visible where, for increasing thickness of the abutment, the extent of the triangular wedge downward along the length of the abutment wall also appears to increase. The most rigid specimen has a shear band that tends to develop more vertically instead of at an angle like for the more flexible abutment which could imply that the extent of this wedge is along the entire length of the wall.

A.2 Abutment wall strains

The following section details the abutment's strain measurements on both sides of the wall.

A.2.1 Strains on the internal side

The measured strains located on the internal side of the wall (i.e., the side facing the retained sand) are shown in Figure A-2, Figure A-3, Figure A-4, and Figure A-5.

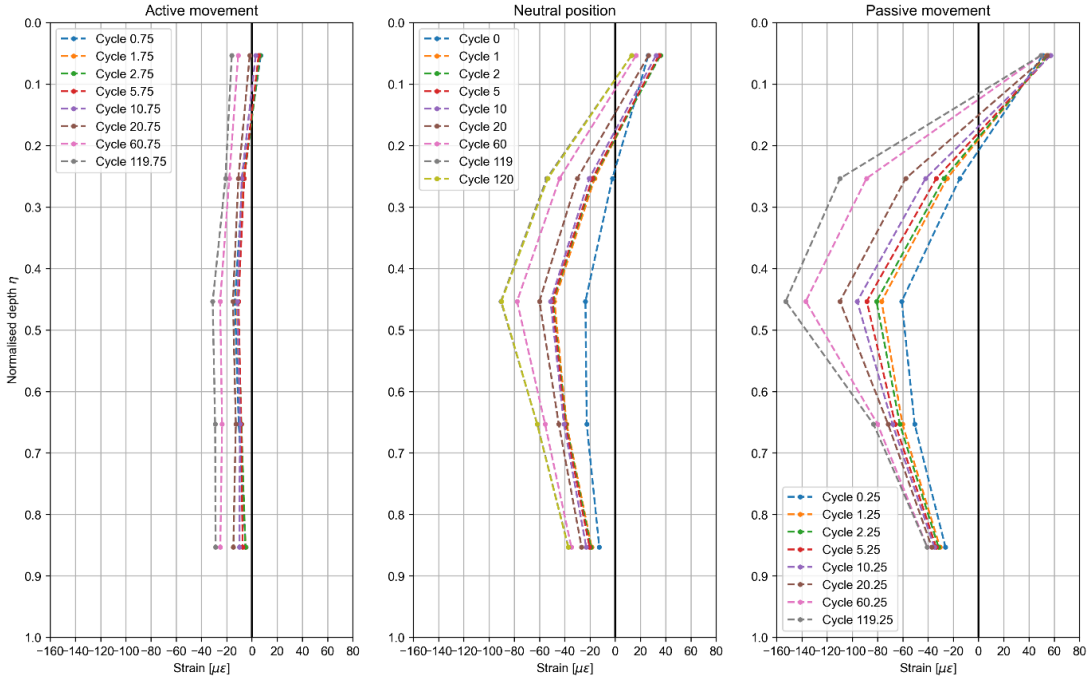

Figure A-2: Abutment internal strains for the 50 mm specimen.

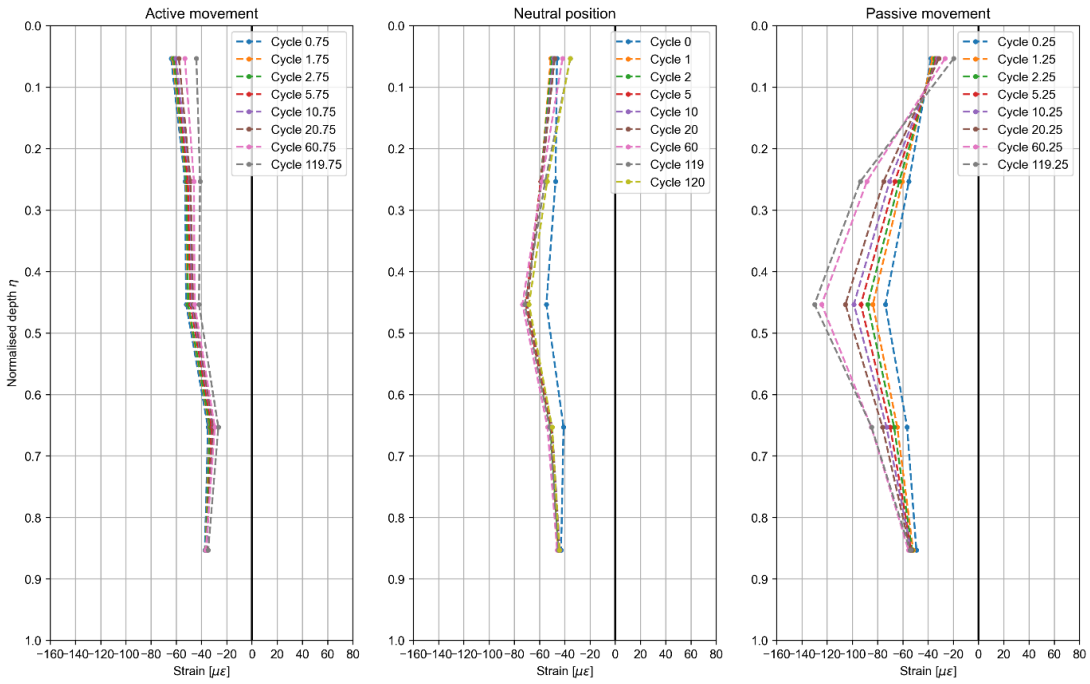

Figure A-3: Abutment internal strains for the 75 mm specimen.

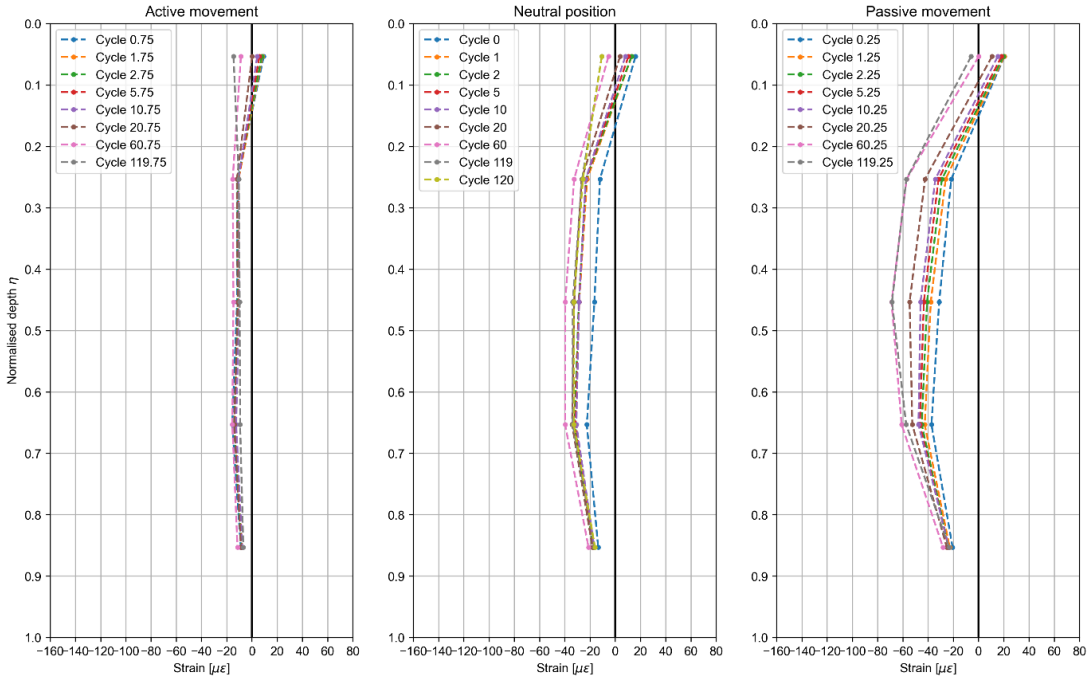

Figure A-4: Abutment internal strains for the 100 mm specimen.

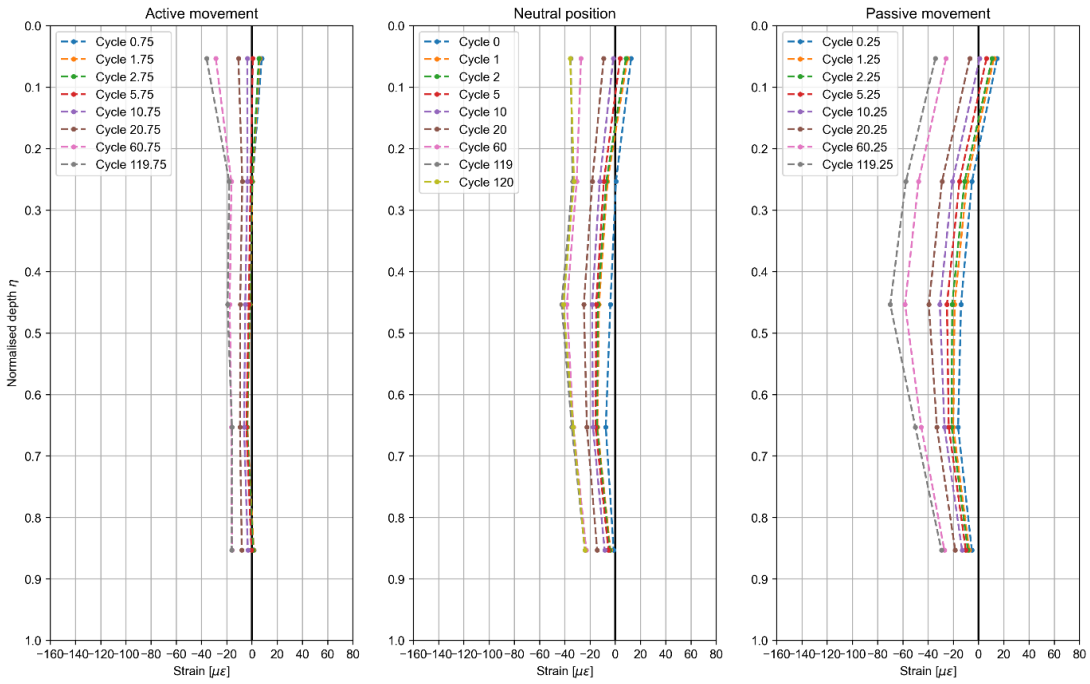

Figure A-5: Abutment internal strains for the 125 mm specimen.

A.2.2 Strains on the external side

The measured strains located on the external side of the wall (i.e., the side facing away from the retained sand) are shown in Figure A-6, Figure A-7, Figure A-8, and Figure A-9.

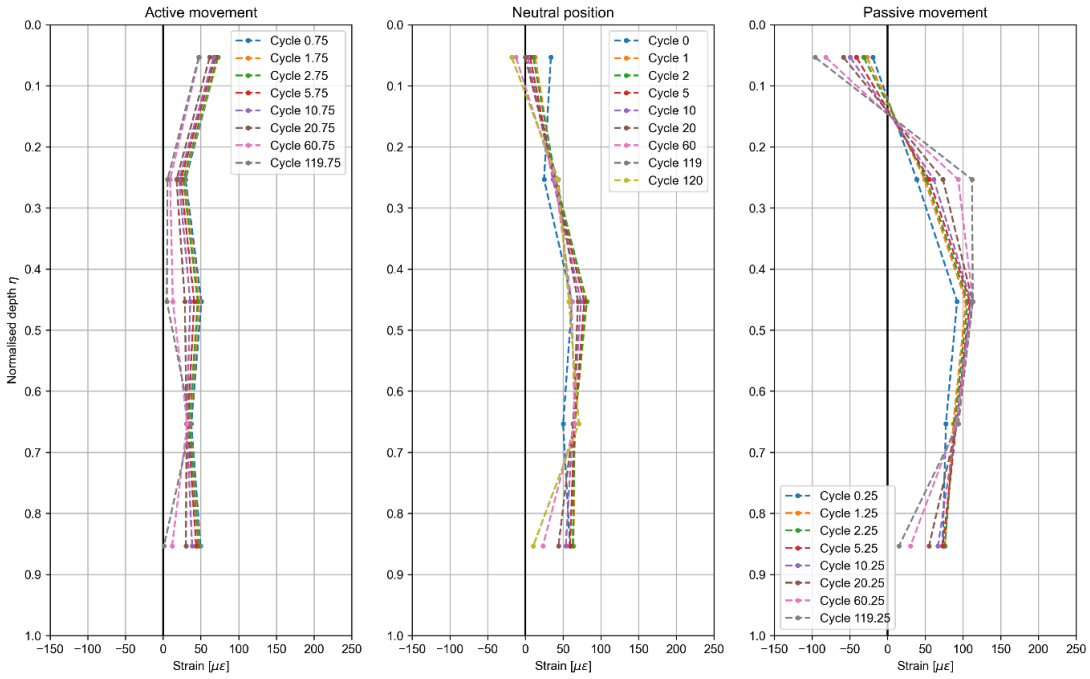

Figure A-6: Abutment external strains for the 50 mm specimen.

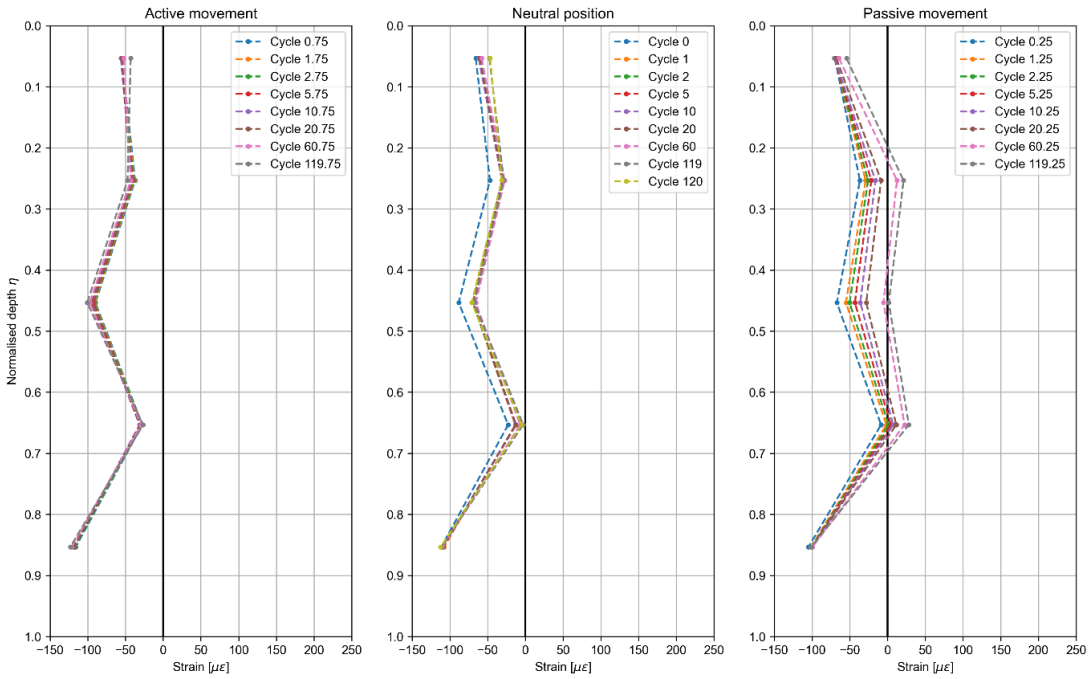

Figure A-7: Abutment external strains for the 75 mm specimen.

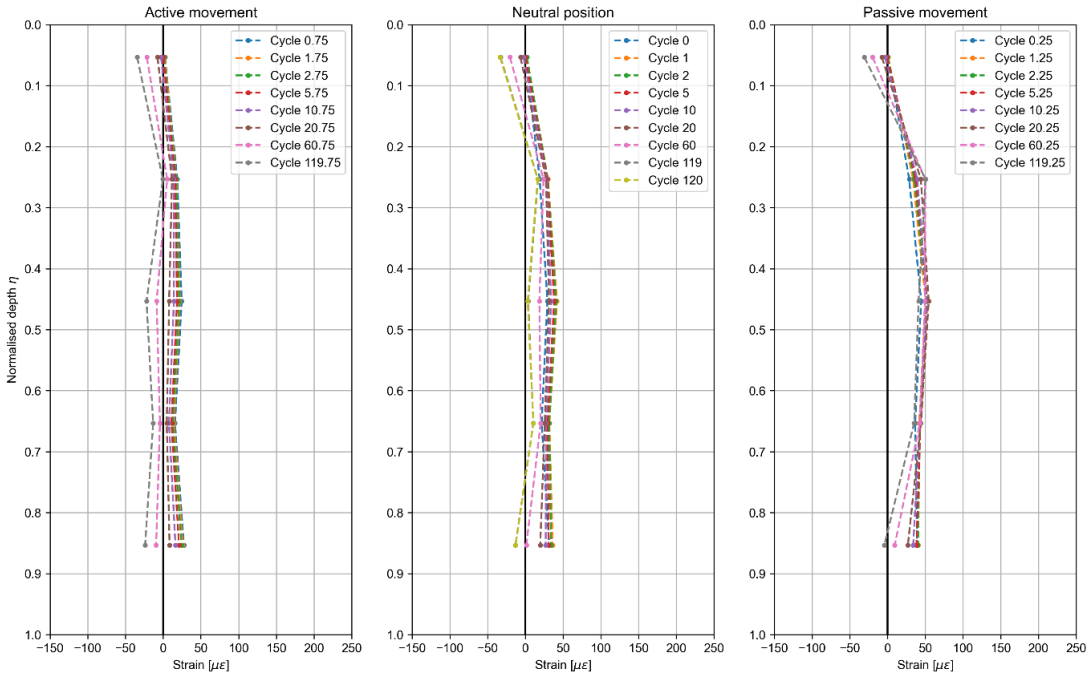

Figure A-8: Abutment external strains for the 100 mm specimen.

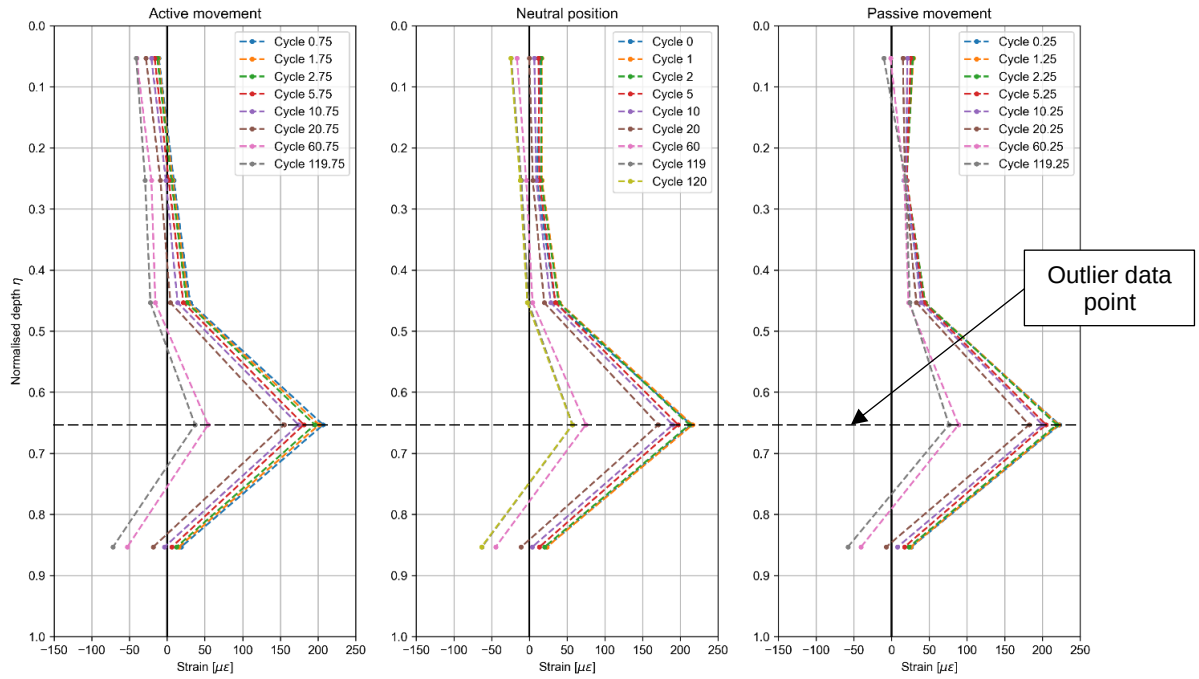

Figure A-9: Abutment external strains for the 125 mm specimen.